

https://dspace.org/

# The Paleoarchean Buffalo River komatiites Progessive melting of a single large mantle plume beneath the growing Kaapvaal craton

**T Netshidzivhe; S Tappe; Allan Wilson; A Ishikawa; F Viljoen**

ELSEVIER SCIENCE BV
https://hdl.handle.net/10539/43103
WOS

Downloaded from a DSpace repository. https://dspace.org/

Precambrian Research 393 (2023) 107071

Contents lists available at ScienceDirect

Precambrian Research

journal homepage: www.elsevier.com/locate/precamres

# The Paleoarchean Buffalo River komatiites: Progressive melting of a single large mantle plume beneath the growing Kaapvaal craton

Thendo Netshidzivhe [a,*], Sebastian Tappe [a,b,*], Allan H. Wilson [c], Akira Ishikawa [d,e], Fanus Viljoen [a]

[a] Department of Geology, University of Johannesburg, Auckland Park 2006, South Africa
[b] Department of Geosciences, UiT - The Arctic University of Norway, N-9037 Tromsø, Norway
[c] School of Geosciences, University of the Witwatersrand, Johannesburg 2050, South Africa
[d] Department of Earth and Planetary Sciences, Tokyo Institute of Technology, Tokyo 152-8551, Japan
[e] Submarine Resources Research Center, Japan Agency for Marine Earth Science and Technology (JAMSTEC), Yokosuka 237-0061, Japan

ARTICLE INFO

*Keywords:*
Early Archean
Komatiite
Kaapvaal craton
Granitoid-greenstone terrane
Highly siderophile elements
Osmium isotopes
Late accretion

ABSTRACT

Several Archean granitoid-greenstone terranes are exposed on the southeastern Kaapvaal craton in South Africa, but they received little scientific attention compared to the archetypal greenstone belt successions of the Barberton Mountain Land at the eastern craton margin. This study reports on a detailed field and geochemical survey of the Buffalo River Greenstone Belt at the southern Kaapvaal craton margin in KwaZulu-Natal, with focus on hitherto unstudied komatiites and basaltic rocks from this volcanic succession. Cross-cutting relationships and new U-Pb zircon age determinations for several granitoid units establish a minimum age of 3.26 Ga for komatiitic volcanism, possibly as old as ca. 3.5 Ga if a 3.47 Ga granodiorite sheet is interpreted as 'intrusive' into the greenstone succession.

Geochemical data reveal three types of Paleoarchean komatiites at Buffalo River. Spinifex textured lava flows represent Al-depleted komatiites, with subchondritic $Al_2O_3/TiO_2$ ratios and enrichment of LREE over HREE. The second type comprises Al-undepleted komatiites that have chondritic $Al_2O_3/TiO_2$ and flat REE patterns. The third type identified comprises Al-enriched komatiites that display suprachondritic $Al_2O_3/TiO_2$ ratios, with significant LREE depletion. The Al-depleted and Al-undepleted komatiites from Buffalo River are geochemically similar to komatiites from the 3.48 Ga Komati and 3.26 Ga Weltevreden formations of the Barberton Supergroup respectively, whereas the Al-enriched komatiites resemble the 3.33 Ga Commondale komatiites on the southeastern Kaapvaal craton.

To explain the co-occurrence of three discrete komatiite types within a single volcanic succession at Buffalo River, we suggest that each major komatiite magmatic pulse originated from the same upwelling mantle source, from which melt was extracted at different pressure but similarly hot temperature conditions. $^{187}Os/^{188}Os$ data for the Al-depleted komatiites suggest an ultimate magma origin from a primitive mantle reservoir. The contrasting $\gamma Os$ values for Kaapvaal craton komatiites (zero to positive) and peridotitic mantle xenoliths (zero to negative) support a complementary nature of these lithologies as high-degree melts and depleted residues linked by vigorous mantle plume activity at around 3.5 Ga. Such a relationship can explain the contrasting Re/Os systematics of komatiites and lithospheric mantle peridotites, which creates the contrasting $\gamma Os$ over time.

The highly siderophile element patterns of the Al-depleted komatiites from Buffalo River are similar to those of Barberton-type komatiites, for which an origin from the deepest upper mantle with high melt retention in an upwelling plume source was suggested. We confirm that this ca. 3.5 Ga mantle source had only 60–80 % of the platinum-group element budget of the modern ambient mantle, which points indirectly to a location at great depth in the aftermath of the meteoritic late accretion. Progressive melting of such an upwelling mantle source, to the point of majoritic garnet exhaustion, may explain the Al-undepleted and Al-enriched komatiites at Buffalo River. The presence of all three major komatiite types within a single volcanic succession may be linked to deep critical melting of a large mantle plume associated with growth of the Kaapvaal 'continent' at 3.5 Ga.

* Corresponding authors at: Department of Geology, University of Johannesburg, Auckland Park 2006, South Africa.
*E-mail addresses:* thendon@uj.ac.za (T. Netshidzivhe), sebastian.tappe@uit.no (S. Tappe).

https://doi.org/10.1016/j.precamres.2023.107071
Received 24 April 2022; Received in revised form 8 March 2023; Accepted 2 May 2023
0301-9268/© 2023 The Authors. Published by Elsevier B.V. This is an open access article under the CC BY license (http://creativecommons.org/licenses/by/4.0/).

## 1. Introduction

Komatiites are ultramafic volcanic to subvolcanic rocks that formed throughout Earth history, but predominantly during the Archean and Paleoproterozoic (Arndt, 2008). The youngest known komatiite occurrences are those of the Permian-Triassic Song Da zone in Vietnam (Hanski et al., 2004) and Cretaceous volcanic units on Gorgona Island off-shore Colombia and in Costa Rica forming part of the Caribbean large igneous province (Echeverria, 1980; Trela et al., 2017). The high MgO contents of komatiites (>18 wt%) imply high degrees of partial melting (>30 %) of mainly peridotitic mantle sources at > 1600 °C (i.e., ~200–300 °C above the present-day ambient mantle temperature; Sun and Nesbitt, 1978; Bickle, 1982; Herzberg, 1992; Herzberg et al., 2010; Puchtel et al., 2013) and high pressures of melt extraction at > 5 GPa (Green, 1981; Nisbet et al., 1993). Komatiitic magmas can be divided into three major types based on different geochemical compositions: (1) Al-depleted komatiites are typified by sub-chondritic $Al_2O_3/TiO_2$ ratios (5–15) with moderate incompatible trace element enrichment and heavy rare earth element (HREE) depletion with $(Gd/Yb)_N$ between 1.3 and 1.6, (2) Al-undepleted komatiites have chondritic $Al_2O_3/TiO_2$ of ~ 22 and flat HREE patterns, and (3) Al-enriched komatiites are characterised by supra-chondritic $Al_2O_3/TiO_2$ of > 30 and marked HREE enrichment (Sun & Nesbitt, 1978; Jahn et al., 1980, 1982; Nesbitt et al., 1979). These compositional variations relate to the origins of komatiitic magmas and can be explained by: (1) evolution in a mantle plume head by partial melting (30–50 %) of dry garnet peridotite at 150 to 400 km depths (Sun and Nesbitt, 1978; Nesbitt et al., 1979; Jahn et al., 1982; Campbell et al., 1989; Ohtani et al., 1989; Robin-Popieul et al., 2012; Schneider et al., 2019), (2) evolution in a subduction-related tectonic setting, where melting takes place within a hydrous mantle at shallower depths and lower temperatures (Allegre, 1982; Parman et al., 1997; Grove et al., 1997; Stone et al., 1997), and (3) evolution in dry mantle plumes that interacted with $H_2O$-bearing minerals in the mantle transition zone between 660 and 410 km depths during ascent to Earth's surface (Sobolev et al., 2016, 2019; Asafov et al., 2018).

Although the Kaapvaal craton in southern Africa is known for its diverse record of Archean komatiitic magmatism (e.g., Robin-Popieul et al., 2012; Wilson, 2019; Bolhar et al., 2021), some smaller greenstone belt remnants at the southern craton margin have received relatively little attention regarding their potential komatiite inventory (Hofmann et al., 2019). One such example, and the subject of this study, is the Buffalo River Greenstone Belt of KwaZulu-Natal in southeastern South Africa. This small greenstone belt provides a rare window into the Early Archean geology at the southernmost edge of the Kaapvaal craton that is otherwise covered by thick sediment-dominated successions of the Late Archean Pongola and Phanerozoic Karoo supergroups (Dixon, 2004).

Our study reveals the nature and origin of komatiites from previously poorly documented parts of the Kaapvaal craton, permitting a broader perspective on Archean magma genesis and tectonic processes during formation of the earliest continents. More specifically, we report on the first geochemical investigation of a wide range of ultramafic–mafic volcanic rocks (i.e., komatiite, komatiitic basalt, basalt) from the Buffalo River Greenstone Belt, including major and trace element compositions, as well as highly siderophile element (HSE) concentrations and Re-Os isotopic compositions. The results for the ultramafic–mafic volcanic rocks are complemented by $^{207}Pb/^{206}Pb$ zircon ages for cross-cutting granitoid units, which establishes a Paleoarchean age of the komatiitic volcanism at the southern margin of the Kaapvaal craton. Our data enable us to develop a model in which the rare co-occurrence of all three major komatiite types (i.e., Al-depleted, Al-undepleted, Al-enriched) in a geographically confined greenstone belt succession is linked to a single mantle plume, with melt extraction over a wide depth range concomitant with Kaapvaal craton lithosphere growth during the Paleoarchean.

## 2. Geological background

### 2.1. Archean greenstone belts of the Kaapvaal craton

The Kaapvaal craton of southern Africa exposes a large portion of the Archean continental crust and is one of the world's oldest and best-preserved granitoid-greenstone terranes (de Wit et al., 1992; Van Kranendonk, 2011; Anhaeusser, 2014). The Kaapvaal craton formed due to the amalgamation of four different lithospheric blocks, namely the Murchison, Witwatersrand, Swaziland and Kimberley blocks (Fig. 1; Eglington and Armstrong, 2004). The craton is endowed with many greenstone belts, with the classic and well-studied 3.55–3.20 Ga old Barberton Greenstone Belt located in the eastern part of the craton (Anhaeusser, 2014; Lowe and Byerly, 2007). The Barberton Greenstone Belt consists of a 15–20 km thick tightly folded volcano-sedimentary sequence (Barberton Supergroup) surrounded by felsic plutons of Paleoarchean and Mesoarchean age (Viljoen and Viljoen, 1969; Brandl et al., 2006; Lowe and Byerly, 2007). The entire eastern part of the craton was affected by a pervasive metamorphic-tectonic event at ca. 3.2 Ga (Kröner et al., 2018). Immediately south of the Barberton Greenstone Belt, the ca. 3.5 Ga Schapenburg greenstone remnant is characterized by rock successions that are similar to those of the lower portion of the Barberton Supergroup and, thus, considered as time equivalents (Anhaeusser, 2014). Several small Archean granitoid-greenstone terranes are exposed in the southernmost part of the Kaapvaal craton, where they are partly affected by the ca. 1.1 Ga Namaqua-Natal orogeny during which the Rodinia supercontinent formed. Remnants of such Paleoarchean crust include the greenstone belts at Commondale, Nondweni and Ilangwe, as well as the basement inliers at Mfule Gorge, Melmoth, Mhlatuze, Nkandla and Buffalo River (du Toit, 1931; Linström, 1987; Hofmann et al., 2019). The Nondweni Greenstone Belt is the largest greenstone remnant south of the Barberton Greenstone Belt (Fig. 1). It is dominated by mafic (basalt and komatiitic basalt) and felsic rocks (rhyolite typically deformed to quartz-feldspar-sericite schists) with subordinate pyroxene spinifex textured komatiites, plus minor sedimentary components (Wilson and Versfeld, 1994).

### 2.2. Buffalo River Greenstone Belt

The Paleoarchean greenstone assemblage consists predominantly of ultramafic and mafic lava flows, including komatiites, komatiitic basalts and basalts; the latter are commonly 'pillowed', which suggests a submarine volcanic environment. The greenstones are generally steeply dipping and strike N-S. They are intercalated with relatively thin chert and quartzite layers, as well as banded iron formations and felsic volcanic rocks. 'Younging' directions deduced from the basaltic pillow lavas of the eastern and western inliers indicate that the volcano-sedimentary succession forms a larger-scale structure, known as the Sifula synform, in which the stratigraphy is partly repeated due to minor faulting (Dixon, 2004) (Fig. 2). The unconformably overlying Karoo Supergroup obscures the fold closure, which is inferred to occur within the Mgunjane inlier of the central part of the Buffalo River Greenstone Belt. The supracrustal assemblages within the Sifula synform are separated into the Sibonvu and Mgunjane Formations (Dixon, 2004). The limbs of this synform are dominated by greenschist with subordinate chert as well as quartz sericite schist. The greenstones in the core of the Sifula synform are mostly serpentinised. The Sibonvu Formation comprises the Paleoarchean greenstones exposed within the Sifula valley and the Buffalo River Gorge, and was subjected to intensive tectonic overprinting, with up to five discrete deformation events recognised (Dixon, 2004). The Mgunjane Formation is a sub-vertically dipping, faulted and folded greenstone succession that comprises rocks within the Mgunjane valley at the inferred core of the Sifula synform. This formation hosts komatiitic lava flows with well-preserved spinifex textures, as well as subordinate cherts, BIFs and felsic volcanic rocks. On the basis of field observations, lithological variations are shown as profiles

highlighting the dominant rock types of the Sifula and Mgunjane inliers (Fig. 2c). The profiles are drawn from the outcrop transects 1 to 10 (Fig. 2a-b). The lower boundary of the Mgunjane Formation is a sheared NE-SW trending contact between the greenschists and a thick serpentinite unit on the western flank of Sibonvu Hill along with the greenschist-dominated assemblage to the east. The NE-dipping Mesoarchean Pongola Supergroup (mainly quartzites, amygdaloidal lavas and stromatolitic dolomites, plus subordinate conglomerates and volcaniclastic rocks; Wilson et al., 2013) and the flat-lying Late Paleozoic Karoo Supergroup (e.g., Dwyka diamictites) obscure the upper boundary of the Mgunjane Formation.

Four distinct intrusive Paleoarchean granitic bodies have been identified along the southeastern margin of the Kaapvaal craton (du Toit, 1931; Dixon, 2004). These pre-Pongola granitoids are exposed in several small and widely-spaced basement inliers (Fig. 2). Granitoid bodies that intruded the volcano-sedimentary assemblage of the Sifula Subgroup comprise an older tonalite-trondhjemite-granodiorite (TTG) suite associated with true granites of slightly younger age based on field relationships. An older coarse-grained melanocratic granodiorite is in contact with a younger leucocratic granodiorite, which has been correlated with the ca. 3.29 Ga Mvunyana granodiorite (Matthews et al., 1989). The Mvunyana granodiorite is an extensive granitoid body exposed mainly in the Nondweni district some 60 km to the northeast of the Buffalo River Greenstone Belt. The younger granodiorite is exposed in the central and lower reaches of the Buffalo River, as well as in several smaller valleys east of the gorge (Dixon, 2004). An intrusive contact is exposed on the west bank of the Sifula River, where granodioritic sheets are infolded with the ultramafic–mafic units of the Buffalo River Greenstone Belt (Fig. 2).

## 3. Lithologies, field relationships, and samples studied

The Buffalo River greenstone assemblage consists of sub-vertically dipping mafic to ultramafic volcanic rock units, including spinifex-textured komatiites, basalts (commonly with pillow structures), amphibolites, actinolite-tremolite chlorite schists and talc schists (preserving relict spinifex textures), associated with subordinate quartz sericite schists, cherts, and banded iron formations. The Sibonvu Formation is dominated by greenstones outcropping within the eastern and western inliers (Fig. 2). Basalt units preserving pillow structures dominate the Sifula (western) inlier, indicating a submarine environment with significant water depths, typically exceeding 1000 m (White et al., 2015).

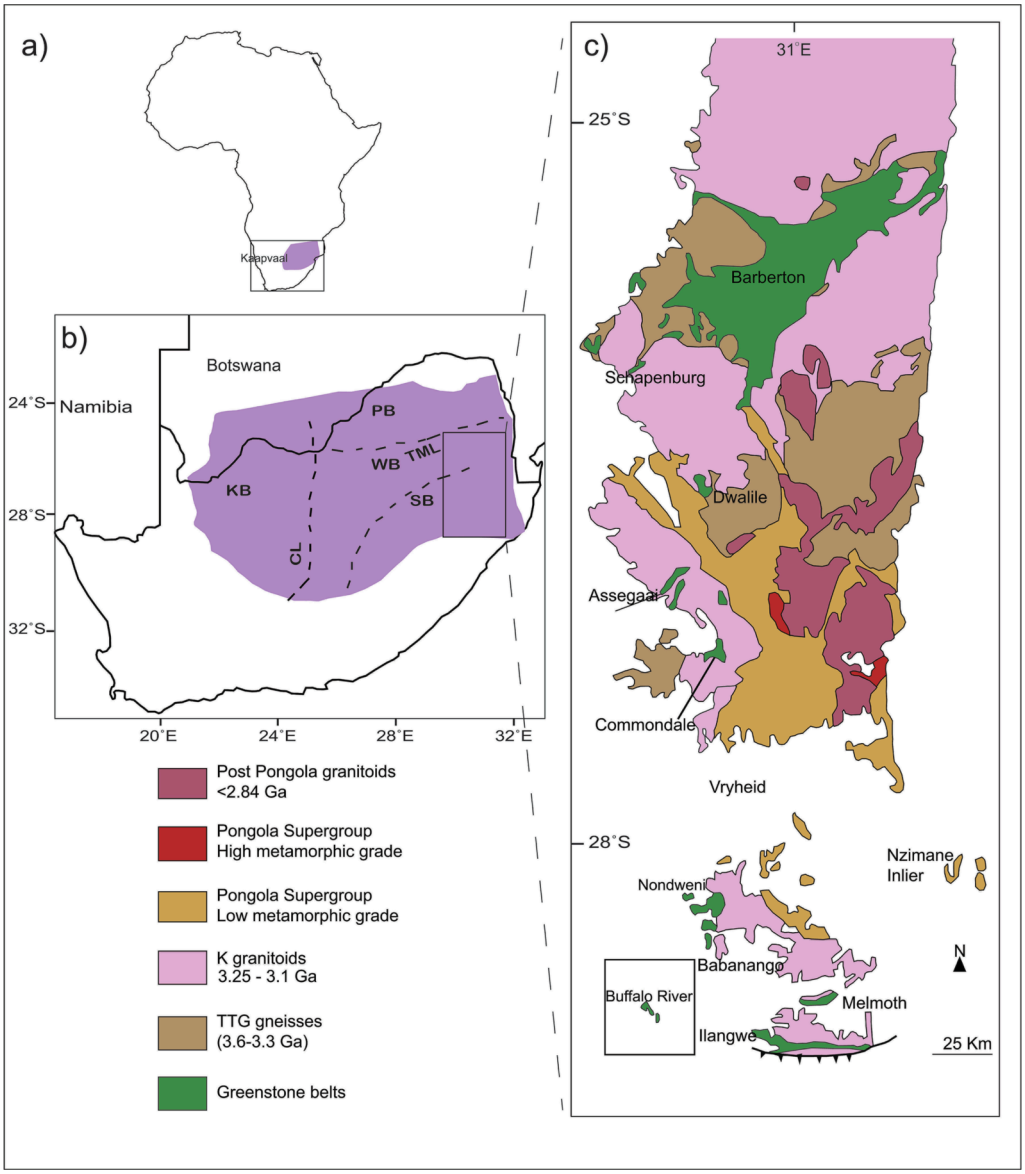



**Fig. 1.** Location of the Kaapvaal Craton (a) and (b) associated subdomains and structural features. KB Kimberley Block, SB Swaziland Block, WB Witwatersrand Block; PB Pietersburg Block, CL Colesberg lineament, TML Thabazimbi-Murchison Lineament; (c) geological map of the south-east region of the Kaapvaal craton, showing the distribution of Archean granitoid and greenstone belt remnants (after Hofmann et al., 2019). The Paleoarchean Buffalo River Greenstone Belt is located at the southern boundary of the Kaapvaal craton with the Mesoproterozoic Natal thrust belt.

Although the rocks of the Buffalo River Greenstone Belt are mainly of greenschist-facies metamorphic grades, in some areas amphibolite-facies conditions are apparent. For example, fine-grained sheared and carbonate veined amphibolite schists occur within the Sifula valley (Fig. 3a). These amphibolites are overlain by massive fine-grained black serpentinites. In places, the serpentinites are also strongly sheared and overlie felsic lava flows that are<1 m in thickness (Fig. 3b).

The Mgunjane Formation is dominated by actinolite-tremolite and talc schists. Sparse outcrops of komatiites are best exposed within this formation and display well-preserved spinifex textures of various types. Complete komatiitic flow units are present in the southern section of the Mgunjane inlier, characterized by basal cumulates grading upwards into spinifex zones of both platy and randomly oriented textural forms (Fig. 4a-d). These flow units are approximately 50 cm in thickness. Pseudomorphs of olivine spinifex have serpentine and magnetite compositions. These acicular crystals range in length from 1 to 11 cm. These komatiite flows preserve textures similar to those of the most diagnostic komatiite lava flows in the Barberton Greenstone Belt of the eastern Kaapvaal craton (e.g., Viljoen and Viljoen 1969) and the Pyke Hill outcrops in the Abitibi Greenstone Belt of the Superior craton in Canada (e.g., Pyke et al., 1973). In the northern part of the Mgunjane inlier, random spinifex textures defined by ~ 1–3 cm large serpentine pseudomorphs after olivine are preserved within weathered outcrops dominated by pale green talc schists. Unlike those from the southern part of the Mgunjane inlier, these scant outcrops do not expose complete komatiite lava flows (Fig. 4e-f). The platy ~ 10 cm long 'spinifex' crystals observed in the northern Mgunjane inlier are elongated (Fig. 4d), similar to those shown in Fig. 4e from the southern part.

Pillow basalts found within the Buffalo River Greenstone Belt show variations in shape, size, and composition. Pillows are common within the Sibonvu Formation, where their sizes range between 10 and 50 cm, with well-developed bulbous shapes (Fig. 5a). A common feature of pillow structures in greenstone belts worldwide is the presence of ocelli (varioles) within the pillow cores and rims (Fowler et al., 2002; Sandsta et al., 2011).

In the Buffalo Gorge, near the southern intrusive contact between granitoids and greenstones, a coarse-grained melanocratic granitoid unit is cross-cut by a leucocratic granitoid. Dixon (2004) correlated the younger unit with the 3.29 Ga Mvunyana granodiorite (Matthews et al., 1989), which is an extensive intrusive body exposed at surface in the Nondweni district some 60 km to the northeast of our study area (Fig. 1).

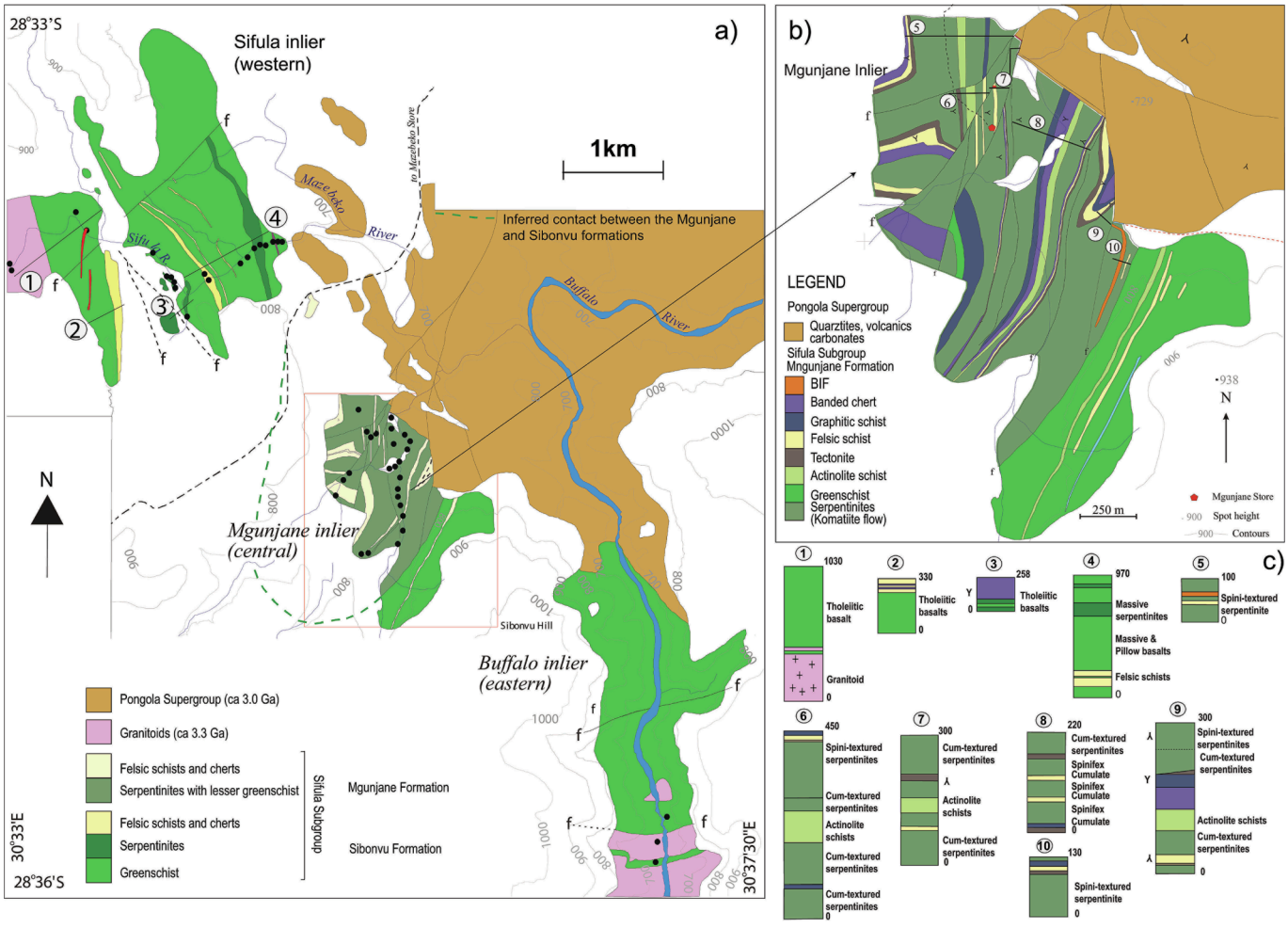



**Fig. 2.** a) A geological map of the study area showing the location of the Sifula, Mgunjane and Buffalo inliers comprising the Paleoarchean Buffalo River Greenstone Belt (modified after Dixon, 2004). These are unconformably overlain by the Mesoarchean Pongola Supergroup (in brown), while white areas on the map comprises of undeformed sediments of the Phanerozoic Karoo Supergroup. Sample localities are indicated by black dots (see Supplementary Table S1 for a detailed list of all samples collected; b) inset corresponding to the lithological sections detailing the key greenstone assemblages within the areas of sampling in the Mgunjane inliers. Ten numbered transects are shown on the outcrop maps drawn for the Sifula and Mgunjane inliers; c) lithological profiles corresponding to the transect lines drawn in (b).

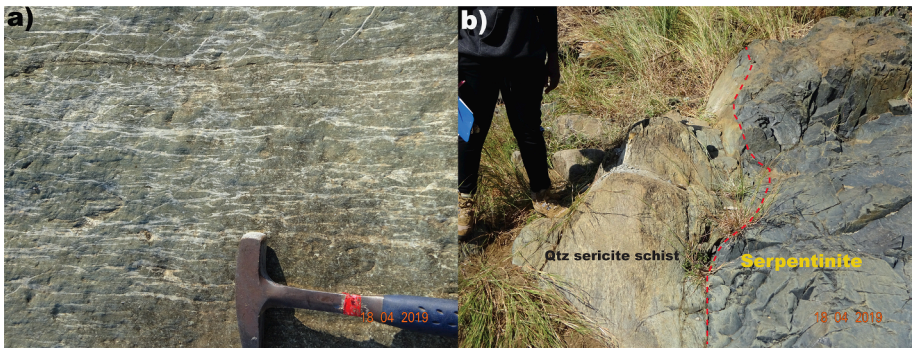



**Fig. 3.** Images of selected (typical) rock exposures encountered in the Sifula inlier: a) dark schistose amphibolite with white secondary carbonate veining; b) dark massive serpentinite in contact with paler quartz-sericite schist.

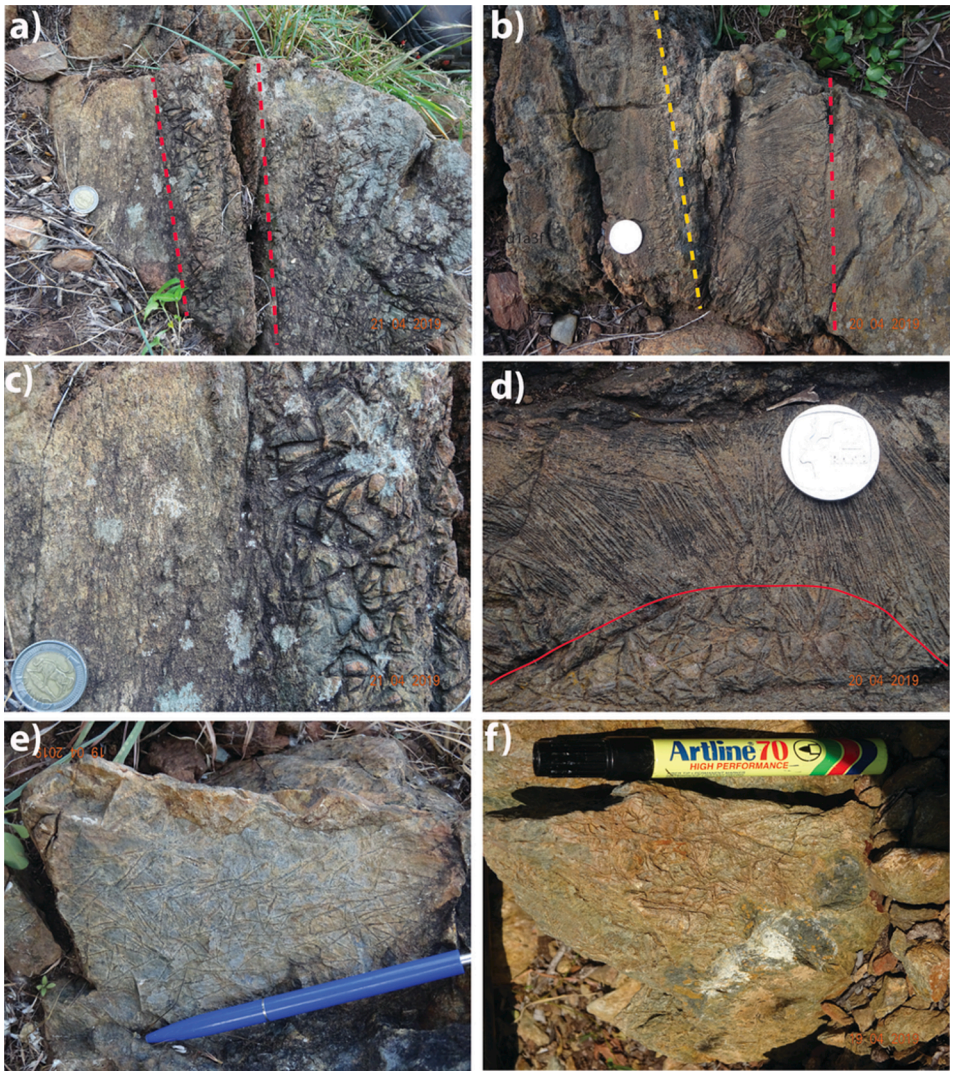



**Fig. 4.** Field photographs of spinifex-textured komatiitic lava flows encountered in the Mgunjane inlier of the Buffalo River Greenstone Belt: a) komatiite flow with basal cumulate (left of image) and top spinifex texture (between the two red lines); b) komatiite flow showing a basal cumulate-textured zone and overlying platy as well as randomly orientated spinifex texture; c) close-up view of outcrop (a) showing the contact between the cumulate and spinifex textural zones; d) close-up view of outcrop (b) showing the contact between randomly-oriented spinifex at the bottom and which grades into and is overlain by platy spinifex; e-f) random spinifex texture seen in talc schists. (For interpretation of the references to colour in this figure legend, the reader is referred to the web version of this article.)

## 4. Petrography

### 4.1. Ultramafic and mafic volcanic rocks

The ultramafic–mafic rocks of the Buffalo River Greenstone Belt comprise mainly komatiites and basalts based on their textures and mineralogy. The komatiites have characteristic spinifex textures. Both the spinifex and the basal cumulate zones of these komatiite lava flows are serpentinised. The most abundant mineral is serpentine pseudomorphic after olivine, with accessory magnetite and amphibole being disseminated throughout the komatiite flow units. In detail, the spinifex zones of the komatiite lava flows are characterised by serpentine after olivine + magnetite ± carbonate in a talc-tremolite-actinolite matrix. The former olivine blades within the spinifex zone show both random and platy orientation (Fig. 6a-b). In some samples, alternating plates of olivine (now serpentine) and pyroxenes (replaced by tremolite-

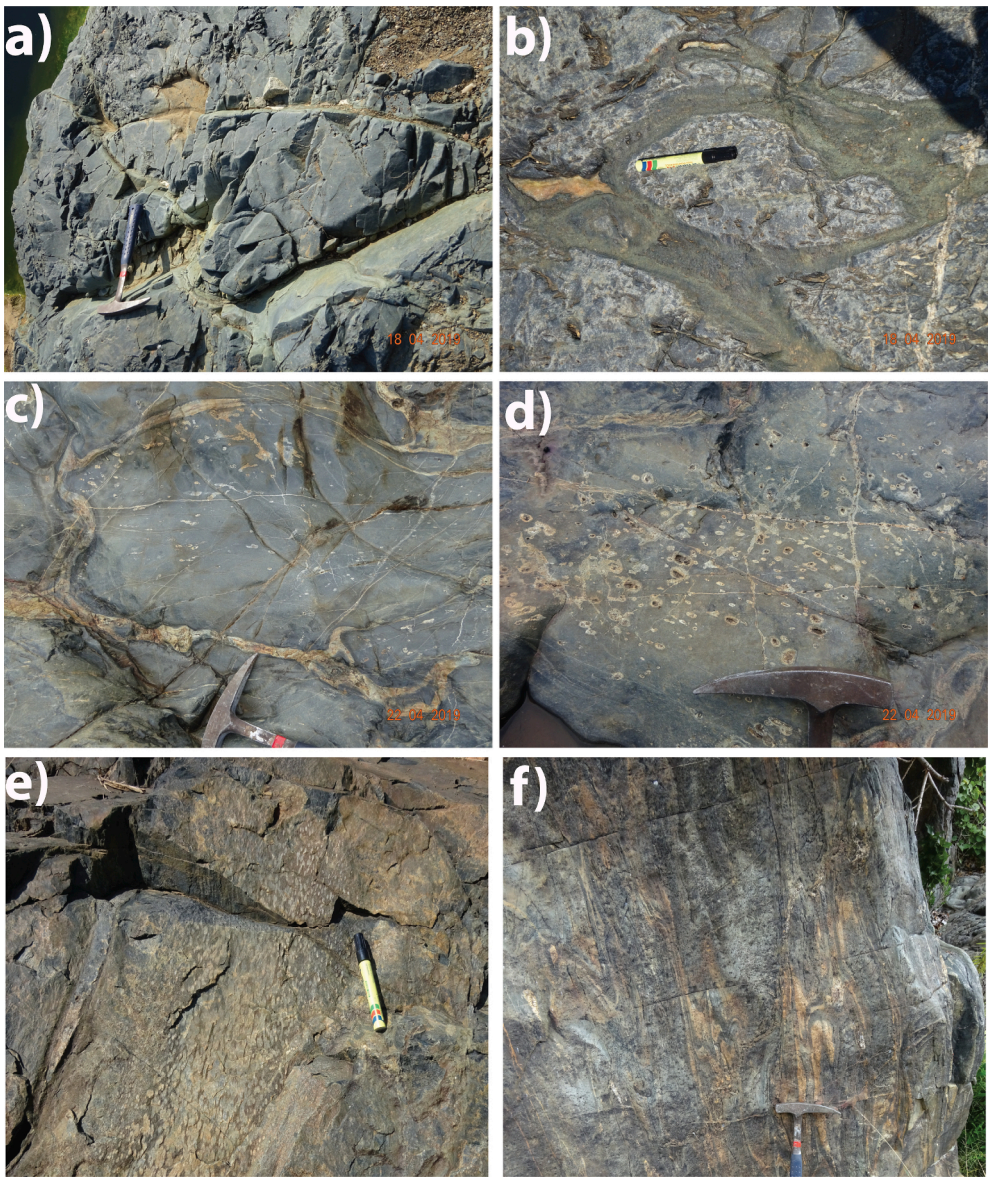



**Fig. 5.** Assorted images of pillow basalt in the Buffalo River Greenstone Belt: a) intact meter-sized pillow defined by a rim of serpentine (Sifula inlier); b) pillows with dark thick chilled margins (Sifula inlier); c) deformed pillow margin now filled with secondary quartz (Sifula inlier); d) quartz-filled vesicles in a pillow (Sifula inlier); e) the ocelli-dominated core of a pillow (Buffalo inlier); f) flattened and folded vertical pillow structures (Buffalo inlier).

actinolite) characterise the textures of the spinifex zone (Fig. 6b). Secondary magnetite, as a product of the olivine serpentinization process, is present in feather shaped textures, in particular along the 'olivine' blade margins. Platy and random spinifex textured komatiites consist of thin parallel olivine blades with a wide range of crystal sizes. The metabasalts are divided into three main groups based on their 'secondary' mineralogy. (1) A so-called serpentinite group is dominated by the presence of Mg-rich minerals such as serpentine, tremolite and talc with minor chlorite and carbonates. Interstitial plagioclase is altered to saussurite. In rare instances, the elongated outlines of former orthopyroxene crystals are completely replaced by serpentine (Fig. 6c). (2) The second 'basaltic' sub-group is represented by actinolite schists dominated by phenocrysts of actinolite set in a tremolite, chlorite, talc and feldspar matrix (Fig. 6d, f). These *meta*-basaltic rocks also contain accessory carbonate and oxide minerals. (3) The third basaltic group is characterised by rocks dominated by tremolite and referred to as tremolite schists. These are dominated by fibrous tremolite with minor plagioclase and accessory actinolite (Fig. 6e).

### 4.2. Granitoids

A medium-grained granite (BR19-57) from the eastern inlier consists of abundant quartz + plagioclase + biotite, with subordinate modal amounts of hornblende and alkali feldspar (Fig. 7a). Quartz and plagioclase occur as subhedral to anhedral crystals, with plagioclase being partly altered to sericite. Small aggregates of quartz may occur in clusters around larger plagioclase crystals. An equigranular granite sample (BR19-64) from the Buffalo River Gorge is characterised by abundant plagioclase and quartz with accessory biotite (Fig. 7b). A megacrystic granodiorite (BR19-67B) crops out in the Buffalo River Gorge and consists of subhedral plagioclase phenocrysts set in a medium- to fine-grained groundmass of quartz and biotite. Associated with BR19-67B is a leucocratic medium-grained granite (BR19-67A), which is in lithological contact with the much coarser grained granodiorite. BR19-67A consists of abundant quartz + plagioclase + biotite, with accessory alkali feldspar.

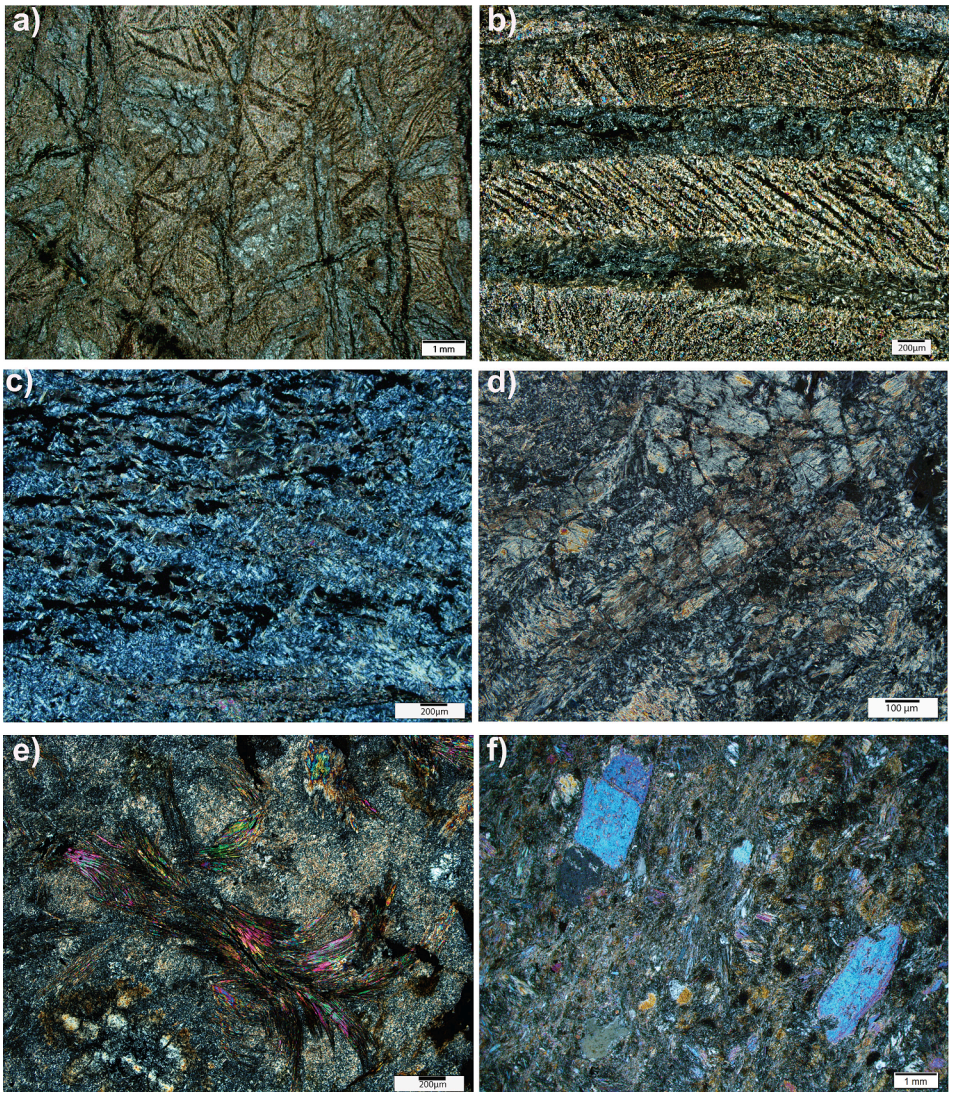



**Fig. 6.** Photomicrographs of thin sections (cross-polarized light) of mafic and ultramafic volcanics in the Buffalo River Greenstone Belt: a) random spinifex textured-komatiite sample BR19-47 (Mgunjane inlier); b) platy spinifex-textured komatiite sample BR19-62D (Mgunjane inlier), showing large blades of olivine now replaced by carbonate and serpentine, and with dark areas consisting mainly of magnetite; c) basal olivine cumulate in a komatiite flow, now altered to serpentine, magnetite and trace quantities of amphibole (probably after pyroxene) in sample BR19-47H (Mgunjane inlier); d) elongate pseudomorphs after probably orthopyroxene, now comprising of serpentine and amphibole, in sample BR19-39 (Mgunjane inlier); e) curved fibres of tremolite in a matrix of talc, chlorite, and tremolite, in sample BR19-49 (Mgunjane inlier); f) coarse crystals of actinolite set in a finer matrix of actinolite, talc, tremolite, chlorite and altered plagioclase in sample BR19-60 (Sifula inlier).

## 5. Analytical methods

### 5.1. Rock sample preparation

All samples were prepared for thin section microscopy and imaging using the transmitted and reflected light options of the Olympus BX51 petrographic microscope at the University of Johannesburg. The rock samples were also prepared for geochemical and isotopic analyses. Rock slabs were cleaned from any saw marks with corundum-based abrasive cloths and then crushed with a plastic lined hammer into mm-sized chips. The rock chips were milled in an agate pot to produce powders that are homogeneous and fine enough for whole-rock major and trace element analyses (including the highly siderophile elements), as well as for Os isotope analytical work.

### 5.2. Whole-rock major and trace element analyses

Loss on ignition (LOI) was determined for each powdered rock sample by heating the samples in crucibles to 930 °C in a furnace for 30 min. Fusion discs were prepared for analysis using a mixture of ~ 0.7 g of the ignited powder residue and 5.9 g of $Li_2B_4O_7$ plus 0.5 g of $LiNO_3$. The compound mixtures were fused in platinum crucibles at 1050 °C. Whole-rock major and minor element compositions were determined on these fusion discs by X-ray fluorescence (XRF) spectrometry using the PANalytical MagiX PRO instrument at the University of Johannesburg. The accuracy and precision of the analyses were monitored by repeated measurements of certified reference materials (BHVO-2, SARM39) and in-house standards (ST224B). Results for these standards are listed in Supplementary file Table S1 and compare well with previous analyses on the same instrument, as summarized in Tappe et al. (2020).

Trace element compositions were determined at the School of Geosciences, University of the Witwatersrand, using a Perkin Elmer Sciex ELAN DRC-e ICP-MS instrument. Rock powders (50 mg per sample) were dissolved in a mixture of concentrated HF and $HNO_3$ (3:2 ratio) at 40 min digestion time at 240 °C. A high-pressure Teflon vessel in a CEM Mars Express Microwave digester was utilised for the digestion. The remaining contents were evaporated to complete dryness in Teflon beakers during several steps of $HNO_3$ addition and evaporation. After evaporation to complete dryness, samples were diluted to 50 ml with 5 % $HNO_3$, also containing the internal standards Re, Bi, In and Rh suitable for trace element measurements (for further analytical details see Tappe et al., 2022). The quality of the results was monitored using the international standards BCR-2, BIR1 and BHVO-2. A selection of representative analytical data is listed in Table 1 and the complete data set is provided in Supplementary file Table S1.

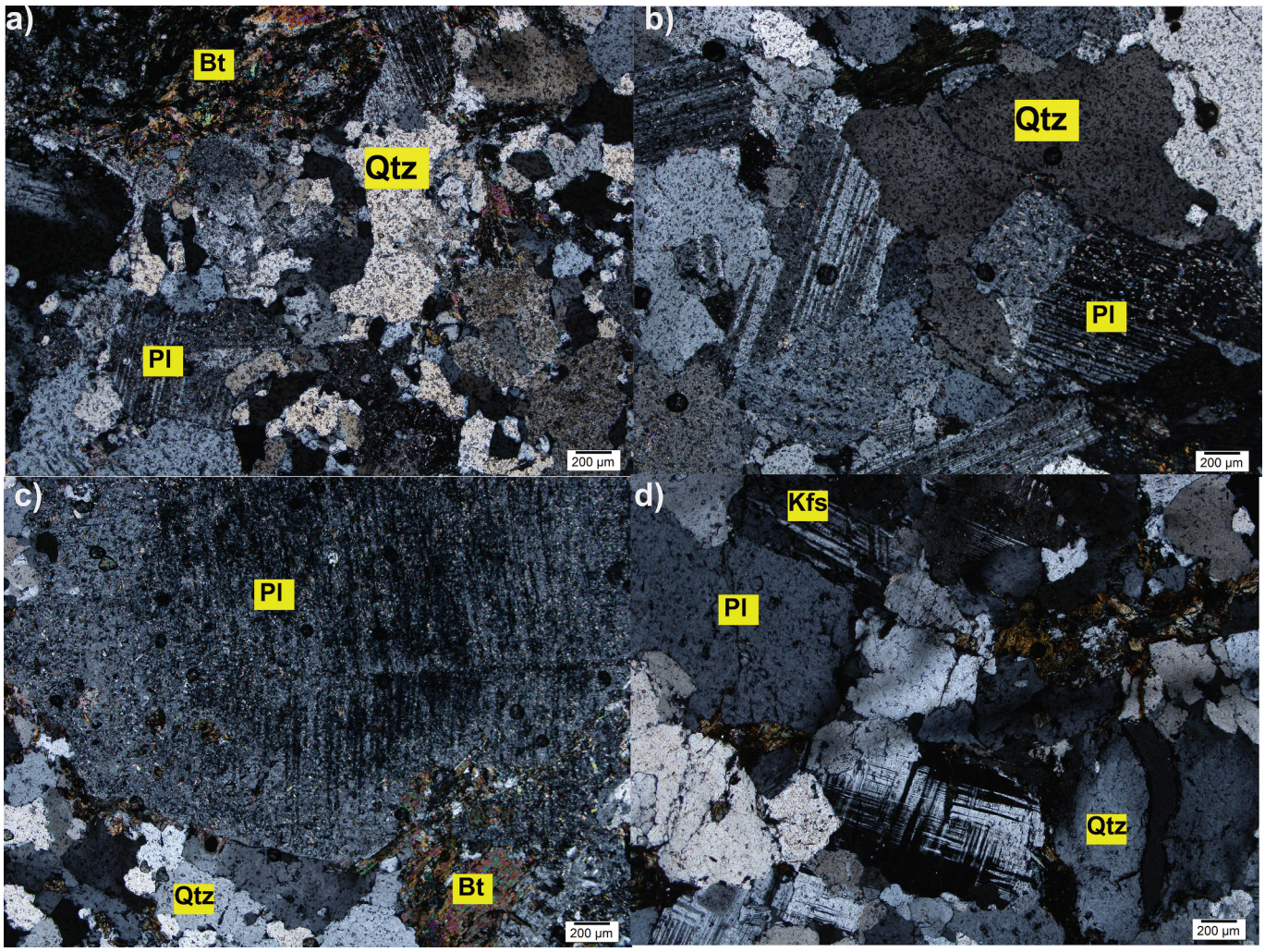



**Fig. 7.** Photomicrographs of thin sections prepared from granitoid intrusives in the Buffalo River Greenstone Belt: a) medium grained granitoid with quartz, plagioclase and biotite sample BR19-57 (Sifula inlier); b) equigranular granitoid dominated by plagioclase and quartz sample BR19-64 (Buffalo inlier); c) a large crystal of plagioclase set in a medium grained groundmass dominated by quartz and biotite sample BR19-67B (Buffalo inlier); d) medium grained granitoid with equigranular plagioclase, quartz and alkali-feldspar, along with smaller accessory biotite sample BR19-67A (Buffalo inlier). Pl = plagioclase, Qtz = quartz, Kfs = alkali feldspar, Bt = biotite.

### *5.3. Whole-rock highly siderophile element (HSE) and Re-Os isotope analyses*

The highly siderophile element concentrations (HSE: Os, Ir, Ru, Pt, Pd, Re) and Os isotopic compositions were determined by isotope dilution mass spectrometry following the methods of Ishikawa et al. (2014, 2017). Approximately 500 mg sample powder aliquots were added into quartz glass tubes (diameter = 14 mm, length = 290 mm), together with isotopic tracer solutions, before digestion in inverse aqua regia for 72 h at 240 °C. The Os concentrations and isotopic compositions were determined by negative thermal ionisation mass spectrometry (N-TIMS) using the Thermo Triton Plus instrument equipped with $10^{13}$ Ohm resistors at JAMSTEC in Japan. The purified Os, after-$CCl_4$ solvent extraction (Cohen and Waters, 1996) and microdistillation (Birck et al., 1997), was loaded in HBr on baked 99.997 % Alfa Aesar Pt wires and covered with a NaOH-$Ba(OH)_2$ activator solution. Analyses of the international Os isotope mass spectrometry standard DROsS (load size 0.2–1 ng) yielded $^{187}Os/^{188}Os$ of 0.16088 ± 4 [2SE, n = 58] and 0.16091 ± 4 (2SE, n = 25) in SEM jumping mode and Faraday cup static mode, respectively. These results are in good agreement with data obtained by other laboratories (0.160924 ± 4 for 10–100 ng; Luguet et al., 2008; 0.160938 ± 22 for 1–3 ng; Liu and Pearson, 2014).

All other HSE concentrations were determined on a Thermo Element-XR ICP-MS instrument at the University of Tokyo in Komaba, Japan. The results reported in Table 2 are blank-corrected, applying the following procedural blanks: Os = 0.07 ± 0.01 pg, Ir = 0.49 ± 0.40 pg, Ru = 2.1 ± 1.5 pg, Pt = 41 ± 37 pg, Pd = 8.6 ± 4.1 pg, Re = 0.30 ± 0.09 pg, and $^{187}Os/^{188}Os$ = 0.198 ± 0.049 (±1S.D.; n = 8). Blank contributions were highly variable depending on the HSE concentrations of the samples analyzed (0.005–1.0 % for Os, 0.048–18 % for Ir, 0.012–16 % for Ru, 0.066–32 % for Pt, 0.058–13 % for Pd, 0.038–26 % for Re, 0.0005–7 % for $^{187}Os/^{188}Os$). The reported analytical uncertainty for each sample entails a full propagation of error sources from the mass spectrometry measurements, plus the blank corrections. Accuracy and precision for our analytical setup was evaluated by measuring mafic and ultramafic reference materials such as BIR-1a, UB-N, GP-13, and JP-1, with concentrations and typical reproducibilities reported in Smart et al. (2019) and Akizawa et al. (2021). Significant variability was occasionally found in the data for ultramafic reference materials, suggesting that the small amounts of material available for analysis (500 mg) are characterized by rather heterogeneous HSE distributions on a small scale. However, BIR-1a and our duplicated komatiitic sample analyses show much better reproducibilities. The observed magnitude of data variation does not affect the conclusions reached in this study.

**Table 1**
Major and trace elements of mafic and ultramafic rocks of the Buffalo River Greenstone Belt.

| Sample | BR19-33B | BR19-33C | BR19-34A | BR19-34B | BR19-42A | BR19-42B | BR19-43A | BR19-43B | BR19-47B |
|---|---|---|---|---|---|---|---|---|---|
| Inlier | Mgunjane | Mgunjane | Mgunjane | Mgunjane | Mgunjane | Mgunjane | Mgunjane | Mgunjane | Mgunjane |
| Rock type | Komatiite | Komatiite | Komatiite | Komatiite | Komatiite | Komatiite | Komatiite | Komatiite | Komatiite |
| Latitude | −28.579 | −28.579 | −28.578 | −28.578 | −28.579 | −28.579 | −28.579 | −28.579 | −28.591 |
| Longitude | 30.586 | 30.586 | 30.588 | 30.588 | 30.588 | 30.588 | 30.588 | 30.588 | 30.585 |
| **Major Elements (wt.%)** | | | | | | | | | |
| $SiO_2$ | 47.6 | 47.0 | 45.0 | 46.0 | 44.1 | 48.5 | 46.5 | 46.9 | 45.4 |
| $TiO_2$ | 0.352 | 0.283 | 0.329 | 0.352 | 0.323 | 0.358 | 0.358 | 0.331 | 0.287 |
| $Al_2O_3$ | 3.75 | 2.84 | 3.32 | 4.18 | 3.03 | 3.43 | 3.71 | 3.47 | 1.96 |
| $Fe_2O_3$ | 12.4 | 12.0 | 13.3 | 11.9 | 13.1 | 10.2 | 14.2 | 12.4 | 10.3 |
| MnO | 0.111 | 0.123 | 0.105 | 0.071 | 0.164 | 0.113 | 0.196 | 0.153 | 0.182 |
| MgO | 27.5 | 27.8 | 26.5 | 27.8 | 26.4 | 27.9 | 22.4 | 25.6 | 26.9 |
| CaO | 0.862 | 1.55 | 2.21 | 1.21 | 2.74 | 1.37 | 7.57 | 4.44 | 6.27 |
| $Cr_2O_3$ | 0.425 | 0.376 | 0.406 | 0.428 | 0.410 | 0.440 | 0.445 | 0.390 | 0.355 |
| NiO | 0.179 | 0.206 | 0.149 | 0.153 | 0.196 | 0.160 | 0.137 | 0.157 | 0.195 |
| LOI | 7.10 | 8.12 | 8.61 | 7.90 | 9.09 | 7.64 | 3.17 | 5.51 | 5.36 |
| Total | 100.3 | 100.3 | 100.0 | 100.1 | 99.56 | 100.0 | 98.66 | 99.38 | 97.28 |
| $Al_2O_3/TiO_2$ | 10.7 | 10.0 | 10.1 | 11.9 | 9.38 | 9.59 | 10.4 | 10.5 | 6.83 |
| **Trace elements (ppm)** | | | | | | | | | |
| Li | 2.46 | 1.40 | 1.17 | 1.50 | 1.80 | 2.27 | 2.28 | 2.53 | 1.03 |
| P | 213 | 150 | 123 | 218 | 94.1 | 146 | 112 | 276 | 46.8 |
| Sc | 24.1 | 16.6 | 18.6 | 27.1 | 22.7 | 17.4 | 18.8 | 19.8 | 17.7 |
| Ti | 2095 | 1661 | 1928 | 2139 | 1957 | 1984 | 2098 | 1990 | 1700 |
| V | 127 | 111 | 126 | 122 | 148 | 117 | 149 | 142 | 93.8 |
| Cr | 3147 | 2724 | 2823 | 2940 | 3162 | 2823 | 3482 | 3063 | 2639 |
| Co | 96.2 | 80.8 | 90.5 | 94.3 | 102 | 88.8 | 92.3 | 90.7 | 86.6 |
| Ni | 1333 | 1480 | 1061 | 1118 | 1450 | 1204 | 1028 | 1191 | 1616 |
| Cu | 82.3 | 126 | 176 | 240 | 580 | 148 | 43.5 | 171 | 8.12 |
| Zn | 68.4 | 68.4 | 75.8 | 73.8 | 71.0 | 71.7 | 55.0 | 56.9 | 46.9 |
| Ga | 4.76 | 3.97 | 4.42 | 5.06 | 4.06 | 4.27 | 4.81 | 4.30 | 3.27 |
| Rb | 0.785 | 0.343 | 0.217 | 0.329 | 0.313 | 0.516 | 0.534 | 1.130 | 0.631 |
| Sr | 10.2 | 19.9 | 29.5 | 13.8 | 25.1 | 11.8 | 13.6 | 18.2 | 24.9 |
| Y | 3.23 | 3.36 | 3.73 | 2.44 | 4.09 | 2.75 | 6.91 | 5.02 | 7.88 |
| Zr | 0.493 | 0.419 | 0.698 | 1.57 | 0.714 | 0.477 | 10.7 | 3.08 | 2.73 |
| Nb | 0.890 | 0.813 | 0.869 | 0.904 | 0.793 | 0.838 | 0.984 | 0.857 | 0.655 |
| Ba | 47.3 | 48.7 | 25.5 | 6.60 | 49.7 | 15.1 | 9.69 | 82.3 | 3.89 |
| Sn | 0.151 | 0.108 | 0.282 | 0.176 | 0.063 | 0.055 | 0.450 | 0.108 | 0.147 |
| Cs | 0.197 | 0.092 | 0.052 | 0.101 | 0.083 | 0.136 | 0.055 | 0.227 | 0.097 |
| La | 0.879 | 1.139 | 0.883 | 0.540 | 0.917 | 0.573 | 0.931 | 0.642 | 0.908 |
| Ce | 1.21 | 2.95 | 2.29 | 1.39 | 1.76 | 1.30 | 2.80 | 1.72 | 2.59 |
| Pr | 0.237 | 0.450 | 0.395 | 0.231 | 0.312 | 0.225 | 0.442 | 0.314 | 0.445 |
| Nd | 1.25 | 2.28 | 2.12 | 1.29 | 1.62 | 1.23 | 2.40 | 1.74 | 2.27 |
| Sm | 0.444 | 0.662 | 0.677 | 0.440 | 0.531 | 0.427 | 0.856 | 0.668 | 0.746 |
| Eu | 0.154 | 0.193 | 0.246 | 0.154 | 0.195 | 0.119 | 0.230 | 0.224 | 0.264 |
| Gd | 0.555 | 0.734 | 0.768 | 0.515 | 0.646 | 0.510 | 1.10 | 0.796 | 1.00 |
| Tb | 0.097 | 0.118 | 0.118 | 0.082 | 0.111 | 0.091 | 0.205 | 0.148 | 0.192 |
| Dy | 0.581 | 0.712 | 0.655 | 0.490 | 0.678 | 0.527 | 1.30 | 0.923 | 1.23 |
| Ho | 0.113 | 0.131 | 0.132 | 0.089 | 0.134 | 0.105 | 0.260 | 0.189 | 0.263 |
| Er | 0.309 | 0.340 | 0.331 | 0.230 | 0.364 | 0.263 | 0.691 | 0.504 | 0.729 |
| Tm | 0.041 | 0.047 | 0.046 | 0.031 | 0.052 | 0.038 | 0.103 | 0.074 | 0.103 |
| Yb | 0.260 | 0.308 | 0.283 | 0.199 | 0.307 | 0.236 | 0.644 | 0.456 | 0.664 |
| Lu | 0.041 | 0.040 | 0.044 | 0.030 | 0.047 | 0.034 | 0.093 | 0.066 | 0.093 |
| Hf | 0.032 | 0.038 | 0.039 | 0.041 | 0.047 | 0.029 | 0.362 | 0.165 | 0.148 |
| Ta | 0.056 | 0.052 | 0.056 | 0.058 | 0.046 | 0.055 | 0.059 | 0.060 | 0.041 |
| W | 0.108 | 0.084 | 0.040 | 0.062 | 0.139 | 0.051 | 0.097 | 0.174 | 0.059 |
| Pb | 0.942 | 1.34 | 1.04 | 0.699 | 5.43 | 6.91 | 0.831 | 0.994 | 0.254 |
| Th | 0.109 | 0.100 | 0.080 | 0.089 | 0.098 | 0.103 | 0.105 | 0.107 | 0.086 |
| U | 0.015 | 0.031 | 0.017 | 0.015 | 0.016 | 0.011 | 0.027 | 0.022 | 0.020 |
| $(La/Sm)_{PM}$ | 1.26 | 1.10 | 0.830 | 0.781 | 1.10 | 0.854 | 0.692 | 0.612 | 0.774 |

| Sample | BR19-47C | BR19-62B | BR19-62C | BR19-47A.cu | BR19-47F | BR19-47H |
|---|---|---|---|---|---|---|
| Inlier | Mgunjane | Mgunjane | Mgunjane | Mngunjane | Mngunjane | Mngunjane |
| Rock type | Komatiite | Komatiite | Komatiite | Komatiite cumulate | Komatiite cumulate | Komatiite cumulate |
| Latitude | −28.591 | −28.591 | −28.591 | −28.591 | −28.591 | −28.591 |
| Longitude | 30.585 | 30.585 | 30.585 | 30.585 | 30.585 | 30.585 |
| **Major Elements (wt.%)** | | | | | | |
| $SiO_2$ | 49.0 | 44.4 | 46.4 | 43.6 | 42.9 | 41.8 |
| $TiO_2$ | 0.313 | 0.272 | 0.294 | 0.199 | 0.193 | 0.172 |
| $Al_2O_3$ | 1.64 | 2.48 | 2.02 | 1.75 | 1.39 | 1.78 |
| $Fe_2O_3$ | 9.57 | 11.8 | 11.1 | 9.08 | 10.5 | 10.2 |
| MnO | 0.169 | 0.198 | 0.167 | 0.243 | 0.207 | 0.174 |
| MgO | 25.3 | 28.4 | 26.6 | 33.2 | 33.2 | 33.3 |
| CaO | 8.33 | 5.18 | 6.85 | 2.67 | 2.42 | 2.73 |
| $Cr_2O_3$ | 0.383 | 0.317 | 0.354 | 0.285 | 0.274 | 0.256 |
| NiO | 0.172 | 0.238 | 0.192 | 0.256 | 0.251 | 0.263 |

(*continued on next page*)

**Table 1** (*continued*)

| | | | | | | | |
|---|---|---|---|---|---|---|---|
| **LOI** | 3.66 | 6.18 | 4.59 | 8.62 | 8.94 | 9.87 | |
| **Total** | 98.54 | 99.44 | 98.61 | 100.2 | 100.5 | 100.4 | |
| **$Al_2O_3/TiO_2$** | 5.23 | 9.10 | 6.87 | 8.81 | 7.19 | 10.3 | |
| **Trace elements (ppm)** | | | | | | | |
| **Li** | 0.829 | 1.11 | 1.01 | 0.702 | 0.511 | 0.722 | |
| **P** | 171 | 53.5 | 60.8 | 65.0 | 93.4 | 80.4 | |
| **Sc** | 20.5 | 17.1 | 19.2 | 12.8 | 10.2 | 10.3 | |
| **Ti** | 1982 | 1683 | 1854 | 1186 | 966 | 870 | |
| **V** | 80.7 | 99.9 | 105 | 66.6 | 46.3 | 54.1 | |
| **Cr** | 2971 | 2500 | 2743 | 2202 | 1582 | 1630 | |
| **Co** | 75.8 | 108 | 94.8 | 108 | 95.7 | 94.6 | |
| **Ni** | 1260 | 1738 | 1428 | 2283 | 1728 | 1784 | |
| **Cu** | 11.3 | 46.7 | 74.2 | 11.8 | 13.0 | 1.79 | |
| **Zn** | 54.8 | 46.9 | 37.4 | 88.2 | 68.8 | 44.5 | |
| **Ga** | 2.05 | 3.35 | 2.58 | 2.69 | 1.85 | 2.27 | |
| **Rb** | 0.591 | 0.576 | 0.331 | 0.276 | 0.482 | 0.207 | |
| **Sr** | 27.3 | 16.9 | 22.4 | 8.48 | 7.66 | 31.0 | |
| **Y** | 6.97 | 5.50 | 5.37 | 3.58 | 3.48 | 3.14 | |
| **Zr** | 3.22 | 2.50 | 2.43 | 10.2 | 10.6 | 8.75 | |
| **Nb** | 0.753 | 0.841 | 0.629 | 0.511 | 0.579 | 0.453 | |
| **Ba** | 18.9 | 11.1 | 27.8 | 4.94 | 5.37 | 28.5 | |
| **Sn** | 0.196 | 0.107 | 0.085 | 0.197 | 0.213 | 0.160 | |
| **Cs** | 0.046 | 0.125 | 0.074 | 0.139 | 0.127 | 0.139 | |
| **La** | 1.16 | 0.859 | 1.29 | 0.522 | 0.825 | 0.571 | |
| **Ce** | 2.88 | 3.41 | 3.35 | 1.32 | 1.68 | 1.54 | |
| **Pr** | 0.570 | 0.461 | 0.499 | 0.216 | 0.357 | 0.248 | |
| **Nd** | 2.80 | 2.46 | 2.38 | 1.16 | 1.72 | 1.28 | |
| **Sm** | 0.915 | 0.797 | 0.764 | 0.435 | 0.527 | 0.441 | |
| **Eu** | 0.337 | 0.246 | 0.328 | 0.111 | 0.170 | 0.123 | |
| **Gd** | 1.10 | 0.921 | 0.905 | 0.538 | 0.602 | 0.512 | |
| **Tb** | 0.206 | 0.167 | 0.163 | 0.102 | 0.106 | 0.092 | |
| **Dy** | 1.28 | 1.03 | 1.01 | 0.663 | 0.655 | 0.568 | |
| **Ho** | 0.254 | 0.204 | 0.199 | 0.133 | 0.124 | 0.113 | |
| **Er** | 0.665 | 0.524 | 0.492 | 0.364 | 0.319 | 0.302 | |
| **Tm** | 0.096 | 0.075 | 0.073 | 0.053 | 0.044 | 0.044 | |
| **Yb** | 0.568 | 0.470 | 0.449 | 0.324 | 0.308 | 0.291 | |
| **Lu** | 0.074 | 0.064 | 0.060 | 0.051 | 0.042 | 0.039 | |
| **Hf** | 0.049 | 0.046 | 0.041 | 0.03 | 0.034 | 0.024 | |
| **Ta** | 0.077 | 0.073 | 0.122 | 0.067 | 0.283 | 0.092 | |
| **W** | 0.258 | 0.414 | 0.462 | 0.511 | 0.420 | 0.398 | |
| **Pb** | 0.091 | 0.086 | 0.085 | 0.057 | 0.056 | 0.045 | |
| **Th** | 0.026 | 0.028 | 0.028 | 0.022 | 0.023 | 0.030 | |
| **U** | 0.808 | 0.686 | 1.08 | 0.764 | 0.996 | 0.824 | |
| **$(La/Sm)_{PM}$** | 0.829 | 1.11 | 1.01 | 0.702 | 0.511 | 0.722 | |

| **Sample** | BR19-23 | BR19-40 | BR19-50 | BR19-52 | BR19-53B | BR19-60 | BR19-03 | BR19-13 |
|---|---|---|---|---|---|---|---|---|
| **Inlier** | Mngunjane | Mngunjane | Mngunjane | Mngunjane | Mngunjane | Sifula | Sifula | Sifula |
| **Rock type** | Actinolite Schist | Actinolite schist | Actinolite schist | Serpentinite | Serpentinite | Actinolite schist | Pillow basalt | Serpentinite |
| **Latitude** | −28.578 | −28.582 | −28.587 | −28.586 | −28.585 | −28.563 | −28.562 | −28.565 |
| **Longitude** | 30.588 | 30.586 | 30.589 | 30.589 | 30.589 | 30.564 | 30.577 | 30.570 |
| **Major Elements (wt.%)** | | | | | | | | |
| **$SiO_2$** | 52.8 | 49.1 | 51.6 | 53.9 | 52.1 | 53.8 | 52.5 | 54.1 |
| **$TiO_2$** | 0.570 | 0.484 | 0.253 | 0.371 | 0.335 | 0.228 | 1.004 | 0.534 |
| **$Al_2O_3$** | 9.89 | 11.54 | 4.40 | 7.06 | 5.83 | 5.54 | 13.28 | 13.81 |
| **$Fe_2O_3$** | 11.3 | 12.0 | 9.94 | 9.49 | 11.1 | 8.74 | 14.6 | 10.1 |
| **MnO** | 0.175 | 0.163 | 0.166 | 0.165 | 0.186 | 0.131 | 0.176 | 0.112 |
| **MgO** | 12.1 | 13.1 | 24.7 | 12.9 | 18.5 | 21.2 | 4.53 | 7.58 |
| **CaO** | 6.65 | 7.05 | 3.31 | 12.5 | 7.72 | 4.36 | 6.25 | 7.65 |
| **$K_2O$** | 0.68 | 0.88 | nd | 0.21 | nd | 0.07 | 0.42 | 1.08 |
| **$Na_2O$** | 1.95 | 1.71 | nd | 1.86 | 0.069 | 0.955 | 5.14 | 2.13 |
| **$Cr_2O_3$** | 0.142 | 0.150 | 0.589 | 0.238 | 0.221 | 0.307 | nd | nd |
| **NiO** | nd | nd | 0.07 | nd | nd | 0.05 | nd | nd |
| **$P_2O_5$** | 0.127 | 0.086 | nd | 0.069 | 0.057 | nd | 0.101 | 0.070 |
| **LOI** | 2.13 | 2.46 | 4.47 | 0.56 | 2.98 | 3.45 | 0.96 | 1.45 |
| **Total** | 100.07 | 98.95 | 100.10 | 98.60 | 99.76 | 100.52 | 99.07 | 99.42 |
| **$Al_2O_3/TiO_2$** | 17.35 | 23.84 | 17.37 | 19.02 | 17.41 | 24.29 | 13.23 | 25.86 |
| **Trace elements (ppm)** | | | | | | | | |
| **Li** | 32.2 | 49.4 | 10.3 | 4.64 | 29.2 | 12.8 | 9.33 | 17.6 |
| **P** | 425 | 398 | 202 | 285 | 243 | 26.3 | 421 | 273 |
| **Sc** | 31.6 | 40.0 | 14.0 | 60.3 | 27.0 | 17.9 | 29.7 | 33.6 |
| **Ti** | 2735 | 3174 | 1195 | 2224 | 1674 | 815 | 6259 | 3113 |
| **V** | 164 | 216 | 82.3 | 283 | 153 | 152 | 361 | 228 |
| **Cr** | 863.4 | 1150 | 3106 | 1696 | 1608 | 2383 | 24.30 | 169.0 |
| **Co** | 49.7 | 51.1 | 64.4 | 50.7 | 66.5 | 69.2 | 47.8 | 43.5 |
| **Ni** | 300.6 | 221.7 | 447.9 | 233.7 | 361.9 | 439.3 | 56.09 | 81.31 |
| **Cu** | 68.7 | 8.70 | 34.8 | 80.4 | 17.63 | 1.69 | 164 | 4.42 |
| **Zn** | 77.2 | 97.7 | 50.2 | 68.0 | 78.3 | 29.5 | 104 | 30.7 |

(*continued on next page*)

**Table 1** (*continued*)

| | | | | | | | | |
|---|---|---|---|---|---|---|---|---|
| **Ga** | 10.9 | 11.3 | 4.33 | 7.74 | 5.97 | 4.10 | 20.2 | 12.6 |
| **Rb** | 14.9 | 26.7 | 0.345 | 4.47 | 0.181 | 1.67 | 6.58 | 28.4 |
| **Sr** | 74.0 | 61.8 | 13.0 | 88.2 | 5.23 | 18.2 | 113 | 108 |
| **Y** | 21.3 | 14.5 | 5.81 | 15.7 | 11.0 | 6.84 | 24.1 | 17.6 |
| **Zr** | nd | 38.0 | 14.8 | 38.0 | 30.0 | 9.8 | 73.0 | 42.0 |
| **Nb** | 3.41 | 2.78 | 1.30 | 1.77 | 1.64 | 0.25 | 3.33 | 2.92 |
| **Ba** | 68.7 | 42.2 | 59.1 | 56.1 | 3.83 | 35.7 | 116 | 70.2 |
| **Sn** | 0.384 | 0.647 | 0.254 | 0.183 | 0.511 | nd | 0.957 | 0.238 |
| **Cs** | 0.309 | 0.682 | 0.118 | 0.05 | 0.041 | 0.15 | 0.504 | 0.389 |
| **La** | 4.62 | 2.99 | 0.839 | 3.49 | 1.74 | 0.692 | 5.31 | 3.66 |
| **Ce** | 12.2 | 7.65 | 2.54 | 8.85 | 5.28 | 1.90 | 12.8 | 9.70 |
| **Pr** | 1.748 | 1.116 | 0.400 | 1.243 | 0.790 | 0.282 | 1.817 | 1.385 |
| **Nd** | 7.93 | 5.33 | 2.04 | 5.58 | 3.83 | 1.30 | 8.60 | 6.14 |
| **Sm** | 2.18 | 1.73 | 0.676 | 1.64 | 1.16 | 0.438 | 2.59 | 1.76 |
| **Eu** | 0.657 | 0.568 | 0.239 | 0.515 | 0.353 | 0.208 | 1.024 | 0.666 |
| **Gd** | 2.62 | 2.07 | 0.821 | 2.02 | 1.43 | 0.603 | 3.28 | 2.24 |
| **Tb** | 0.473 | 0.397 | 0.159 | 0.374 | 0.274 | 0.124 | 0.607 | 0.412 |
| **Dy** | 3.13 | 2.71 | 1.06 | 2.55 | 1.90 | 0.987 | 3.99 | 2.76 |
| **Ho** | 0.689 | 0.583 | 0.218 | 0.561 | 0.417 | 0.243 | 0.839 | 0.607 |
| **Er** | 1.90 | 1.63 | 0.642 | 1.59 | 1.22 | 0.76 | 2.22 | 1.68 |
| **Tm** | 0.301 | 0.264 | 0.100 | 0.234 | 0.202 | 0.127 | 0.343 | 0.269 |
| **Yb** | 1.91 | 1.64 | 0.710 | 1.50 | 1.29 | 0.87 | 2.08 | 1.77 |
| **Lu** | 0.286 | 0.242 | 0.108 | 0.224 | 0.204 | 0.144 | 0.292 | 0.258 |
| **Ta** | 0.310 | 0.182 | 0.076 | 0.128 | 0.105 | 0.027 | 0.184 | 0.177 |
| **W** | 0.502 | 0.554 | 0.272 | 0.13 | 0.183 | 0.039 | 0.266 | 0.435 |
| **Pb** | 0.823 | 1.39 | 0.260 | 1.54 | 0.233 | 0.571 | 1.66 | 1.30 |
| **Th** | 0.813 | 0.678 | 0.169 | 0.438 | 0.493 | 0.104 | 0.752 | 0.664 |
| **U** | 0.222 | 0.304 | 0.070 | 0.048 | 0.161 | 0.031 | 0.191 | 0.206 |
| **$(La/Sm)_{PM}$** | 1.35 | 1.09 | 0.790 | 1.35 | 0.951 | 1.00 | 1.30 | 1.32 |

| **Sample** | BR19-32 | BR19-53A | BR19-63A | BR19-63B | BR19-55 | BR19-51 |
|---|---|---|---|---|---|---|
| **Inlier** | Mgunjane | Mgunjane | Buffalo Gorge | Buffalo Gorge | Sifula | Mgunjane |
| **Rock type** | Serpentinite | Serpentinite | Pillow basalt | Pillow basalt | Serpentinite | Serpentinite |
| **Latitude** | −28.579 | −28.585 | −28.614 | −28.614 | −28.568 | −28.586 |
| **Longitude** | 30.586 | 30.589 | 30.615 | 30.615 | 30.567 | 30.589 |
| **Major Elements (wt.%)** | | | | | | |
| **$SiO_2$** | 43.3 | 52.7 | 51.2 | 49.9 | 42.3 | 42.2 |
| **$TiO_2$** | 0.206 | 0.452 | 0.864 | 0.705 | bdl | 0.213 |
| **$Al_2O_3$** | 3.827 | 14.71 | 14.05 | 12.11 | 1.66 | 4.03 |
| **$Fe_2O_3$** | 10.1 | 9.07 | 12.4 | 11.6 | 8.86 | 11.2 |
| **MnO** | 0.093 | 0.128 | 0.166 | 0.155 | 0.163 | 0.139 |
| **MgO** | 32.0 | 7.38 | 7.16 | 10.1 | 33.8 | 30.7 |
| **CaO** | 0.35 | 8.34 | 7.95 | 8.79 | 2.33 | 1.98 |
| **$K_2O$** | nd | 1.10 | 0.403 | 1.29 | nd | nd |
| **$Na_2O$** | nd | 3.45 | 2.77 | 2.03 | nd | nd |
| **$Cr_2O_3$** | 0.887 | nd | nd | 0.063 | 0.469 | 0.719 |
| **NiO** | 0.155 | nd | nd | nd | 0.328 | 0.138 |
| **$P_2O_5$** | nd | 0.08 | 0.08 | 0.06 | nd | nd |
| **$V_2O_5$** | nd | nd | 0.053 | nd | nd | nd |
| **LOI** | 9.41 | 1.25 | 1.86 | 1.31 | 9.61 | 8.78 |
| **Total** | 99.05 | 99.03 | 98.18 | 98.35 | 98.32 | 99.34 |
| **$Al_2O_3/TiO_2$** | 18.58 | 32.5 | 16.3 | 17.2 | | 18.9 |
| **Trace elements (ppm)** | | | | | | |
| **Li** | 15.6 | 16.2 | 34.2 | 27.6 | 1.56 | 1.96 |
| **P** | 267 | 317 | 334 | 251 | 33.0 | 172 |
| **Sc** | 38.2 | 31.0 | 33.8 | 34.9 | 6.92 | 9.01 |
| **Ti** | 2362 | 2725 | 5415 | 4356 | 195 | 867 |
| **V** | 214 | 192 | 296 | 246 | 33 | 59.4 |
| **Cr** | 1481 | 179.4 | 39.78 | 433.1 | 1890 | 3654 |
| **Co** | 89 | 36.2 | 50.8 | 54.4 | 110 | 95.6 |
| **Ni** | 520.5 | 56.63 | 94.49 | 141.2 | 2752 | 934.2 |
| **Cu** | 674 | 33.1 | 96.0 | 5.08 | 10.6 | 4.11 |
| **Zn** | 80.7 | 51.3 | 79.2 | 64.8 | 45.1 | 62.2 |
| **Ga** | 11.1 | 12.4 | 16.9 | 11.8 | 1.19 | 4.43 |
| **Rb** | 16.1 | 25.5 | 25.1 | 78.4 | 0.051 | 0.377 |
| **Sr** | 45.8 | 138 | 177 | 82.4 | 6.26 | 14.1 |
| **Y** | 13.0 | 15.7 | 20.4 | 16.5 | 1.14 | 6.50 |
| **Zr** | 39.7 | 39.0 | 49.6 | 40.0 | 3.00 | 15.4 |
| **Nb** | 2.60 | 2.92 | 2.80 | 2.30 | 0.154 | 2.23 |
| **Ba** | 63.4 | 97.0 | 82.4 | 115 | 3.77 | 9.32 |
| **Sn** | 0.754 | 0.608 | 0.444 | 0.553 | 0.593 | 0.621 |
| **Cs** | 0.114 | 0.355 | 0.299 | 0.885 | 0.041 | 0.126 |
| **La** | 4.92 | 3.27 | 3.47 | 2.58 | 0.527 | 0.952 |
| **Ce** | 11.3 | 8.28 | 8.77 | 7.03 | 1.06 | 2.89 |
| **Pr** | 1.51 | 1.20 | 1.31 | 1.05 | 0.131 | 0.443 |
| **Nd** | 6.51 | 5.68 | 6.20 | 5.01 | 0.513 | 2.21 |
| **Sm** | 1.56 | 1.82 | 1.96 | 1.63 | 0.141 | 0.713 |

(*continued on next page*)

**Table 1** (*continued*)

| | | | | | | |
|---|---|---|---|---|---|---|
| **Eu** | 0.502 | 0.701 | 0.725 | 0.62 | 0.195 | 0.230 |
| **Gd** | 1.78 | 2.14 | 2.46 | 2.03 | 0.173 | 0.902 |
| **Tb** | 0.313 | 0.411 | 0.461 | 0.385 | 0.032 | 0.171 |
| **Dy** | 2.04 | 2.71 | 3.11 | 2.63 | 0.211 | 1.13 |
| **Ho** | 0.441 | 0.587 | 0.679 | 0.57 | 0.047 | 0.243 |
| **Er** | 1.28 | 1.64 | 2.00 | 1.67 | 0.131 | 0.669 |
| **Tm** | 0.196 | 0.261 | 0.294 | 0.244 | 0.021 | 0.103 |
| **Yb** | 1.26 | 1.66 | 1.90 | 1.57 | 0.145 | 0.663 |
| **Lu** | 0.188 | 0.246 | 0.281 | 0.233 | 0.022 | 0.098 |
| **Ta** | 0.156 | 0.178 | 0.168 | 0.149 | 0.001 | 0.105 |
| **W** | 0.130 | 0.079 | 0.206 | 0.367 | 0.133 | 0.898 |
| **Pb** | 0.917 | 2.66 | 4.87 | 2.61 | 1.88 | 0.600 |
| **Th** | 0.552 | 0.753 | 0.337 | 0.46 | 0.053 | 0.165 |
| **U** | 0.167 | 0.175 | 0.086 | 0.093 | 0.019 | 0.067 |
| **$(La/Sm)_{PM}$** | 2.01 | 1.15 | 1.13 | 1.01 | 2.39 | 0.850 |

nd = not detected; PM = Primitive Mantle-normalised.

### 5.4. U-Pb zircon geochronology

Four granitoid samples, each of approximately 500 g weight, were processed for zircon liberation using the SELFRAG instrument for rock fragmentation by high-voltage discharge at the University of Pretoria, South Africa. The fragmented material was sieved using a 250 μm disposable nylon mesh. After magnetic separation, the non-magnetic fractions were processed through heavy liquid separation using sodium polytungstate (NaPT) with a density of 2.9 g/ml. Representative zircon crystals were handpicked from the non-magnetic heavy mineral fractions and were mounted in epoxy resin and polished to expose their interiors. The mounted zircon crystals were examined by cathodoluminescence (CL) and backscattered electron (BSE) imaging using the JEOL JSM 5600 and VEGA3 TESCAN scanning electron microscopes at the University of Johannesburg, South Africa.

In situ U-Pb zircon isotope ratio measurements were performed by laser ablation multi-collector inductively coupled plasma mass spectrometry (LA-MC-ICP-MS) at the University of Johannesburg. The LA-MC-ICP-MS setup consists of a RESOlution SE 193 nm excimer laser ablation system (Australian Scientific Instruments) coupled to a Nu Plasma-II mass spectrometer (Nu Instruments). Supplementary file 1 comprises a detailed LA-MC-ICP-MS method description, and only a brief method summary is provided here.

The sensitivity of the MC-ICP-MS instrument was optimized twice a day during continuous 35 μm wide line ablations on an in-house standard applying a laser energy of 4 mJ and a 1.4 Hz repetition rate at a scan speed of 0.003 mm/s. Sample ablations were performed in a Laurin Technic dual-volume cell in a helium atmosphere (0.3 l/min gas flow). The helium sample gas was mixed with argon carrier gas (0.8 l/min gas flow) prior to entering the ICP-MS instrument. Using 25 μm laser spot sizes, ablation pits were drilled with the excimer laser at a relatively low fluence of 1.0 J/cm$^2$, equivalent to a nominal energy of < 4 mJ at an attenuator setting of 12.5 %. Prior to each spot measurement, mineral surfaces were 'cleaned' with two pre-ablation laser pulses. The intensities of the $^{238}$U (H8) and $^{232}$Th (H7) ion beams were measured with Faraday detectors, whereas atomic masses $^{208}$Pb (IC0), $^{207}$Pb (IC1), $^{206}$Pb (IC2), $^{204}$Pb+$^{204}$Hg (IC3) and $^{202}$Hg (IC4) were measured with ion counters (see Smart et al., 2021). Calculations of isotope ratios and U-Th-Pb radiometric ages were performed with reference to the following primary zircon calibration standards: OGC1 (3465 ± 0.6 Ma), A1772 (2711 ± 3 Ma) and A382 (1877 ± 2 Ma). Reference material used to check data accuracy included zircons from the Cape Donnington Quartz Gabbro Norite Gneiss (CDQGNG). A $^{207}$Pb/$^{206}$Pb age of 1853 ± 16 Ma was obtained for this zircon and compares well with the accepted age of 1850 Ma by Black et al. (2003). For our standard-sample bracketing approach, up to 15 spot analyses of 'unknowns' were embedded into 5 spot measurements on the calibration standards. The raw data were reduced with a VB Excel based in-house software. The IsoplotR program by Vermeesch (2018) was used for additional age calculations and data visualization. The recommended $^{238}$U/$^{235}$U ratio of 137.818 ± 0.0225 was used for U-Pb age calculations, employing the decay constants of $9.8485 \times 10^{-10}$ a$^{-1}$ for $^{235}$U and $1.55125 \times 10^{-10}$ a$^{-1}$ for $^{238}$U (Steiger and Jäger, 1977). All age uncertainties are quoted at the 2-sigma level throughout the text.

## 6. Results

### 6.1. Ultramafic and mafic volcanic rocks

#### 6.1.1. Major and trace elements

The major and trace element compositions of the Buffalo River Greenstone Belt volcanic rocks are listed in Table 1. Given the effects of low-grade metamorphism and possible late-stage alteration of Archean greenstones, it is crucial to interpret their geochemical signatures with caution. As a first step, each whole-rock analysis is recalculated on an anhydrous basis to avoid the chemical effects of secondary hydration. For the 64 mafic–ultramafic volcanic rocks analysed in this study, MgO is used in binary variation diagrams to identify fractionation trends (Fig. 8). In the $SiO_2$ versus MgO diagram (Fig. 8a), the mafic to ultramafic volcanic rocks are classified as basalts, komatiitic basalts and komatiites, plus associated cumulates, using the scheme of Barnes and Arndt (2019). The spinifex textured komatiites of the Buffalo River Greenstone Belt are characterised by high MgO ranging between 23 and 35.6 wt%, whereas $SiO_2$ varies between 46 and 53 wt%. These komatiites are amongst the most MgO rich lavas of the Kaapvaal craton. The basal cumulates of the komatiite lava flows contain > 36 wt% MgO (e.g., BR19-47 and BR19-62). Furthermore, both the actinolite- and tremolite schists classify geochemically as komatiitic basalts and komatiites. The samples that fall within the komatiitic basalt field have MgO contents that range between 12.6 and 14.3 wt% at 51 to 54.7 wt% $SiO_2$. The actinolite schists classify geochemically as komatiites but have slightly higher $SiO_2$ and $Al_2O_3$ contents than the spinifex textured komatiites. Massive serpentinites of komatiitic affinity have MgO contents between 28 and 35 wt%, overlapping with those of the spinifex textured komatiites, but it remains uncertain by how much MgO was increased due to serpentinization. The negative $Al_2O_3$ versus MgO correlation is indicative of olivine or pyroxene fractionation that may be recorded by the non-cumulate rocks (Fig. 8d). The $TiO_2$ and MgO contents also show a negative correlation possibly due to pyroxene fractionation (Fig. 8b). The CaO versus MgO diagram lacks discernible trends, which is probably caused by Ca mobility during alteration (Fig. 8c).

We use the classification method of Pearce and Reagan (2019) to study the relationship between $SiO_2$, MgO and $TiO_2$ for volcanic rocks of the Buffalo River Greenstone Belt further (Fig. 9). In a $SiO_2$-MgO classification diagram, the wide compositional range of our samples occupies the fields of low silica boninites (LSB), high silica boninites (HSB), basaltic andesites and basalts (Fig. 9a). The spinifex textured

**Table 2**
HSE and Re-Os isotopic data for the Buffalo River komatiites and associated basalts.

| Sample | Os (ppb) | Ir (ppb) | Ru (ppb) | Pt (ppb) | Pd (ppb) | Re (ppb) | $^{187}Re/^{188}Os$ | 2sm | $^{187}Os/^{188}Os$ | 2sm | γOs [i] |
|---|---|---|---|---|---|---|---|---|---|---|---|
| ***Spinifex Al-depleted*** | | | | | | | | | | | |
| BR19-22 | 1.01 | 1.13 | 4.83 | 4.81 | 4.33 | 0.0119 | 0.0564 | 0.00210 | 0.12293 | 0.00013 | 15.9 |
| BR19-33A | 1.47 | 1.44 | 4.52 | 4.50 | 1.02 | 0.0095 | 0.0310 | 0.00070 | 0.10907 | 0.00008 | 3.9 |
| BR19-33B | 1.35 | 1.44 | 4.44 | 4.17 | 2.48 | 0.0045 | 0.0160 | 0.00180 | 0.11066 | 0.00008 | 6.3 |
| BR19-33C | 1.42 | 1.31 | 4.37 | 4.61 | 1.17 | 0.0121 | 0.0413 | 0.00210 | 0.15827 | 0.00008 | 51 |
| BR19-33D | 1.44 | 1.42 | 4.26 | 4.70 | 2.36 | 0.0032 | 0.0106 | 0.00130 | 0.11189 | 0.00010 | 7.8 |
| BR19-33E | 1.44 | 1.32 | 4.42 | 4.83 | 4.31 | 0.0051 | 0.0170 | 0.00140 | 0.10927 | 0.00005 | 4.9 |
| BR19-33F | 1.55 | 1.43 | 4.67 | 5.17 | 0.75 | 0.0062 | 0.0192 | 0.00120 | 0.12084 | 0.00007 | 16 |
| BR19-34A | 1.48 | 1.49 | 4.18 | 5.39 | 2.78 | 0.0028 | 0.0090 | 0.00120 | 0.11605 | 0.00006 | 12 |
| BR19-34B | 1.33 | 1.36 | 4.46 | 5.84 | 2.78 | 0.0133 | 0.0480 | 0.00180 | 0.13744 | 0.00045 | 30.4 |
| BR19-42A | 1.65 | 1.47 | 4.53 | 4.83 | 1.04 | 0.0092 | 0.0269 | 0.00120 | 0.12498 | 0.00007 | 19.6 |
| BR19-42B | 1.67 | 1.66 | 4.68 | 5.43 | 3.92 | 0.0091 | 0.0264 | 0.00160 | 0.12137 | 0.00010 | 16.1 |
| BR19-42C | 1.66 | 1.25 | 4.19 | 3.97 | 3.22 | 0.0174 | 0.0506 | 0.00130 | 0.13975 | 0.00006 | 32.5 |
| BR19-42C* | 1.61 | 1.38 | 4.29 | 3.76 | 3.13 | 0.0249 | 0.0745 | 0.00150 | 0.13999 | 0.00024 | 31.4 |
| BR19-43A | 0.786 | 0.970 | 4.20 | 5.27 | 2.76 | 0.0167 | 0.1021 | 0.00360 | 0.11278 | 0.00021 | 3.4 |
| BR19-43B | 1.00 | 1.01 | 4.52 | 5.01 | 2.14 | 0.0209 | 0.1007 | 0.00330 | 0.11157 | 0.00024 | 2.3 |
| BR19-47A | 1.20 | 1.18 | 3.95 | 5.92 | 3.67 | 0.0114 | 0.0458 | 0.00170 | 0.10760 | 0.00008 | 1.7 |
| BR19-47B | 1.09 | 1.03 | 3.63 | 3.60 | 2.25 | 0.0091 | 0.0401 | 0.00130 | 0.10807 | 0.00009 | 2.4 |
| BR19-47C | 1.09 | 1.12 | 3.52 | 4.45 | 2.64 | 0.0096 | 0.0422 | 0.00150 | 0.10877 | 0.00019 | 3 |
| BR19-47E | 1.36 | 1.26 | 4.08 | 4.77 | 2.19 | 0.0086 | 0.0306 | 0.00140 | 0.11112 | 0.00024 | 5.9 |
| BR19-47G | 1.28 | 1.20 | 3.92 | 4.28 | 1.86 | 0.0066 | 0.0248 | 0.00170 | 0.10829 | 0.00010 | 3.5 |
| BR19-62A | 1.90 | 1.73 | 3.42 | 2.56 | 1.52 | 0.0090 | 0.0227 | 0.00060 | 0.10664 | 0.00004 | 2.1 |
| BR19-62B | 1.09 | 1.06 | 3.07 | 4.14 | 2.72 | 0.0111 | 0.0487 | 0.00210 | 0.10851 | 0.00006 | 2.4 |
| BR19-62C | 1.20 | 1.05 | 3.71 | 4.04 | 2.23 | 0.0091 | 0.0364 | 0.00170 | 0.10794 | 0.00006 | 2.5 |
| BR19-62D | 1.21 | 1.12 | 3.81 | 3.86 | 2.28 | 0.0155 | 0.0614 | 0.00230 | 0.10842 | 0.00004 | 1.5 |
| BR19-62E | 1.18 | 1.00 | 3.55 | 3.03 | 1.48 | 0.0087 | 0.0353 | 0.00210 | 0.10855 | 0.00010 | 3.2 |
| BR19-62F | 1.39 | 1.05 | 3.33 | 4.13 | 2.20 | 0.0066 | 0.0228 | 0.00100 | 0.11002 | 0.00011 | 5.3 |
| BR19-62G | 1.36 | 1.28 | 4.20 | 3.75 | 2.83 | 0.0120 | 0.0422 | 0.00160 | 0.10743 | 0.00004 | 1.7 |
| BR19-62H | 1.09 | 1.03 | 3.61 | 3.60 | 1.92 | 0.0072 | 0.0318 | 0.00130 | 0.10820 | 0.00007 | 3 |
| BR19-62I | 1.30 | 1.22 | 4.03 | 4.30 | 2.61 | 0.0049 | 0.0182 | 0.00140 | 0.10816 | 0.00008 | 3.8 |
| ***Cumulates*** | | | | | | | | | | | |
| BR19-47A CU | 1.02 | 1.03 | 3.47 | 2.79 | 0.686 | 0.0053 | 0.0250 | 0.00860 | 0.10846 | 0.00011 | 3.68 |
| BR19-47F | 2.00 | 1.84 | 3.39 | 1.96 | 1.04 | 0.0071 | 0.0170 | 0.00050 | 0.10684 | 0.00008 | 2.57 |
| ***Al-undepleted komatiites*** | | | | | | | | | | | |
| BR19-18 | 2.93 | 2.57 | 5.69 | 1.38 | 1.20 | 0.0140 | 0.0229 | 0.00070 | 0.10538 | 0.00004 | 0.819 |
| BR19-18* | 2.53 | 2.31 | 5.81 | 1.35 | 1.65 | 0.0224 | 0.0425 | 0.00100 | 0.10652 | 0.00017 | 0.789 |
| BR19-32 | 1.09 | 1.24 | 6.10 | 15.3 | 19.3 | 0.0278 | 0.125 | 0.00180 | 0.24543 | 0.00010 | 6.95 |
| BR19-32* | 1.03 | 1.14 | 6.17 | 15.4 | 19.6 | 0.0347 | 0.165 | 0.00400 | 0.25414 | 0.00006 | 44.9 |
| BR19-45 | 0.632 | 0.500 | 3.27 | 6.88 | 17.9 | 0.1748 | 1.35 | 0.01840 | 0.23490 | 0.00015 | 1197 |
| BR19-45* | 0.585 | 0.605 | 3.82 | 4.87 | 9.16 | 0.1357 | 1.13 | 0.01470 | 0.22864 | 0.00011 | 985 |
| BR19-51 | 0.546 | 0.593 | 4.07 | 8.37 | 3.51 | 0.0218 | 0.192 | 0.00570 | 0.13401 | 0.00012 | 78.8 |
| BR19-55 | 0.440 | 0.258 | 5.42 | 6.58 | 4.92 | 0.8022 | 9.44 | 0.30740 | 0.69208 | 0.00051 | 9007 |
| BR19-60 | 0.048 | 0.104 | 0.850 | 2.85 | 5.28 | 0.0055 | 0.554 | 0.03230 | 0.15500 | 0.00061 | 428 |
| BR19-61 | 1.96 | 1.75 | 4.41 | 2.63 | 2.95 | 0.0060 | 0.0146 | 0.00060 | 0.10589 | 0.00005 | 1.79 |
| ***Al-undepleted (komatiitic basalts)*** | | | | | | | | | | | |
| BR19-50 | 0.989 | 0.709 | 3.667 | 25.7 | 39.2 | 0.1469 | 0.724 | 0.01100 | 0.2136 | 0.0001 | 590 |
| BR19-52 | 0.042 | 0.006 | ND | 0.035 | ND | 0.8175 | 1854 | 39.47 | 145.1 | 3.6 | 1,788,133 |
| ***Basalts*** | | | | | | | | | | | |
| BR19-03 | 0.084 | 0.017 | 0.191 | 7.11 | 16.3 | 1.238 | 153 | 4 | 8.991 | 0.021 | 147,787 |
| BR19-03* | 0.059 | 0.015 | 0.060 | 7.40 | 15.3 | 0.899 | 228 | 6 | 16.33 | 0.05 | 220,040 |
| BR19-13 | 0.033 | 0.045 | 0.362 | 21.0 | 28.6 | 0.3025 | 68.2 | 1.4 | 4.363 | 0.014 | 65,726 |
| BR19-13* | 0.033 | 0.042 | 0.450 | 13.8 | 25.3 | 0.2529 | 53.0 | 0.6 | 3.412 | 0.023 | 51,026 |
| BR19-20 | 0.145 | 0.016 | 0.032 | 0.198 | 0.154 | 1.437 | 384 | 18 | 53.92 | 0.25 | 368,986 |
| BR19-20* | 0.149 | 0.017 | 0.048 | 0.133 | 0.167 | 1.417 | 380 | 11 | 55.73 | 0.35 | 364,478 |
| BR19-46 | 0.401 | 0.322 | 1.09 | 3.32 | 7.75 | 0.1825 | 2.32 | 0.03 | 0.5839 | 0.0008 | 2116 |
| BR19-46* | 0.478 | 0.380 | 1.31 | 4.94 | 8.76 | 0.2032 | 2.15 | 0.03 | 0.5066 | 0.0011 | 1953 |
| BR19-53A | 0.015 | 0.006 | ND | 0.043 | ND | 0.4269 | 893 | 26 | 42.44 | 0.92 | 862,951 |
| BR19-63A | 0.067 | 0.197 | 0.114 | 14.1 | 13.1 | 0.5785 | 79.6 | 2.3 | 7.200 | 0.022 | 76,636 |
| BR19-63B | 0.130 | 0.303 | 0.290 | 12.1 | 8.82 | 0.0368 | 1.38 | 0.02 | 0.2129 | 0.0003 | 1227 |
| BR19-66 | 0.039 | 0.008 | ND | 0.0552 | ND | 1.113 | 2551 | 83 | 133.0 | 3.4 | 2464516 |

*Replicates of the same powder.
ND = Not detected.
The initial γOs values were calculated using the age of the 3470 Ma granitoid.

komatiites fall within the low silica boninite field in Fig. 9a but are identified as komatiites in Fig. 9b. The komatiitic basalt samples classify geochemically as low silica boninites (Fig. 9a). Using the Si8-Ti8 projections of Pearce and Reagan (2019), the komatiitic basalts cluster within the 'siliceous high magnesium basalt' or SHMB field (Fig. 9c). Samples identified by us as tholeiitic basalts extend between boninite, basalt and HMA/BADR in Fig. 9b. We use Fig. 9d (after Shervais, 1982) to further classify the tholeiitic basalts in the Ti/1000 versus V diagram. Our samples fall within the island arc basalt (IAB) and mid-ocean ridge basalt (MORB) fields.

Although komatiites are typically grouped on the basis of their $Al_2O_3/TiO_2$ ratios, some of our samples cannot be further subdivided with confidence because of their very low $TiO_2$ contents, which results in extremely high $Al_2O_3/TiO_2$. These samples have therefore been excluded from further grouping. In a $(Gd/Yb)_N$ versus $(Al/Ti)_N$ diagram (after Barnes and Arndt, 2019; Fig. 9e), the spinifex textured samples

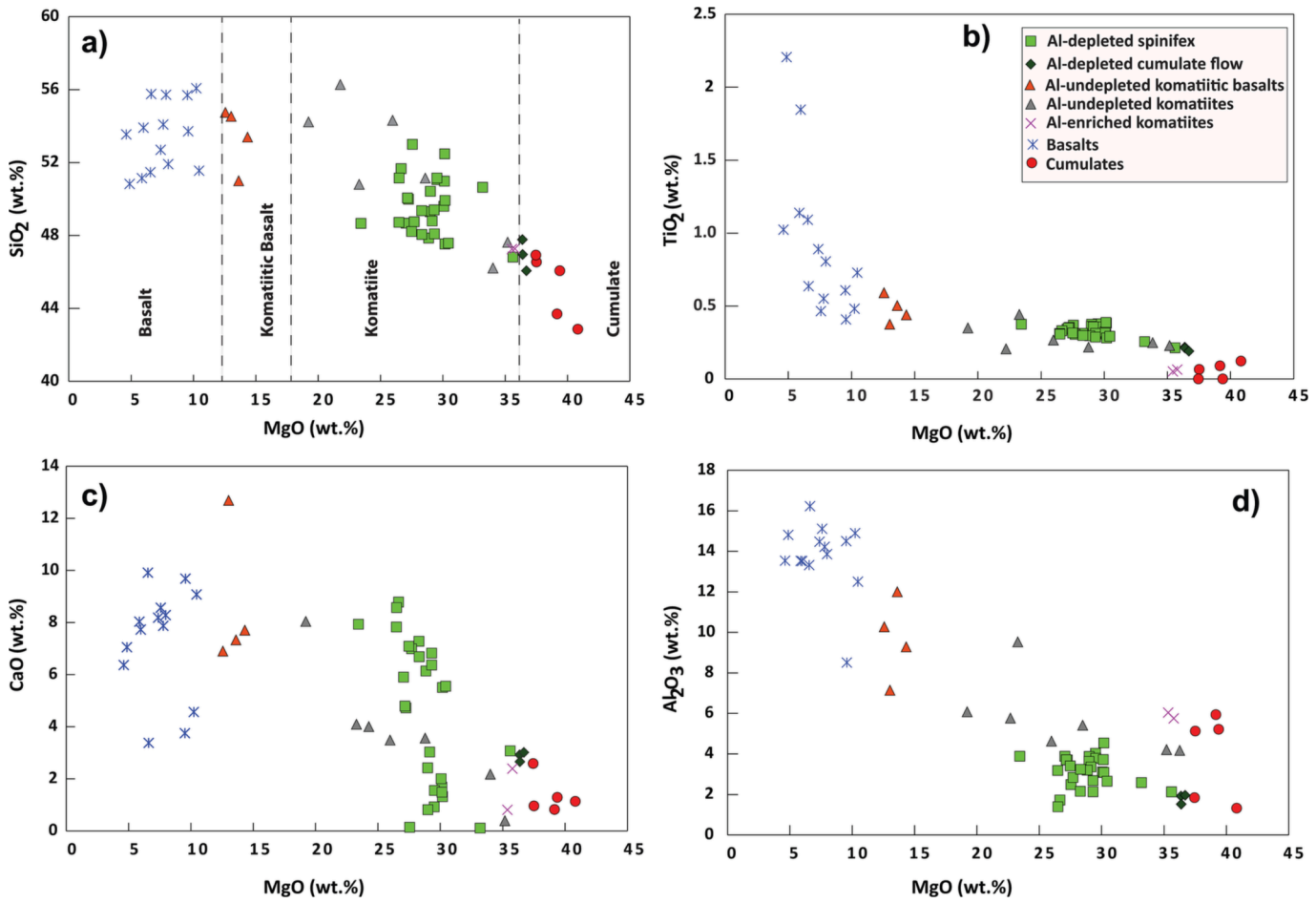



**Fig. 8.** Bivariate plots of selected major elements vs MgO for mafic and ultramafic rock types in the Buffalo River Greenstone Belt. a) $SiO_2$; b) $TiO_2$; c) CaO; and d) $Al_2O_3$. The subdivision of the various mafic–ultramafic rock types on the basis of MgO content (a) is after Barnes and Arndt (2019).

classify as Al-depleted komatiites with $(Al/Ti)_N$ between 0.31 and 0.58. The cumulate rocks of the komatiite lava flow also fall along the Al-depleted komatiite trend with $(Al/Ti)_N$ ratios between 0.41 and 0.57. We note that samples that are petrographically identified as actinolite- and tremolite schists belong to both the Al-undepleted ($Al/Ti_N$ between 0.89 and 1.93) and Al-enriched komatiite varieties ($Al/Ti_N > 5.5$). The basalts have $(Al/Ti)_N$ ratios varying between 0.31 and 1.84, which corresponds to the Al-Ti systematics of the Al-depleted and the Al-undepleted komatiites. The Al-enriched basalts have lower $(Al/Ti)_N$ ratios than the komatiites because of their higher $TiO_2$ contents. The Al-depleted spinifex textured komatiite samples have the highest $(Gd/Yb)_N$ at low (Al/Ti) compared to the komatiitic basalts and basalts from the same volcanic succession (Fig. 9e). Five cumulate rock samples with > 38 wt% MgO classify as Al-depleted, Al-undepleted and Al-enriched komatiite types. The $(Al/Ti)_N$ ratios of the Al-enriched komatiite cumulates range between 2.43 and 6.93.

Chromium and Ni exhibit positive correlations with MgO (Fig. 10a, b). The compatible behaviour of Cr is consistent with the fractionation of a Cr-rich phase, possibly chromite or pyroxene, which is in agreement with the negative trend observed for $Al_2O_3$ and MgO (not shown). The volcanic rocks exhibit increasing La and Nb contents with decreasing MgO (Fig. 10c, d). The basalts are more enriched in La and Nb (2–15 ppm La and 2–13 ppm Nb) than the spinifex textured komatiites, which contain < 1.5 ppm La and < 0.9 ppm Nb.

Incompatible trace element patterns are plotted in Fig. 11 and Supplementary Fig. 1, normalised to the primitive mantle values of Palme and O'Neill (2014). The Al-depleted spinifex textured komatiites are characterised by very low incompatible trace element concentrations. The diagram shows a slight enrichment of the LREE over the HREE for the Al-depleted komatiites ($La/Sm_N = 0.58–1.34$). Ultramafic cumulates from the komatiite lava flows are characterised by similar REE patterns, albeit at lower concentration levels than for the spinifex textured komatiites. The Al-undepleted komatiites are characterised by slight enrichment in incompatible elements compared to the Al-depleted komatiites, and they tend to have smooth flat patterns from the LREE to the HREE. We furthermore note elevated Th contents and a negative Nb anomaly in the normalised multi-element diagram (Fig. 11b). The Al-undepleted komatiites from the Buffalo River Greenstone Belt have similar incompatible trace element patterns compared to those of their counterparts from the Weltevreden Formation in the Barberton Greenstone Belt (Fig. 11b). The Al-undepleted komatiitic basalts have similar trace element patterns to the Al-undepleted komatiites, but at slightly higher concentration levels (Fig. 11c). These komatiitic basalts are generally distinguished by their spatial association with the Al-undepleted komatiites of the central inlier. The Al-enriched komatiites are characterised by a strong depletion in incompatible trace elements at HREE enrichment, with normalized La/Sm between 0.5 and 1.0. These trace element patterns are similar to those of the Al-enriched komatiites from the Commondale Greenstone Belt (Fig. 11d). The komatiite cumulates are characterised by a variety of trace element patterns (Fig. 11e). The Al-depleted cumulate samples show a slight LREE enrichment over the HREE. The Al-enriched cumulates have extreme LREE depletion and HREE enrichment, similar to the Al-enriched komatiite lava flows. The basalts have higher incompatible trace element contents at 5 to 20 times primitive mantle values compared to the komatiites (Fig. 11e). The basalts are generally enriched in the LREE

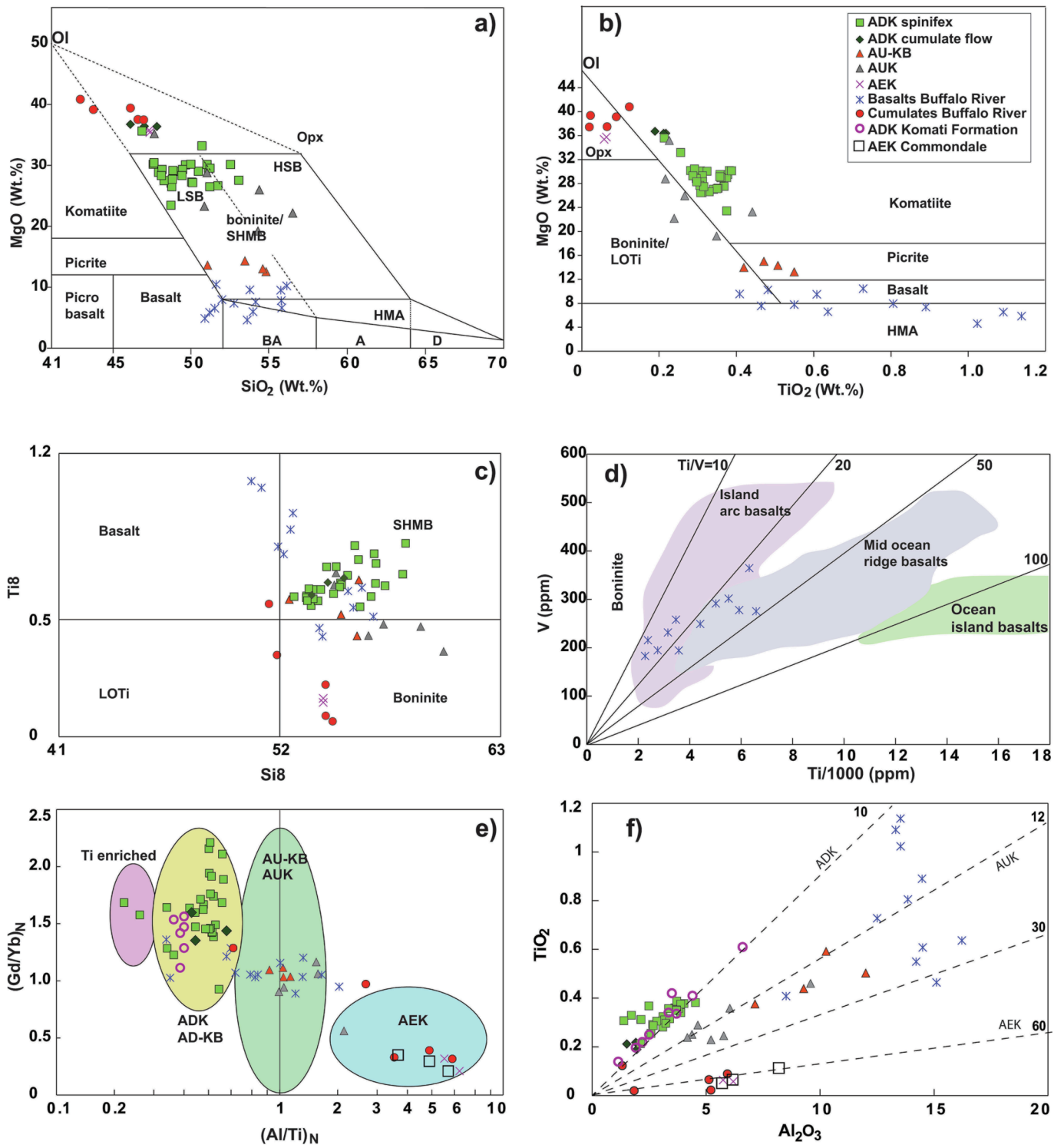



**Fig. 9.** Major and minor element classification diagrams after Pearce and Reagan 2019 (a-c) and Shervais (1982) (d) for the volcanic rocks from the Buffalo River Greenstone Belt: a) MgO vs $SiO_2$; b) MgO vs $TiO_2$; c) Ti8 vs Si8, where Si8 = $SiO_2$ + (MgO–8)/3.82, for MgO > 8 and Ti8 = 42$TiO_2$/(50–MgO), for MgO > 8; and d) V vs Ti/1000; e) classification of the Buffalo River komatiites into Al-depleted, Al-undepleted and Al-enriched types on the basis of $(Al/Ti)_N$ vs $(Gd/Yb)_N$ is after Barnes and Arndt (2019); f) classification of the Buffalo River komatiites into Al-depleted, Al-undepleted and Al-enriched types on the basis of $Al_2O_3$ vs $TiO_2$ (in wt%). Best fit trends representing $Al_2O_3/TiO_2$ ratios. Data for komatiites from the Komati Formation are taken from Robin-Popieul et al. (2012) and those from the Commondale Greenstone Belt are taken from Wilson (2019). Elements are normalised to the primitive mantle values recommended by Palme and O'Neill (2014). ADK = Al-depleted komatiites, AUK = Al-undepleted komatiites, AEK = Al-enriched komatiites, AUK-KB = Al-undepleted komatiitic basalts, SHMB = silicieous high-Mg basalt, A = andesite, D = dacite, LOTi = low Ti basalt, LSB = low silica boninite, HSB = high silica boninite, BA = basaltic andesite, HMA = high-Mg andesite.

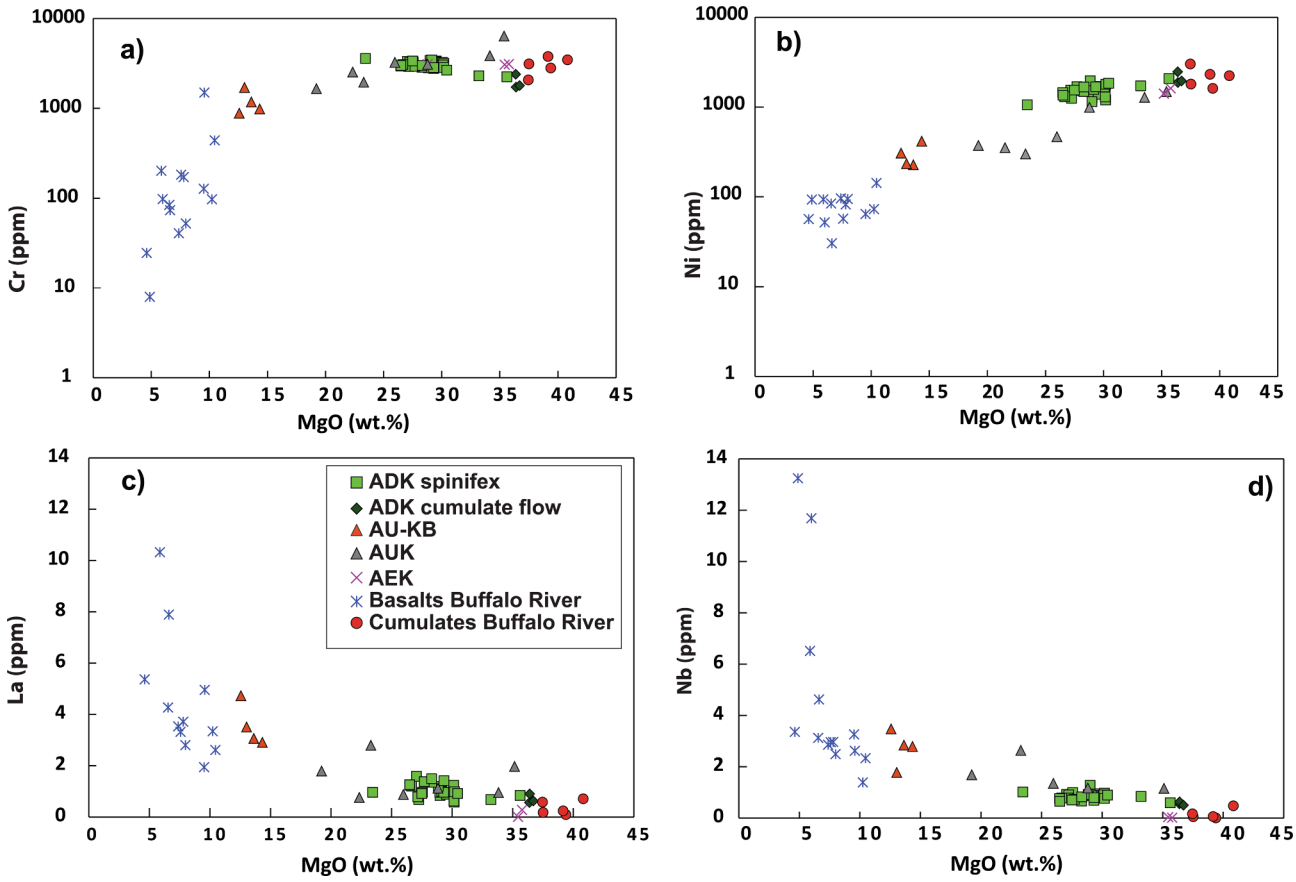



**Fig. 10.** Bivariate plots of Cr, Ni, La and Nb vs MgO for mafic and ultramafic rock types in the Buffalo River Greenstone Belt.

relative to the HREE. They can be further grouped into a high LREE/HREE type, with similar REE systematics to the Al-depleted komatiites, and a subtype that is characterised by flat REE patterns at generally lower abundances, more similar to the REE systematics of the Al-undepleted komatiites. In general, negative Ti anomalies occur in all mafic and ultramafic volcanic rocks analysed in this study (Fig. 11).

### 6.1.2. *Highly siderophile element (HSE) abundances*

The HSE concentrations of representative volcanic sample subsets from the Buffalo River Greenstone Belt are listed in Table 2. In general, the normalised HSE patterns differ between the volcanic suites identified. For the spinifex textured Al-depleted komatiites, the HSE concentrations are within the range of typical HSE abundances reported from other Al-depleted komatiite suites on the Kaapvaal craton, such as those from the Barberton and Schapenburg belts (Puchtel et al., 2009; Connolly et al., 2011). The variations in Pt and Pd abundances plotted against MgO (see Supplementary Figs. 2 and 3) show negative trends consistent with the more incompatible behaviour of these PPGEs during magmatic differentiation of ultramafic magmas. In a chondrite normalised diagram, the Al-depleted spinifex textured Buffalo River komatiite samples fall slightly below the Primitive Upper Mantle composition of Becker et al. (2006; Fig. 12a). The normalised patterns illustrate marked Re depletions, similar to the Schapenburg komatiites (Fig. 12e). Furthermore, for both these komatiite suites we note subtle depletions in Os and Ir relative to slightly less compatible Ru-Pt-Pd. The Al-undepleted komatiite and komatiitic basalt samples from the Buffalo River Greenstone Belt show subparallel chondrite normalised HSE patterns. These Al-undepleted komatiite samples have elevated Pt and Pd contents higher than the respective Primitive Upper Mantle values (Fig. 12.b). The Buffalo River komatiite cumulates show strongly variable HSE patterns characterised by IPGE (Os-Ir-Ru) depletion at elevated PPGE contents (Pt-Pd) (Fig. 12d), similar to the HSE patterns of cumulates from the Komati Formation (Fig. 12f), including notable Re depletions. The *meta*-basalts from the Buffalo River Greenstone Belt have significantly more fractionated HSE patterns compared to their komatiitic counterparts. The *meta*-basalts show strong IPGE depletions (Os-Ir-Ru) and PPGE enrichments (Pt-Pd) relative to primitive upper mantle values (Fig. 12c).

### 6.1.3. *Whole-rock Re-Os isotopic compositions*

The Re-Os isotope results for the Al-depleted komatiites and related rocks from the Buffalo River Greenstone Belt are listed in Table 2. The analysed Al-depleted spinifex textured komatiite samples have Re and Os concentrations between 0.003 and 0.025 ppb and 0.786–1.9 ppb, respectively, which corresponds to low $^{187}Re/^{188}Os$ (0.0090–0.1021; average = 0.0378 ± 0.0451). The Al-depleted komatiite samples have initial $^{187}Os/^{188}Os$ between 0.10477 and 0.15581, which corresponds to initial γOs values between + 1.55 and + 55 (at 3470 Ma). However, the majority of samples fall between + 1.55 and + 7.84 $\gamma Os_{(3470)}$. The Al-depleted komatiite samples with the highest measured $^{187}Os/^{188}Os$ have very low $^{187}Re/^{188}Os$, which suggests relatively recent Re loss, probably during alteration processes near the Earth's surface. The apparent Re mobility has eradicated any possibly existing 'isochronous' relationship between the various analysed Al-depleted komatiite units from the Buffalo River Greenstone Belt. The two analysed cumulate samples from Al-depleted komatiite lava flows reveal Re-Os elemental and isotopic compositions that are similar to those of the respective spinifex textured units (Table 2).

In contrast, the Al-undepleted komatiites and basaltic komatiites exhibit much higher initial $^{187}Os/^{188}Os$, with γOs values above + 427 (at 3470 Ma). Similarly, the basalts including pillowed varieties have very high $^{187}Re/^{188}Os$ (0.213–133) and initial $^{187}Os/^{188}Os$ (>1.3)

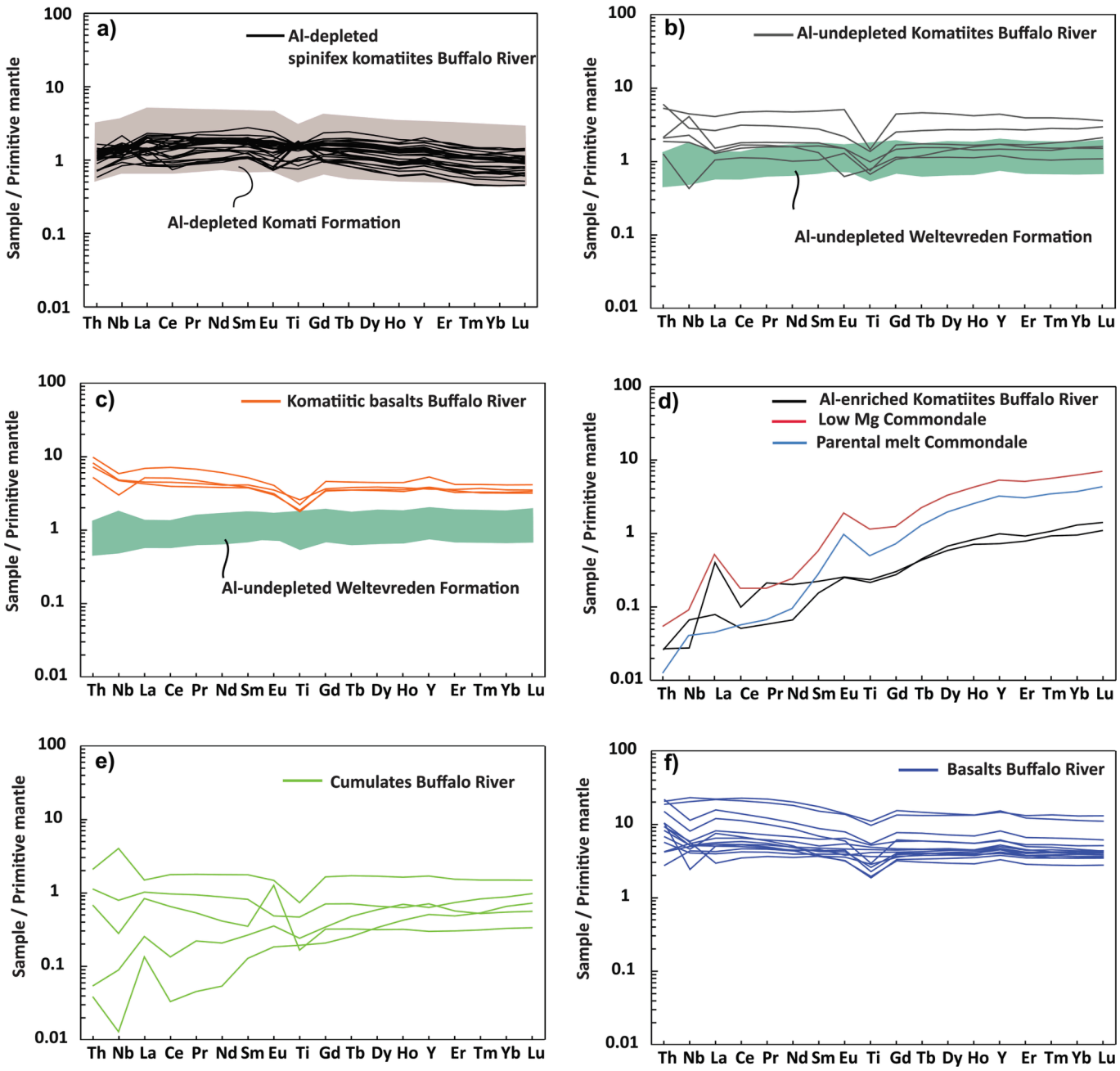



**Fig. 11.** Incompatible element abundance patterns for mafic and ultramafic rock types in the Buffalo River Greenstone Belt: a) Al-depleted komatiites from Buffalo River compared with Al-depleted komatiites from the Komati Formation of the Barberton Greenstone Belt (Robin-Popieul et al., 2012); b) Al-undepleted komatiites from Buffalo River compared with Al-undepleted komatiites from the Weltevreden Formation of the Barberton Greenstone Belt (Robin-Popieul et al., 2012); c) Al-undepleted komatiitic basalts from Buffalo River compared with Al-undepleted komatiitic basalts from the Weltevreden Formation of the Barberton Greenstone Belt (Robin-Popieul et al., 2012); d) Al-enriched komatiites from Buffalo River compared with Al-enriched komatiites from the Commondale Greenstone Belt (Wilson, 2019); e) ultramafic cumulates from Buffalo River; f) basalts from Buffalo River. All data normalised to the values for primitive mantle in Palme and O'Neill (2014).

compositions (0.037–1.437 ppb Re; 0.015–0.478 ppb Os). The associated cumulate samples (except for BR19-55) have Re and Os concentrations between 0.006 and 0.035 ppb and 0.55–2.93 ppb, respectively, which corresponds to low $^{187}Re/^{188}Os$ (0.015–0.254). Their initial $^{187}Os/^{188}Os$ compositions range between 0.104 and 0.184, which corresponds to initial γOs values between +0.8 and +78.8 (at 3470 Ma), similar to the Re-Os isotope systematics of the Al-depleted komatiites.

In general, it is noted that the Al-depleted spinifex textured komatiites from the Buffalo River Greenstone Belt have similar initial Os isotopic compositions to other Paleoarchean komatiites from the Kaapvaal craton, such as those from the Barberton (ca. 3484 Ma Komati Formation komatiites: 0 to + 0.7 γOs; Puchtel et al., 2014), Schapenburg (ca. 3550 Ma komatiites: +3.2 to + 16 γOs; Puchtel et al., 2016) and Commondale (ca. 3334 Ma komatiites: 0 to + 4.5 γOs; Wilson et al., 2003) belts (Fig. 13). The near-chondritic to supra-chondritic $^{187}Os/^{188}Os$ compositions of these Paleoarchean komatiite suites, including the Buffalo River occurrence studied here, provide a strong contrast to the predominantly sub-chondritic Os isotopic compositions that are characteristic for mantle peridotite xenolith suites from the Kaapvaal craton root (Pearson et al., 1995; Janney et al., 2010; van der Meer et al., 2017). An estimate of the HSE content of the mantle source to the Al-depleted Buffalo River komatiites, including comparisons to

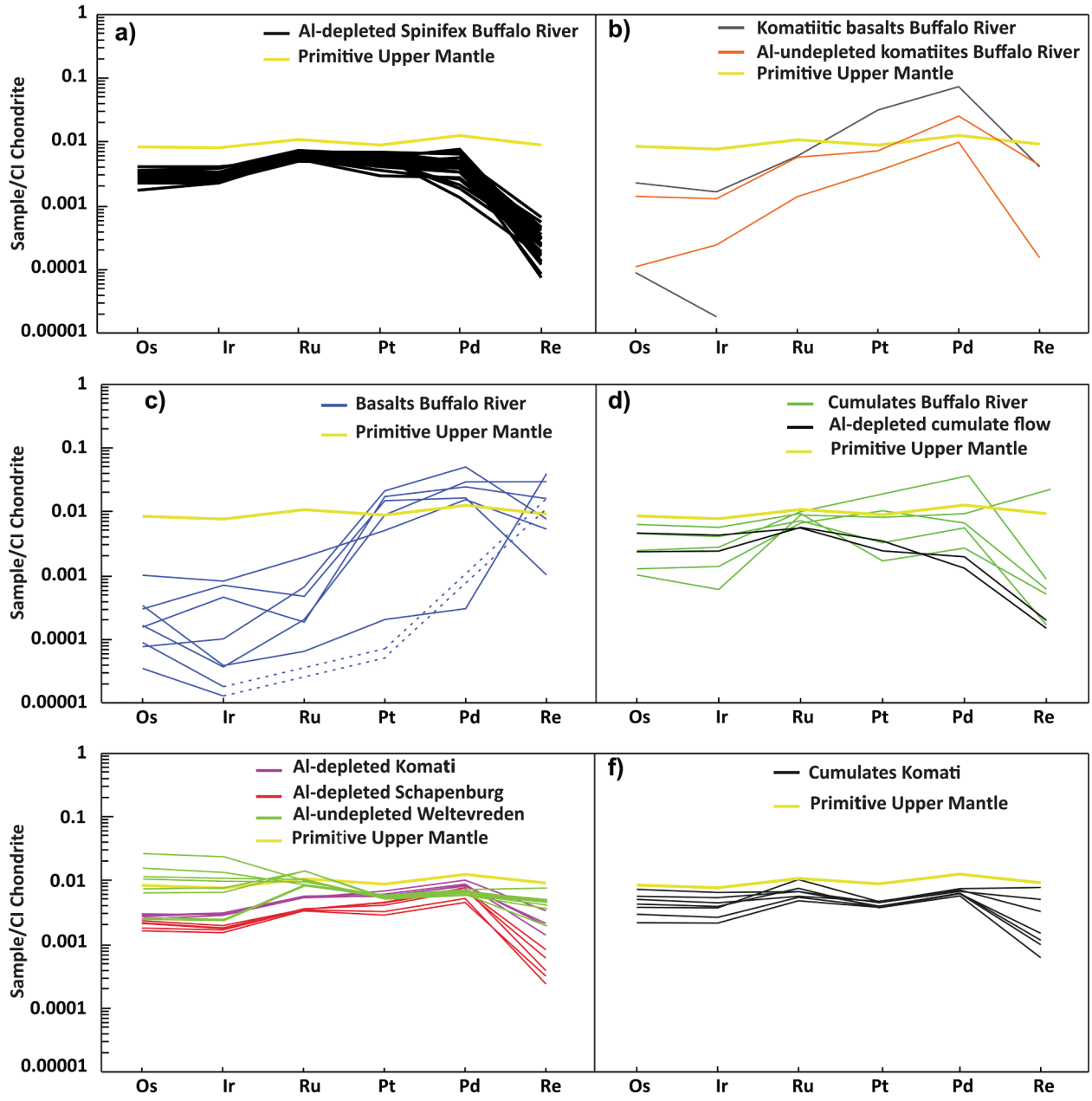



**Fig. 12.** Highly siderophile element abundance patterns for mafic and ultramafic rock types from the Buffalo River Greenstone Belt. All values normalised to the C1 carbonaceous chondrite of Horan et al. (2003). The yellow line in each panel represents the estimated composition of primitive mantle as per Becker et al. (2006). Data for komatiites from the Weltevreden and Komati Formations are from Puchtel et al (2009) and Puchtel et al (2014) respectively, while data for the Schapenburg komatiites are from Connolly et al. (2011).

other komatiite suites worldwide, is shown in Fig. 14 and discussed in Section 7.6.

### 6.2. *Felsic intrusive rocks (granitoids)*

#### 6.2.1. *Whole-rock major and trace element compositions*

Six samples from cross-cutting granitoids in the Sifula and Buffalo inliers of the Buffalo River Greenstone Belt were collected primarily for zircon U-Pb isotope ratio analysis to better constrain the minimum age of the mafic–ultramafic volcanic rock units. Table 3 lists the major and trace element data for these granitoids, which show $SiO_2$ ranges between 66 and 76 wt%. Using the geochemical classification of Barker (1979), our samples fall into the fields for trondhjemite, granodiorite and granite (Fig. 15a). We note that biotite is the predominant mafic phase of the granitoids studied. In a primitive mantle normalized multi-element diagram, the granitoid samples show LILE enrichments over the HREE, with relative depletions at Ta, Ti, P and Ba (Fig. 15b). When compared to the felsic intrusive rocks of the Barberton Greenstone Belt, there is a general overlap in LILE and HREE with no negative Eu observed. However, there is a contrast in that the Buffalo River samples are characterised by elevated concentrations of LREE when compared to those from Barberton.

#### 6.2.2. *U-Pb zircon geochronology*

Granite BR19-56 (Sifula inlier): the recovered prismatic zircon crystals range in size between ~ 150–250 μm and do not show any magmatic zoning or metamorphic overgrowths (Fig. 16). The Th and U contents range between 22 and 77 ppm and 749–1540 ppm, respectively, with low Th/U ratios of 0.02–0.05. In Wetherill U-Pb concordia space, 13 individually analysed zircon crystals define a mean

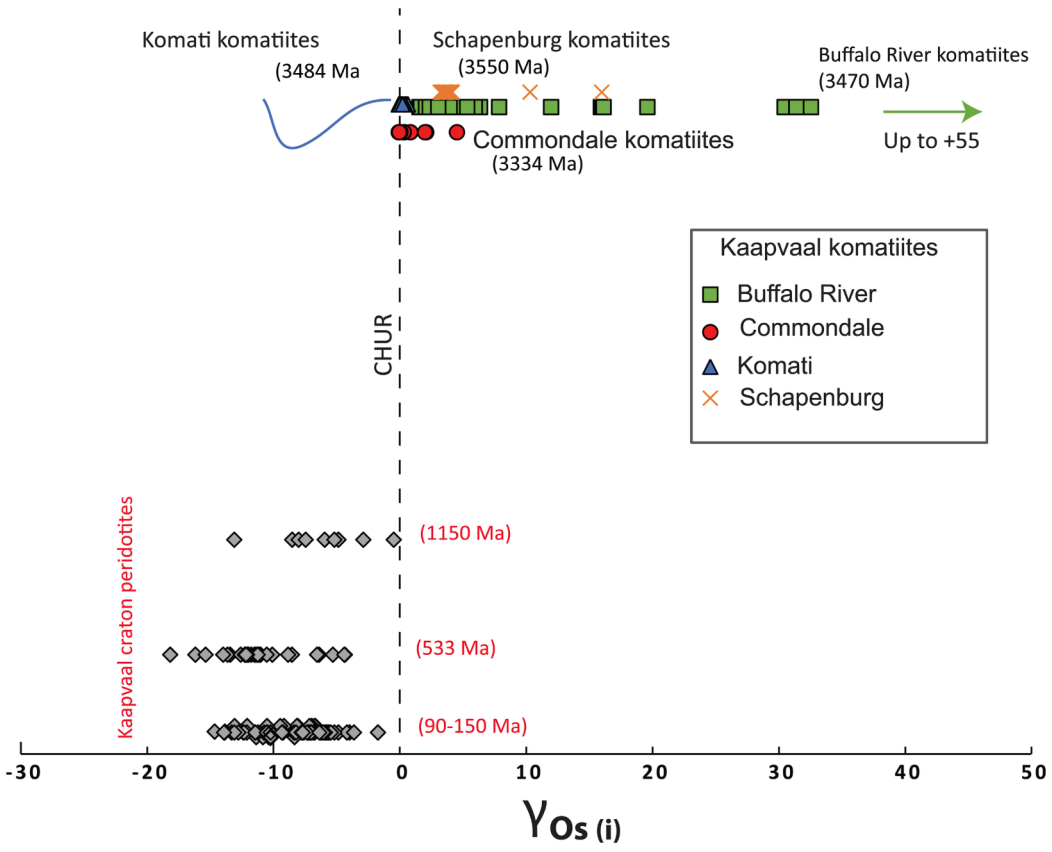



**Fig. 13.** Initial γOs compositions for the Buffalo River Al-depleted spinifex komatiites. Data for other komatiites on the Kaapvaal craton include Commondale (Wilson et al., 2003), Schapenburg (Puchtel et al., 2016), and Komati (Puchtel et al., 2014). Data for mantle-derived peridotite xenoliths in kimberlites on and around the Kaapvaal craton (grey diamonds) are taken from Pearson et al. (1995), Janney et al. (2010) and van der Meer et al. (2017), displayed at the respective times of kimberlite eruption.

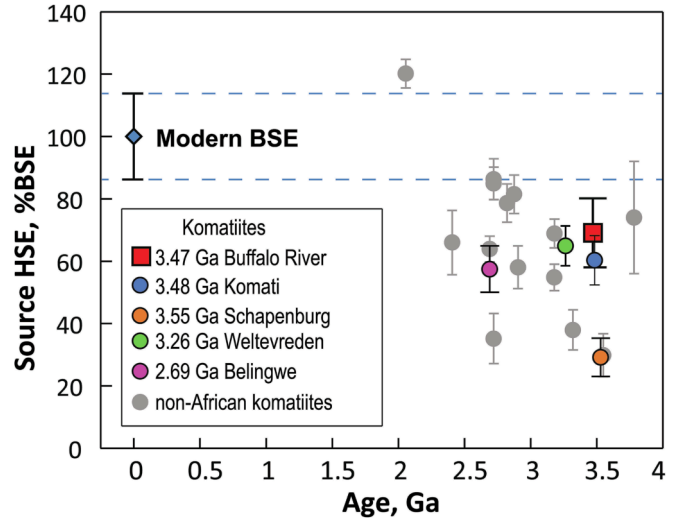



**Fig. 14.** Estimated total HSE abundances in the mantle sources of Archean and Proterozoic komatiites and related rocks, expressed as per cent relative to the total HSE content of the modern Bulk Silicate Earth (i.e., 100 %). The BSE estimate and its uncertainty are after Becker et al. (2006). The data for komatiites from cratons worldwide are taken from Puchtel et al. (2022), except for the ca. 3.8 Ga Saglek metakomatiites (Ishikawa et al., 2017). Our estimate for the total HSE abundance in the mantle source of the ca. 3.47 Ga Buffalo River komatiites is based on 27 samples of the Al-depleted variety (Table 2), for which we calculated a source Ru concentration of 4.84 ± 0.77 (1S.D.) ppb using the MgO-Ru correlation method of Ishikawa et al. (2017). This approach yields 69 ± 11 % total HSE abundance in the Buffalo River komatiite source relative to the modern BSE (7 ppb Ru).

$^{207}Pb/^{206}Pb$ upper intercept age of 3263.2 ± 2.4 Ma (2-sigma, MSWD = 38) (Fig. 17a).

Granite BR19-57 (Sifula inlier): the recovered prismatic zircon crystals range in size between ~ 150–250 μm and do not show any magmatic zoning or metamorphic overgrowths (Fig. 16). The Th and U contents range between 13 and 72 ppm and 527–2501 ppm, respectively, with low Th/U ratios of 0.02–0.06. In Wetherill U-Pb concordia space, 13 individually analysed zircon crystals define a mean $^{207}Pb/^{206}Pb$ upper intercept age of 3286.4 ± 4.0 Ma (2-sigma, MSWD = 17) (Fig. 17b).

Granite BR19-65 (Buffalo inlier): the recovered prismatic zircon crystals range in size between ~ 150–250 μm and do not show any magmatic zoning or metamorphic overgrowths (Fig. 16). The Th and U contents range between 60 and 132 ppm and 1600–2692 ppm, respectively, with low Th/U ratios of 0.03–0.06. In Wetherill U-Pb concordia space, 10 individually analysed zircon crystals define a mean $^{207}Pb/^{206}Pb$ upper intercept age of 3260.6 ± 8.0 Ma (2-sigma, MSWD = 7) (Fig. 17c). Granodiorite BR19-67B (Buffalo inlier): the recovered prismatic zircon crystals range in size between ~ 100–250 μm and do not show any magmatic zoning or metamorphic overgrowths (Fig. 16). The Th and U contents range between 15 and 81 ppm and 726–2174 ppm, respectively, with low Th/U ratios of 0.02–0.05. In Wetherill U-Pb concordia space, 11 individually analysed zircon crystals define a mean $^{207}Pb/^{206}Pb$ upper intercept age of 3469.2 ± 11.6 Ma (2-sigma, MSWD = 9) (Fig. 17d). The U-Pb zircon isotopic compositions are listed in Supplementary file Table S2.

## 7. Discussion

### 7.1. Age constraints for the Buffalo River komatiites and basalts

There are no direct radiometric age constraints for the greenstone assemblages of the Buffalo River belt, which is generally poorly studied

**Table 3**
Whole-rock analyses of the felsic intrusive rocks (granitoids) from the Buffalo River Greenstone Belt.

| Sample | BR19-56 | BR19-57 | BR19-64 | BR19-65 | BR19-67A | BR19-67B |
|---|---|---|---|---|---|---|
| **Major elements (wt.%)** | | | | | | |
| $SiO_2$ | 75.1 | 73.3 | 77.3 | 67.8 | 75.0 | 67.7 |
| $TiO_2$ | 0.140 | 0.200 | 0.120 | 0.610 | nd | 0.68 |
| $Al_2O_3$ | 13.7 | 13.8 | 12.6 | 13.1 | 13.3 | 13.8 |
| $Fe_2O_3$ | 1.14 | 1.65 | 1.13 | 4.82 | 0.844 | 5.20 |
| MnO | nd | nd | nd | 0.08 | nd | 0.10 |
| MgO | 0.340 | 0.813 | 0.498 | 1.90 | 0.084 | 1.62 |
| CaO | 0.717 | 0.721 | 1.88 | 2.46 | 0.581 | 3.31 |
| $Na_2O$ | 4.42 | 4.33 | 5.07 | 2.92 | 3.83 | 3.38 |
| $K_2O$ | 3.68 | 2.89 | 0.636 | 4.03 | 5.27 | 2.06 |
| $P_2O_5$ | nd | 0.058 | nd | 0.170 | nd | 0.202 |
| LOI | 0.790 | 2.0 | 1.12 | 1.15 | 0.430 | 1.21 |
| Total | 100 | 99.8 | 100 | 99.1 | 99.4 | 99.3 |
| **Trace elements (ppm)** | | | | | | |
| Li | 4.58 | 7.76 | 8.20 | 33.9 | 1.90 | 28.8 |
| P | 97.5 | 197 | 11.1 | 627 | 59.5 | 764 |
| Sc | 1.71 | 2.42 | 1.28 | 7.67 | 1.89 | 8.11 |
| Ti | 700 | 973 | 555 | 3122 | 197 | 3557 |
| V | 3.53 | 4.91 | 9.91 | 44.6 | 0.75 | 45.9 |
| Cr | 0.88 | 0.92 | 3.18 | 46.7 | 0.36 | 16.3 |
| Co | 1.28 | 1.69 | 2.92 | 11.2 | 0.83 | 12.4 |
| Ni | 1.47 | 1.00 | 4.91 | 22.12 | 1.06 | 17.0 |
| Cu | 6.57 | 1.37 | 25.6 | 22.8 | 32.4 | 41.2 |
| Zn | 26.8 | 41.6 | 14.1 | 66.7 | 15.7 | 80.6 |
| Ga | 14.9 | 17.0 | 12.0 | 21.0 | 14.5 | 19.1 |
| Rb | 97.8 | 107 | 23.8 | 110 | 128 | 151 |
| Sr | 129 | 110 | 78.2 | 193 | 50.2 | 249 |
| Y | 10.9 | 9.64 | 8.74 | 34.7 | 36.1 | 30.2 |
| Zr | 77.6 | 76.3 | 33.8 | 73.1 | 29.3 | 71.2 |
| Nb | 12.5 | 17.2 | 13.5 | 21.6 | 28.3 | 20.7 |
| Ba | 371 | 367 | 73.8 | 834 | 182 | 255 |
| Sn | 5.80 | 6.46 | 3.60 | 4.78 | 8.15 | 7.39 |
| Cs | 1.68 | 1.27 | 0.416 | 2.48 | 0.96 | 4.53 |
| La | 20.9 | 30.7 | 9.74 | 85.5 | 17.2 | 73.1 |
| Ce | 37.9 | 56.2 | 19.1 | 160 | 32.4 | 145 |
| Pr | 4.00 | 5.73 | 2.03 | 16.6 | 3.75 | 14.5 |
| Nd | 13.8 | 19.5 | 6.6 | 54.7 | 13.4 | 44.6 |
| Sm | 2.87 | 3.57 | 1.49 | 8.73 | 3.87 | 6.87 |
| Eu | 0,580 | 0,672 | 0,213 | 1,48 | 0,208 | 1,17 |
| Gd | 2.73 | 3.38 | 1.38 | 8.11 | 4.57 | 7.05 |
| Tb | 0,388 | 0,418 | 0,227 | 1,14 | 0,853 | 0,922 |
| Dy | 2.11 | 1.98 | 1.41 | 6.19 | 5.53 | 5.03 |
| Ho | 0,385 | 0,341 | 0,299 | 1.21 | 1.17 | 1.01 |
| Er | 1.07 | 0.886 | 0.928 | 3.37 | 3.43 | 3.00 |
| Tm | 0,159 | 0,131 | 0,170 | 0,482 | 0,575 | 0,463 |
| Yb | 1.00 | 0.821 | 1.27 | 2.87 | 3.67 | 2.98 |
| Lu | 0.135 | 0.113 | 0.189 | 0.387 | 0.504 | 0.431 |
| Ta | 1.92 | 1.95 | 2.00 | 1.23 | 4.73 | 1.85 |
| W | 0.560 | 0.233 | 0.974 | 0.331 | 0.235 | 0.337 |
| Pb | 18.9 | 21.8 | 12.3 | 18.9 | 49.5 | 20.1 |
| Th | 15.0 | 13.2 | 15.0 | 14.0 | 18.9 | 18.8 |
| U | 2.48 | 2.87 | 3.14 | 1.64 | 7.71 | 4.06 |

in comparison to other greenstone remnants on the Kaapvaal craton (e.g., Hofmann et al., 2019). Thus, the contact relationships with intrusive Archean granitoids provide an important 'indirect' constraint on the time frame of the ultramafic–mafic volcanism studied here. The Paleoarchean granitoids intrusive into the volcano-sedimentary assemblage of the Sifula Subgroup of the Buffalo River Greenstone Belt comprise an older tonalite-trondhjemite-granodiorite (TTG) suite at ca. 3.47 Ga and a more widespread younger granite suite that was emplaced in several magmatic pulses between 3.29 and 3.26 Ga (Fig. 17). Although it was apparent from the work of Dixon (2004) that the Sifula Subgroup must predate the ca. 3.29 Ga Mvunyana granodiorite or its local equivalents, our new U-Pb zircon data show that granodiorite units exposed in the Buffalo Gorge have a $^{207}Pb/^{206}Pb$ magma emplacement age of 3469.2 ± 11.6 Ma (Fig. 17). The dated, older granodiorite unit does not, however, expose an unequivocal intrusive contact with the surrounding greenstone units. Therefore, the available information permits two possible interpretations: (1) the older granodiorite unit represents part of a felsic basement to the greenstones, or (2) the ca. 3.47 Ga granodiorite is indeed intrusive into the greenstone sequence and, thus, provides a minimum age of the komatiitic to basaltic magmatism at the SE margin of the Kaapvaal craton. Regardless, our U-Pb zircon geochronological data for the diverse granitoid units within the Buffalo River Greenstone Belt identify the komatiitic and related volcanism as Paleoarchean in age with ultramafic–mafic magma eruptions before 3.26 Ga, or possibly even before 3.47 Ga. If the age of the komatiites and associated basalts is constrained by the age of the older granodiorite at 3.47 Ga, then these volcanic units can be interpreted as time-equivalents of the 3.55–3.48 Ga komatiite–basalt successions of the lower Onverwacht Group (e.g., Komati Formation and Schapenburg komatiites) in and near the Barberton Greenstone Belt (Puchtel et al., 2014, 2016; Schneider et al., 2019). This inference is supported by the geochemical similarity between the Al-depleted komatiites of the Barberton Greenstone Belt (i.e., Barberton-type komatiites) and those from the Buffalo River Greenstone Belt studied here, which includes overlapping HSE patterns and Os isotopic compositions (Fig. 12e and 13). However, we also identified subordinate Al-undepleted and Al-enriched komatiitic units that may represent ca. 3.33–3.26 Ga old time-equivalents of geochemically similar units in the Barberton (i.e., Weltevreden Formation) and Commondale greenstone belts of the Kaapvaal craton (Wilson et al., 2003; Connolly et al., 2011; Puchtel et al., 2014).

### 7.2. Alteration and element mobility

A limitation to the study of Archean volcanic rocks is the extent to which they have been subjected to alteration processes during and after magma emplacement. In order to investigate the effects of early-stage surface processes and later metamorphic overprint, it is important to assess how strongly the elemental and isotopic compositions of these rocks may have changed, and which geochemical signatures may still provide insights into their mantle sources. Hydration and silicification caused by hydrothermal seafloor alteration and low-grade regional metamorphism commonly affect the compositions of komatiites and related rocks in Archean greenstone belts (Lahaye et al., 1995; Chavagnac, 2004; Wilson, 2019; Bolhar et al., 2021). Our ultramafic–mafic volcanic rock samples from the Buffalo River Greenstone Belt are no exception and have been screened for alteration. Although the REE (excluding Ce and Eu) and the HFSE are generally considered to be immobile during alteration of komatiites, it is important to note that subtle element mobility has been observed in some komatiites from localities worldwide (e.g., Lahaye et al., 1995). The LILE such as Na, K, Cs, Rb, Ba and Sr have been proven to be highly mobile in komatiites and related rocks (Arndt, 2008), and these elements are not considered further. We note, however, that highly mobile Na shows only minor dispersion in the Al-undepleted komatiites, komatiitic basalts and tholeiites (Supplementary Fig. 4a).Certain other major and minor elements such as Al, Ti and Fe, as well as most HFSE (Th, Nb, Ta, Zr, Hf) and REE + Y, appear to be less affected by alteration and potentially record primary magmatic processes (Chavagnac, 2004; Lahaye et al., 1995). Positive correlations between these elements can be used to support their immobility during alteration (e.g., Ti vs Zr; Supplementary Fig. 4b).

The Buffalo River komatiites are characterized by greenschist facies mineral assemblages such as serpentine + tremolite-actinolite ± chlorite + magnetite, which indicate hydration reactions during hydrothermal alteration. No pronounced carbonate alteration is observed in thin sections except for some minor secondary carbonate associated with voluminous serpentine ± magnetite replacing olivine. The LOI values are also a good proxy for rock alteration, and the spinifex textured komatiites and pillowed basalts from the Buffalo River Greenstone Belt have 3–10 wt% and 0.8–3 wt% LOI, respectively. Arndt (2008) showed

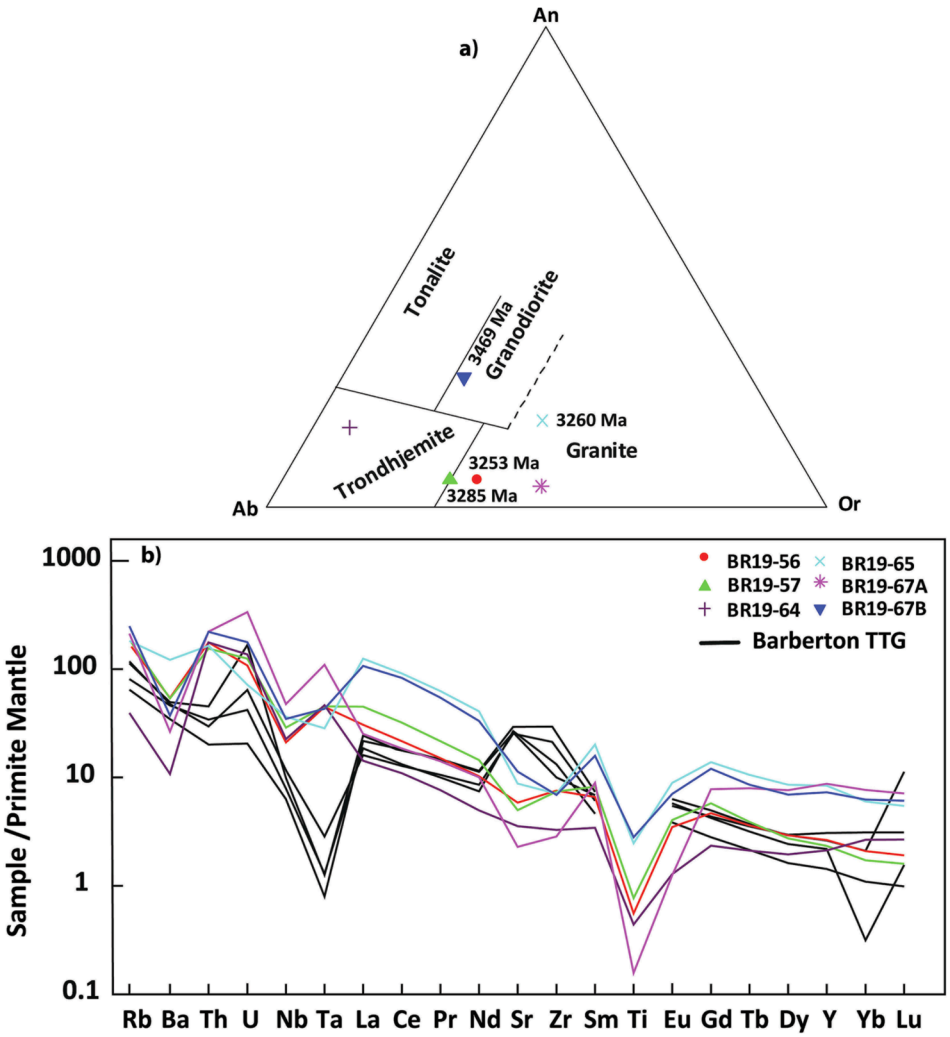



**Fig. 15.** a) Petrological classification of granitoid intrusives in the Buffalo River Greenstone Belt after Barker (1979); b) incompatible element abundance patterns of Buffalo River granitoids normalised to the primitive mantle values recommended by Palme and O'Neill (2014). Data for tonalite-trondhjemite-granodiorite rocks from Barberton are from Kleinhanns et al. (2003).

that MgO in Archean komatiites is relatively immobile as can be seen by the tight trends when plotted against other immobile major element oxides (e.g., $SiO_2$, $TiO_2$, $Al_2O_3$). The Co, Cr, Ni, La and Sc concentrations correlate well with MgO, which testifies to their immobility during alteration. Normalized REE patterns are well-defined without notable Ce and Eu anomalies. Apart from Re, the HSE contents of the komatiites and basalts studied do not exhibit scatter when plotted against MgO (Supplementary Figs. 2 and 3), which suggests that this group of immobile elements can also be used to evaluate the mantle sources of the ultramafic–mafic magmatism beneath the growing Kaapvaal craton during the Paleoarchean.

### *7.3. Nature of the Buffalo River komatiites and comparisons with other Kaapvaal komatiites*

The relatively well-preserved komatiite lava flows of the Buffalo River Greenstone Belt exhibit a cumulate zone at the bottom and a spinifex zone at the top (Fig. 4a-f). These textural-genetic characteristics are typical for komatiite lava flows from the Barberton Greenstone Belt on the Kaapvaal craton and for the classic Pyke Hill outcrop in the Abitibi Greenstone Belt on the Superior craton, where good exposures of a basal olivine cumulate layer (B unit) and an upper spinifex layer (A unit) are preserved (Pyke et al., 1973; Arndt and Nesbitt, 1982; Arndt, 2008). Within these lava flows, the spinifex textured layer is characterised by extremely high MgO contents of > 18 to 33 wt% (Figs. 8 and 10). Such extremely high Mg contents are also known from komatiite lava flows in the Barberton Greenstone Belt, with up to 37 wt % MgO in the spinifex zone of certain flow units (Viljoen and Viljoen, 1969; Jahn et al., 1982). A clear distinction is made based on petrographic differences between the samples (i.e., olivine spinifex textured komatiites, the phenocrystic actinolite schists and pillow basalts), where one can clearly distinguish between Mg-rich komatiites, komatiitic basalts and the Fe-rich tholeiitic basalts. The komatiites and komatiitic basalts from the Buffalo River Greenstone Belt have major element compositions that are typical for ultramafic–mafic volcanic rocks from Archean terranes worldwide (Barnes and Arndt, 2019). Most Archean volcanic rocks have been classified as boninites or "boninite-like" (e.g., the Barberton and Commondale komatiites; Pearce and Reagan, 2019). We use the discrimination diagrams of Pearce and Reagan (2019) to explore if the volcanic rocks from the Buffalo River Greenstone Belt meet the geochemical requirement of being classified as boninites (Fig. 9a-c). 'Identification' of the Al-depleted volcanic rocks as both boninites (Fig. 9a) and komatiites (Fig. 9b) raises a warning sign as to the applicability of these diagrams to the classification of Archean ultramafic rocks. We stress that the metavolcanic rocks investigated in this study should not be classified as boninites on geochemical grounds (Fig. 9a-d), which is also supported by the occurrence of spinifex textured lava flow units, a hallmark feature of komatiites and related high-MgO basaltic

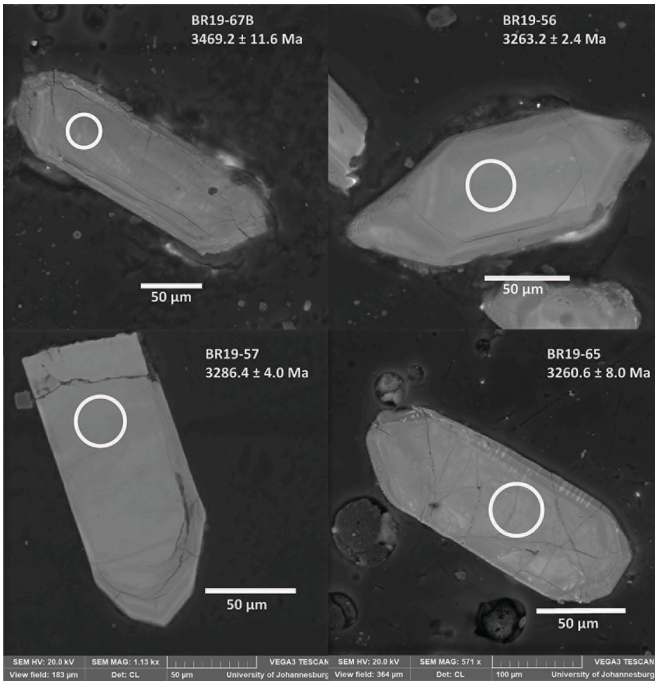



**Fig. 16.** Representative cathodoluminescence images of zircon crystals recovered from granitoids in the Buffalo River Greenstone Belt. The circles correspond to a 25 µm U-Pb LA-MC-ICP-MS analysis spot size.

rocks.

The Buffalo River komatiites are compared with the three globally recognized komatiite types that also occur on the eastern and southeastern portions of the Kaapvaal craton (i.e., Barberton and Commondale belts). The ultramafic–mafic volcanic rocks of the Buffalo River Greenstone Belt classify geochemically as Al-depleted, Al-undepleted and Al-enriched komatiites and related rocks including cumulates (Fig. 9e, f). In the case of bona fide komatiites (>18 wt% MgO and < 1 wt% $TiO_2$), recognition of the three main "alumina" types within a single volcanic succession suggests multi-stage petrogenetic processes, which may involve several distinct mantle sources or different melting conditions of a single mantle source (e.g., Sproule et al., 2002; Robin-Popieul et al., 2012). In our sample suite, the spinifex textured lava flows represent Al-depleted komatiites, with subchondritic $Al_2O_3/TiO_2$ ratios (5–12; Fig. 9f) and enrichment of the LREE over the HREE ($(La/Sm)_N$ = 0.58–1.34). These Al-depleted Buffalo River komatiites geochemically resemble archetypal komatiites from the Komati Formation in the Barberton Greenstone Belt (Figs. 11-12), which implies similar magma origins. The Al-depleted komatiites from the Komati Formation have been explained by > 30 % of high-pressure partial melting of an incompatible element depleted mantle source in the garnet/majorite stability field (Fig. 19a; Jahn et al., 1982; Cattell et al., 1984; Gruau et al., 1990; Xie et al., 1993; Arndt, 2003; Sossi et al., 2016). The presence of residual garnet/majorite accounts for the high $(Gd/Yb)_N$ ratios in these Al-depleted komatiites because this high-pressure Al-phase preferentially retains the HREE during mantle melting. The second geochemical type is represented by the actinolite schists, which are interpreted as metamorphosed Al-undepleted komatiites with chondritic $Al_2O_3/TiO_2$ (17–24) and flat REE patterns ($Gd/Yb_N$ = 0.9–1.1). The 'komatiitic' actinolite schists from the Buffalo River Greenstone Belt correspond geochemically to the Al-undepleted komatiites of the Weltevreden Formation in the Barberton Greenstone Belt (Fig. 11b). The geochemical character of Al-undepleted komatiites has been attributed to melt generation by very high degrees of partial melting at relatively shallow mantle depths without garnet involvement (Herzberg, 1992; Arndt, 2008; Robin-Popieul et al., 2012; Sossi et al., 2016). The flat REE patterns, low $(Gd/Yb)_N$ values and high $Al_2O_3/TiO_2$ compositions can be explained by re-melting of an upwelling mantle source that had previously produced Al-depleted komatiites at greater depths (i.e., a sequential melting model linked to the same rising mantle plume; Sossi et al., 2016) (Fig. 19b). The third geochemical type is represented by Al-enriched ultramafic rocks (some of which in the form of cumulates) that display suprachondritic $Al_2O_3/TiO_2$ ratios of > 25 (Fig. 9f). This type is characterised by significant LREE depletion at relative HREE enrichment (up to 2.39 $(La/Sm)_N$;Fig. 11d-e). The geochemical compositions of this Buffalo River komatiite type resemble those of the Al-enriched komatiites from the Commondale Greenstone Belt on the southeastern Kaapvaal craton (Fig. 1), but we note that flow structure preservation and rock type association differ between these occurrences (Wilson, 2019). Regarding the origin of such Al-enriched komatiites, their extremely depleted incompatible trace element contents at relatively high HREE concentration levels require a highly depleted mantle source that was poorer in incompatible elements than the modern depleted MORB mantle (Hoffmann and Wilson, 2017). Alumina-enriched komatiites were reported first from the Paleoarchean Commondale Greenstone Belt in South Africa (Wilson, 2003), and similar komatiite compositions have been reported recently from the Mesoarchean Rio das Velhas Greenstone Belt in Brazil (van Acken et al., 2016). We show that the Paleoarchean Buffalo River Greenstone Belt provides yet another occurrence of this seemingly rare type of komatiite. In order to account for the ultra-depleted trace element compositions of the Commondale komatiites, Wilson (2019) devised a two-stage model in which a primitive mantle source containing aluminous orthopyroxene and garnet partially melted at < 4 % and then the residue continued to melt to much higher degrees of up to 70 %. This model can yield Al-enriched ultramafic silicate melts with 36 wt% MgO, and melting of the refractory portion of an ascending mantle plume head at relatively shallow depths (<5 GPa) provides a reasonable scenario (Wilson, 2019). Although an involvement of, or interaction with, the refractory cratonic mantle lithosphere had also been considered in earlier models for the origin of Al-enriched komatiites (Wilson et al., 2003), the growing Re-Os isotope database for Archean komatiites and lithospheric mantle peridotite xenoliths from the Kaapvaal craton does not support this petrogenetic link (Fig. 13). For the Buffalo River Greenstone Belt, we suggest that the Al-enriched komatiite component formed by major melting of the refractory residue of the same ascending mantle plume that had previously produced the Al-depleted and Al-undepleted komatiites at greater depths (Fig. 19c). It remains unclear, however, as to why the Al-enriched komatiites are the volumetrically smallest component of the greenstone volcanic succession, and it is reasonable to speculate that the stratigraphically highest (latest) lava units were subjected to significantly more erosion shortly after emplacement.

The preserved volcanic succession of the Buffalo River Greenstone Belt is currently best explained by polybaric melting of a hot anhydrous mantle plume (see Jahn et al., 1982; Herzberg, 1992; Arndt et al., 1998; Robin-Popieul et al., 2012; Sossi et al., 2016). Although such dynamic mantle melting models have been proposed previously to explain komatiite-bearing volcanic successions in the Barberton and Abitibi greenstone belts through time (Sproule et al., 2002; Robin-Popieul et al., 2012), our model suggests that products of polybaric mantle plume melting may constitute single komatiitic to basaltic volcanic successions (see also Sossi et al., 2016). In other words, the model of Robin-Popieul et al. (2012) for the mantle source evolution and melt extraction history of the various komatiite types from the Barberton Greenstone Belt is able to account for the co-existence of the three major types of komatiites present in the Buffalo River Greenstone Belt.

### *7.4. Role of fractional crystallization in the genesis of komatiitic basalts and tholeiites*

The origin of komatiitic basalts within greenstone belts and their genetic relationship, if any, to bona fide komatiites and basalts remains

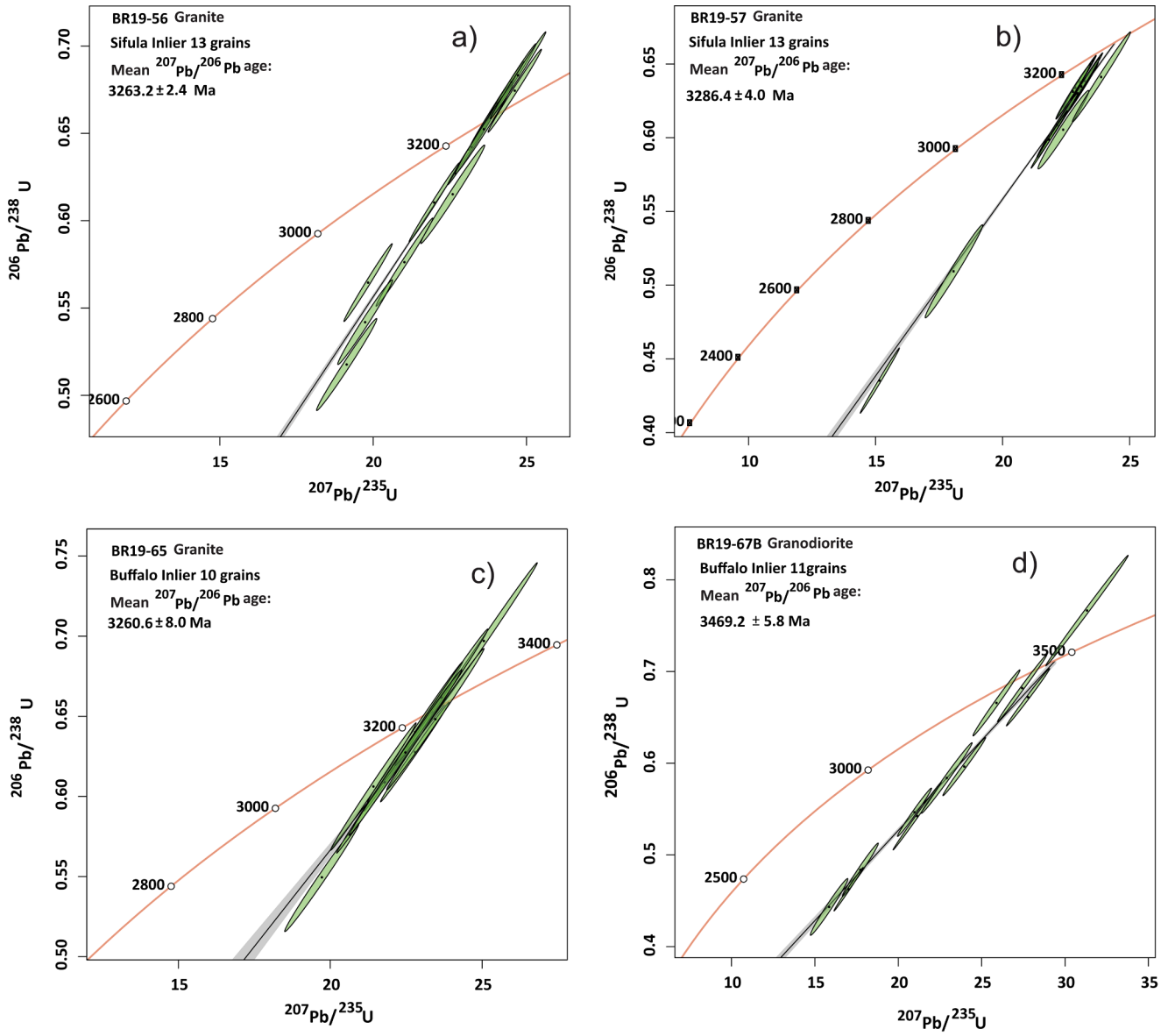



**Fig. 17.** U-Pb (Wetherill) concordia diagrams for zircons recovered from the granitoids of the Buffalo River Greenstone Belt. Data ellipses correspond to 1-sigma analytical uncertainties. Age calculations and data display were conducted using IsoplotR (Vermeesch, 2018).

controversial. It has been shown that komatiitic basalts can either be produced as primary mantle melts or by fractional crystallisation from primary komatiite magma (Arndt, 2008). More recent models demonstrate that AFC processes (assimilation and fractional crystallisation) played an important role in the production of komatiitic basalts and tholeiitic basalts in some greenstone volcanic successions in India and Canada (e.g., Ghosh et al., 2019; Waterton et al., 2020).

The komatiitic basalts of the Buffalo River Greenstone Belt can be linked to the komatiites on the basis of their field relationships and common textural features. The komatiitic basalts are characterised by actinolite phenocrysts set in a tremolite matrix, which is similar to the komatiites from the central inlier that do not show spinifex textures. In geochemical variation diagrams, trends from the komatiites to the lower-MgO komatiitic basalts are noted (Fig. 8a-b, 10). The major and trace element variations show that the tholeiitic and komatiitic basalts fall on a continuous data array that originates at the komatiite compositions. These trends are best explained by a fractional crystallisation relationship, with bona fide komatiite magmas as the parent and komatiitic basalts through to tholeiitic basalts as derivatives. More specifically, the positively correlated trends between Cr-MgO and Ni-MgO observed for the Al-undepleted komatiites can be attributed to fractional crystallization of Cr-spinel and olivine. A role for orthopyroxene as a fractionating liquidus phase is difficult to establish because of the scattered $Al_2O_3$ contents ranging between 1.32 and 4 wt% in the komatiites and between 6 and 12 wt% in the komatiitic basalts. Importantly, we find that the komatiitic basalts and basalts possibly evolved from the Al-undepleted komatiite liquid by olivine and Cr-spinel fractionation, which may also explain the relative scarcity of this parental magma type. The trace element compositions of the komatiitic basalts and basalts from the Buffalo River Greenstone Belt provide evidence for concomitant crustal contamination during fractional crystallisation (i.e., AFC-type processes). To quantify the extent of AFC-type processes by which the komatiitic and tholeiitic basalts evolved from the Al-undepleted komatiite parent magma, detailed energy-constrained geochemical modelling is required (Spera and Bohrson, 2001), which is beyond the scope of this study.

### 7.5. Contamination by felsic continental crust

All preserved Archean greenstone belts are in relatively close contact

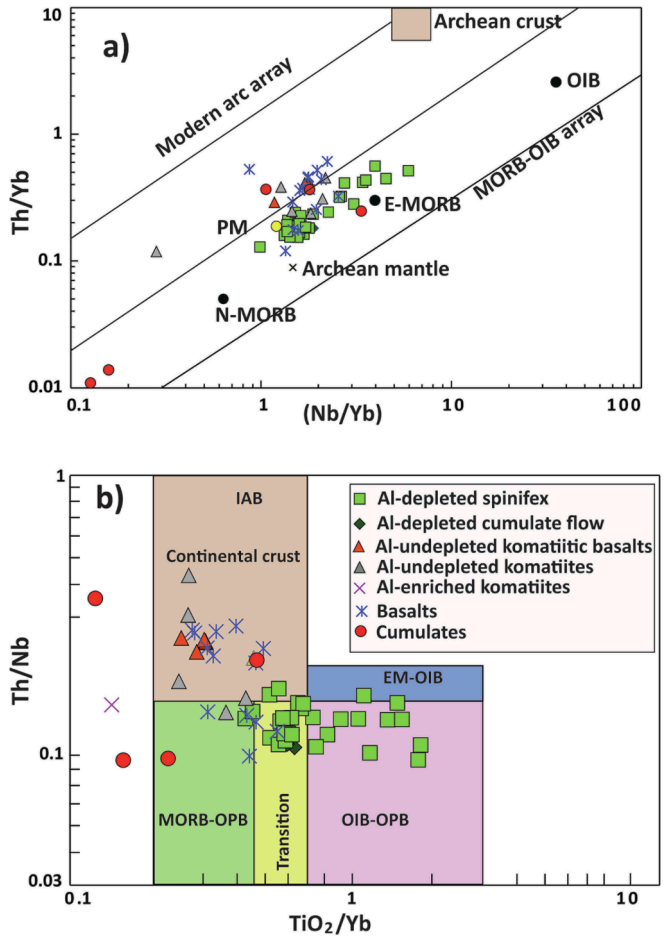



**Fig. 18.** a) Th/Yb vs Nb/Yb and (b) Th/Nb vs $TiO_2$/Yb plots for mafic and ultramafic rock types from the Buffalo River Greenstone Belt, after Pearce (2008) and Pearce et al. (2021) respectively. Reference values are from Sun and McDonough (1989; modern mantle reservoirs), Smithies et al. (2018; Archean crust) and Schneider et al. (2019; Archean mantle). Oceanic plateau basalts = OPB, ocean island basalts = OIB, mid-ocean ridge basalts = MORB, EM = enriched mantle.

with pre-existing felsic continental crust (Bickle et al., 1994; Kröner et al., 2013; Campbell and Davies, 2016). However, there is uncertainty about whether Archean ultramafic–mafic magmas erupted in an oceanic environment and were subsequently emplaced onto continental crust by tectonic events (de Wit, 2004; Bolhar et al., 2021). In order to assess the origin and evolution of Archean ultramafic–mafic volcanic rock successions it is important to identify possible contamination by materials from the early felsic continental crust (Schneider et al., 2019).

For the komatiitic and basaltic rocks of the Buffalo River Greenstone Belt we test the effects of crustal contamination by exploring their immobile trace element ratios. Fig. 18a shows that the komatiites, komatiitic basalts and basalts have geochemical characteristics typical for primitive, mantle-derived magmas without significant contamination by felsic continental crust materials (Fig. 18a). In the Th/Yb versus Nb/Yb diagram, the ultramafic–mafic volcanic rocks lie parallel to and above the mantle array, at Th/Yb ratios between 0.1 and 0.5 (Fig. 18a). There is wide scatter among the basalts, which partly overlap with the komatiitic basalts at high Th/Yb and low Nb/Yb – very different from the komatiites. To further test the effects of crustal contamination on the komatiite data set, we use the Nb/Nb* ratio ($Nb/Nb^* = Nb_N/\sqrt{(Th^*La)_N}$). For komatiitic magma, involvement of felsic crustal material during emplacement will result in Nb/Nb* ratios < 1 (Jochum et al., 1991), and several of our samples show such crustal fingerprints. Variation within the Al-depleted komatiite samples is noted in their Nb/Nb* ratios, where samples with a slight Nb anomaly in normalized patterns have ratios below unity (0.7 to 0.98). The samples without Nb anomaly have Nb/Nb* between 1 and 1.7. Two Al-undepleted komatiite samples have Nb/Nb* >1, and the remainder of the samples fall between 0.37 and 0.95. Al-undepleted komatiitic basalts have Nb/Nb* between 0.6 and 0.85. The Al-enriched komatiites and their cumulates have Nb/Nb* between 0.2 and 1.47 and between 0.18 and 0.76, respectively.

In the discrimination diagram using Th/Nb vs $TiO_2$/Yb (Fig. 18b), the Buffalo River Greenstone Belt samples fall within several fields for different tectonic settings. The Al-depleted spinifex textured komatiites and their cumulates fall within the MORB-OPB and OIB-OPB fields (OPB = oceanic plateau basalts). The Al-undepleted komatiites and komatiitic basalts as well as Al-enriched komatiite cumulates overlap the field for the continental crust. Due to the extremely low $TiO_2$ contents, the Al-enriched komatiites fall outside of the 'tectonic settings' demarcation in Fig. 18b. Fig. 18b also shows wide variation for the basaltic samples, with the majority falling within the field of continental crust.

Although the incompatible trace element signatures of the majority of the Al-depleted komatiites reflect mantle source features, several of our Al-undepleted and Al-enriched komatiite samples as well as a few basaltic samples show contamination by felsic continental crust materials. A recent study by Grosch and Slama (2021) reported initial εHf values for the 3.48 Ga ultramafic and mafic volcanic rocks from the Barberton Greenstone Belt. The negative εHf values of their komatiite samples (−3.1 to −1.9) are best explained by crustal contamination of the magma with felsic or even mafic materials as known from the nearby ca. 3.6 Ga Ancient Gneiss Complex (Grosch and Slama, 2021). In a similar manner, we interpret the crustal signatures observed in many of the volcanic samples from the ca. 3.47 Ga Buffalo River Greenstone Belt (Fig. 18b) to indicate interactions between the ultramafic–mafic magmas and mainly felsic basement components of the Ancient Gneiss Complex.

### *7.6. Petrogenetic constraints from $^{187}Os/^{188}Os$ and siderophile element systematics*

Komatiite melts extract relatively large amounts of HSE from their mantle source regions, which renders these high-Mg, sulphur undersaturated volcanic rocks a good proxy for the compositional variation of Earth's mantle (Puchtel et al., 2007; Fiorentini et al., 2011; Waterton et al., 2021). The HSE are characterised by high partition coefficients between sulphides and mantle-derived silicate melts, with Pt and Pd being less compatible than Os-Ir-Ru (Mungall and Brenan, 2014). The HSE can be used to infer whether mantle-derived mafic and ultramafic magmas had equilibrated with sulphides in their source (Maier et al., 2003). The Re-Os isotopic compositions of mantle-derived melts from localities worldwide have been used to suggest that the convecting upper mantle had evolved with Re/Os ratios similar to those of chondritic meteorites (Snow and Reisberg, 1995; Harvey et al., 2006; Liu et al., 2009). Considering that the Al-depleted komatiites from the Buffalo River Greenstone Belt have initial $^{187}Os/^{188}Os$ near the chondritic value and slightly above (Fig. 13), it is reasonable to infer that the upwelling plume material that sourced these komatiites from > 400 km depth had a primitive mantle composition. Subsequent to multi-stage komatiitic melt extraction from the rising plume head, the depleted and buoyant peridotitic residues were 'subcreted' onto the growing Kaapvaal lithospheric root (e.g., Aulbach, 2012), where most of this material evolved at relatively low Re/Os (e.g., Pearson and Wittig, 2014), as is evident from the exclusively negative γOs values of cratonic mantle peridotite xenoliths from southern Africa (Fig. 13). The observed behaviour of Os in the volcanic samples of the Buffalo River Greenstone Belt is in agreement with the high compatibility of this element during mantle melting, whereas Pt and Pd are slightly more incompatible (Barnes et al., 1985; Rehkämper et al., 1999), which can be observed in the slightly higher chondrite-normalized concentrations (Fig. 12). The normalized HSE patterns of the Al-depleted Buffalo River komatiites

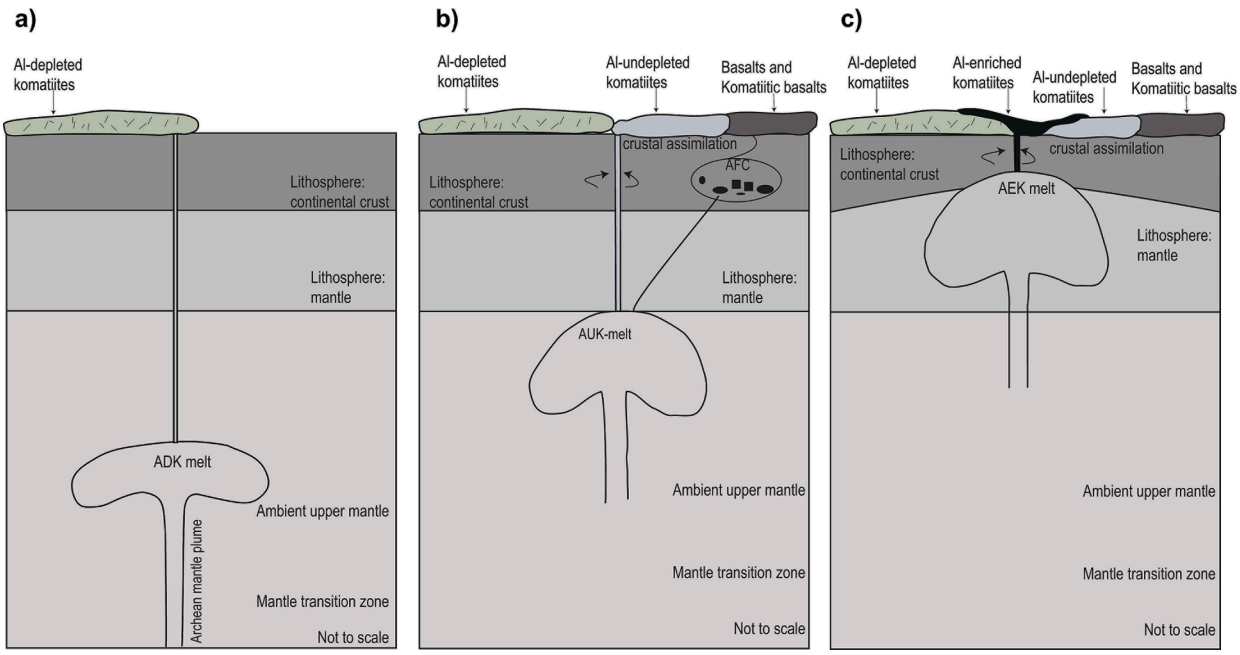



**Fig. 19.** A schematic geodynamic model for the formation of the various komatiites, komatiitic basalts and basalts of the Buffalo River Greenstone Belt from stages 1 to 3. a) initial stages of the Archean plume which first formed the Al-depleted komatiite melts at greater depths; b) further decompression melting of the previously depleted plume formed the AUK komatiites. Komatiitic and tholeiitic basalts formed by assimilation and/or partial melting of an AUK source; c) the final melting stage where the formation of AEK melts occurs at shallow depths from the same plume source as that shown in (a) and (b). ADK = Al-depleted komatiites, AUK = Al-undepleted komatiites, AEK = Al-enriched komatiites, AFC = Assimilation-fractional crystallisation.

overlap with those of the Paleoarchean Schapenburg and Komati Formation komatiites farther north on the Kaapvaal craton (Fig. 12e) (Puchtel et al., 2009, 2014, 2016), which implies a similar petrogenesis.

It has been speculated that during Early Earth mantle evolution an increase in the abundances of HSE, as apparent from the analysis of komatiites through time, was caused by progressive downward mixing of the meteoritic 'late veneer' after 3.8 Ga (Maier et al., 2009). However, other komatiite studies challenged this model and argued that the HSE systematics do not define concentration trends through time (Puchtel et al., 2014, 2016; Waterton et al., 2021). Regardless, it has been noticed in several independent studies that some of the lowest Pt-Pd concentrations of komatiites occur in Paleoarchean occurrences formed at ca. 3.5 Ga (Puchtel et al., 2009; Maier et al., 2009; Fiorentini et al., 2011), and this may indeed reflect the presence of HSE poor mantle domains during the Early Archean. Most recently, Waterton et al. (2021) stressed that the variable Pt-Pd contents of komatiites from localities worldwide may be a function of changes in the intensive variables during high-degree mantle melting, such as the pressure of melt extraction and the $fO_2$ conditions in the source.

The HSE patterns of the Al-depleted komatiites from the Buffalo River Greenstone Belt are slightly fractionated relative to the primitive upper mantle estimate of Becker et al. (2006), at marginally lower HSE abundance levels, with Pd/Ir ranging between 0.9 and 2. According to Puchtel et al. (2009), komatiites with such HSE systematics were probably derived from sources with low PGE contents that may represent ca. 3.5 Ga old deep-seated convecting mantle domains. By this time, these deep mantle domains had not received the full HSE complement from the meteoritic 'late veneer' (Maier et al., 2009). Indeed, our estimate of the HSE content of the mantle source to the Al-depleted komatiites suggests that only 69 ± 11 % HSE were present relative to the modern mantle HSE inventory proxied by the Bulk Silicate Earth value set at 100 % (Fig. 14). Our HSE estimate at ca. 3.47 Ga, using the approach of Ishikawa et al. (2017), is similar to the mantle source HSE constraint from the Al-depleted komatiites of the ca. 3.48 Ga Komati Formation (60 ± 8 %; Puchtel et al., 2022), which once again points to a similar petrogenesis for these particular Paleoarchean komatiites from the Kaapvaal craton (Fig. 14).

The Al-undepleted komatiites from the Buffalo River Greenstone Belt exhibit HSE patterns that are different from those of the Al-depleted komatiites, which suggests different mantle sources. They have similar IPGE abundances and distributions compared to the Al-undepleted komatiites of the Weltevreden Formation (Connolly et al., 2011), but their Pt and Pd concentrations (PPGE) are extremely enriched, partly exceeding primitive upper mantle values. According to Waterton et al. (2021), such PPGE enrichment may record melt extraction at lower pressures, which is consistent with other geochemical parameters (e.g., REE patterns) that suggest melt generation by very high degrees of partial melting at relatively shallow mantle depths, with only little or no garnet involvement (see Section 7.3). Given the complexity of these HSE patterns, we did not attempt a mantle source HSE estimate for the Al-undepleted komatiites.

The basaltic samples from the Buffalo River Greenstone Belt show strong fractionation between the IPGE and PPGE (e.g., extremely high Pd/Ir; Fig. 12c), which supports our earlier notion that these lavas formed mainly by differentiation from the Al-undepleted komatiites in the volcanic succession. Magmatic differentiation may have further accentuated the IPGE/PPGE fractionation and, thus, caution must be exercised in the interpretation of the HSE systematics of the *meta*-basalts studied here. For example, the marked Ru depletion observed in some basaltic samples (Fig. 12c) may be caused by chromite fractionation, because Ru is more compatible in chromite compared to the other IPGEs at ambient mantle redox conditions (Brenan et al., 2012). Hence, this HSE geochemical signature cannot be interpreted in terms of source-forming processes.

## 8. Conclusions

- The Paleoarchean Buffalo River Greenstone Belt at the southeastern Kaapvaal craton margin has a minimum age of 3469 ± 12 Ma based on zircon U-Pb isotope data for a granodiorite sheet that is interpreted as intrusive into the *meta*-volcanic succession. The relatively small greenstone remnant hosts three geochemically discrete

komatiite types (Al-depleted, Al-undepleted, Al-enriched) and abundant associated basalts.

- The origins of the three identified Buffalo River komatiite types may be linked to deep critical melting of a single large mantle plume that may have been associated with the formation and growth of the Kaapvaal continent at around 3.5 Ga. Each komatiite melt type escaped from the upwelling mantle source at different pressure but similarly hot temperature conditions.
- The Buffalo River Al-depleted komatiites are most common within the spinifex zone of lava flows and compositionally resemble the ca. 3.48 Ga komatiites from the Komati River type locality in the Barberton Greenstone Belt. Their petrogenesis requires the highest pressures within the stability field of majoritic garnet at $>$ 300–400 km depth.
- Continued decompression melting of the same mantle plume head formed the Al-undepleted komatiites of the Buffalo River Greenstone Belt, which are geochemically similar to the ca. 3.26 Ga komatiites of the Weltevreden Formation in the Barberton Greenstone Belt.
- The Buffalo River Al-enriched komatiites formed at the shallowest depth level directly beneath the growing Kaapvaal craton root, and their petrogenesis is comparable to that of the ultra-depleted ca. 3.33 Ga silica-rich komatiites from the Commondale Greenstone Belt some 100 km farther north.
- The geochemical signatures of the volcanic rocks from the Buffalo River Greenstone Belt suggest interactions between the mantle-derived magmas and older felsic crust, probably associated with an unexposed equivalent of the ca. 3.6 Ga Ancient Gneiss Complex.
- Basalts of komatiitic and tholeiitic affinity are interpreted as fractionation products derived from parental magmas that were similar in composition to the Al-undepleted komatiites.
- The highly siderophile element systematics of the Al-depleted komatiites from Buffalo River suggest an origin from a deep-seated PGE poor mantle source that had not received the full complement of the meteoritic late veneer by ca. 3.5 Ga (only 69 $\pm$ 11 % of the modern mantle HSE budget). For the Al-undepleted komatiites, it appears likely that high Pt and Pd contents are a function of shallower melt extraction rather than records of PGE rich mantle sources.

## CRediT authorship contribution statement

**Thendo Netshidzivhe:** Investigation, Data curation, Writing - original draft. **Sebastian Tappe:** Investigation, Funding acquisition, Supervision, Data curation, Writing - original draft, Manuscript writing and editing, Computational analysis. **Allan H. Wilson:** Data collection, Manuscript editing. **Akira Ishikawa:** Data collection, Manuscript editing, Computational analysis. **Fanus Viljoen:** Manuscript editing, Funding acquisition, Supervision.

## Declaration of Competing Interest

The authors declare that they have no known competing financial interests or personal relationships that could have appeared to influence the work reported in this paper.

## Data availability

All data have been made available and are included.

## Acknowledgements

This manuscript forms part of the PhD thesis of TN, who was supported by a National Research Foundation South Africa (NRF) studentship. ST acknowledges support from the NRF through the IPRR grant program and the CIMERA Centre of Excellence (#1976). A large portion of the analytical costs for this project were covered from DSI-NRF SARChI funds (#64779), awarded to FV. We gratefully acknowledge support by the following colleagues during the course of this study: Christophe Ballouard (field work support), Henriette Ueckermann (LA-ICP-MS support), Christian Reinke (XRF support), and the late Roger Dixon for help with the SELFRAG instrumentation. Special thanks go to Axel Hofmann who made ST aware of the underexplored komatiites in the Buffalo River area. Igor Puchtel is sincerely thanked for providing his published data for South African komatiites in easy-to-access table format and for his helpful journal review. We also thank an anonymous reviewer and the editor Martin Whitehouse for constructive feedback on our work.

## Appendix A. Supplementary data

Supplementary data to this article can be found online at https://doi.org/10.1016/j.precamres.2023.107071.

## References

Akizawa, N., Yamaguchi, A., Tani, K., Ishikawa, A., Fujita, R., Choi, S.H., 2021. Highly refractory dunite formation at Gibbs Island and Bruce Bank, and its role in the evolution of the circum-Antarctic continent. Can. Mineral. 59 (6), 1731–1753.

Allegre, C., 1982. Genesis of Archean komatiites in a wet ultramafic subducted plate. In: Arndt, N.T., Nisbet, E.G. (Eds.), Komatiites. George Allen and Unwin, London, England, pp. 495–500.

Anhaeusser, C.R., 2014. Archaean greenstone belts and associated granitic rocks - A review. J. Afr. Earth Sc. 100, 684–732.

Arndt, N.T., 2003. Komatiites, kimberlites, and boninites. J. Geophys. Res. 108 (B6), 2293.

Arndt, N.T., 2008. Komatiite. Cambridge University Press, p. 467.

Arndt, N., Ginibre, C., Chauvel, C., Albare'de, F., Cheadle, M., Herzberg, C., Jenner, G., Lahaye, Y., 1998. Were komatiites wet? Geology 26, 739–742.

Arndt, N.T., Nesbitt, R.W., 1982. Geochemistry of Munro township basalts. In: Arndt, N. T., Nisbet, E. (Eds.), Komatiites. George Allen and Unwin, London, pp. 309–329.

Asafov, E.V., Sobolev, A.V., Gurenko, A.A., Arndt, N.T., Batanova, V.G., Portnyagin, M. V., Garbe-Schönberg, D., Krasheninnikov, S.P., 2018. Belingwe komatiites (2.7 Ga) originate from a plume with moderate water content, as inferred from inclusions in olivine. Chem. Geol. 478, 39–59.

Aulbach, S., 2012. Craton nucleation and formation of thick lithospheric roots. Lithos 149, 16–30.

Barker, F., 1979. Trondhjemite: definition, environment and hypotheses of origin. In: Developments in petrology, Vol. 6. Elsevier, pp. 1–12.

Barnes, S.J., Arndt, N., 2019. Distribution and geochemistry of komatiites and basalts through the Archean. In: Van Kranendonk, M., Bennett, V., Hoffmann, E. (Eds.), Earth's Oldest Rocks. Elsevier.

Barnes, S.J., Naldrett, A.J., Gorton, M.P., 1985. The origin of the fractionation of platinum-group elements in terrestrial magmas. Chemical geology 53 (3–4), 303–323.

Becker, H., Horan, M.F., Walker, R.J., Gao, S., Lorand, J.-P., Rudnick, R.L., 2006. Highly siderophile element composition of the Earth's primitive upper mantle: constraints from new data on peridotite massifs and xenoliths. Geochim. Cosmochim. Acta 70 (17), 4528–4550.

Bickle, M.J., 1982. The magnesium contents of komatiitic liquids. In: Arndt, N.T., Nisbet, E.G. (Eds.), Komatiites. George Allen and Unwin, London, pp. 479–494.

Bickle, M.J., Nisbet, E.G., Martin, A., 1994. Archean greenstone belts are not oceanic crust. J. Geol. 102 (2), 121–137.

Black, L.P., Kamo, S.L., Williams, I.S., Mundil, R., Davis, D.W., Korsch, R.J., Foudoulis, C., 2003. The application of SHRIMP to Phanerozoic geochronology; a critical appraisal of four zircon standards. Chem. Geol. 200 (1–2), 171–188.

Bolhar, R., Tappe, S., Wilson, A.H., Ireland, T., Avila, J., Anhaeusser, C.R., 2021. A petrochronology window into near-surface fluid/rock interaction within Archaean ultramafic-mafic crust: Insights from the 3.25 Ga Stolzburg Complex, Barberton Greenstone Belt. Chem. Geol. 569, 120130.

Brandl, G., Cloete, M., & Anhaeusser, C.R. (2006). Archaean greenstone belts. In: Johnson, M.R., Anhaeusser, C.R., Thomas, R.J. (Eds.), The Geology of South Africa, Johannesburg and Pretoria (Geological Society of South Africa, and Council for Geosciences), 9–56.

Brenan, J.M., Finnigan, C.F., McDonough, W.F., Homolova, V., 2012. Experimental constraints on the partitioning of Ru, Rh, Ir, Pt and Pd between chromite and silicate melt: the importance of ferric iron. Chem. Geol. 302, 16–32.

Campbell, I.H., Davies, D.R., 2016. Raising the continental crust. Earth Planet. Sci. Lett. 460, 112–122.

Campbell, I.H., Griffiths, R.W., Hill, R.I., 1989. Melting in an Archaean mantle plume: heads it's basalts, tails it's komatiites. Nature 339, 697–699.

Cattell, A., Krogh, T.E., Arndt, N.T., 1984. Conflicting Sm-Nd whole rock and U-Pb zircon ages for Archean Lavas from Newton Township, Abitibi Belt, Ontario. Earth Planet. Sci. Lett. 70, 280–290.

Chavagnac, V., 2004. A geochemical and Nd isotopic study of Barberton komatiites (South Africa): implication for the Archean mantle. Lithos 75 (3–4), 253–281.

Cohen, A.S., Waters, F.G., 1996. Separation of osmium from geological materials by solvent extraction for analysis by thermal ionisation mass spectrometry. Analytica Chimica Acta 332 (2–3), 269–275.

Connolly, B.D., Puchtel, I.S., Walker, R.J., Arevalo Jr, R., Piccoli, P.M., Byerly, G., Robin-Popieul, C., Arndt, N., 2011. Highly siderophile element systematics of the 3.3 Ga Weltevreden komatiites, South Africa: Implications for early Earth history. Earth Planet. Sci. Lett. 311, 253–263.
de Wit, M.J., 2004. Archean greenstone belts do contain fragments of ophiolites. Dev. Precambrian Geol. 13, 599–614.
de Wit, M.J., Roering, C., Hart, R.J., Armstrong, R.A., de Ronde, C.E.J., Green, R.W.E., Tredoux, M., Peberdy, E., Hart, R.A., 1992. Formation of an Archaean continent. Nature 357, 553–562.
Dixon, J.G.P., 2004. Archaean geology of the Buffalo River gorge, KwaZulu-Natal. University of Natal Durban. Doctoral dissertation (unpublished),.
Du Toit, A.L. (1931). The geology of the country surrounding Nkandla, Natal. Explanation Sheet 109 (Nkandla), Geological Survey of South Africa, 111.
Echeverria, L.M., 1980. Tertiary or Mesozoic komatiites from Gorgona Island, Colombia: field relations and geochemistry. Contrib. Miner. Petrol. 73 (3), 253–266.
Eglington, B.M., Armstrong, R.A., 2004. The Kaapvaal Craton and adjacent orogens, southern Africa: a geochronological database and overview of the geological development of the craton. S. Afr. J. Geol. 107 (1–2), 13–32.
Fiorentini, M.L., Barnes, S.J., Maier, W.D., Burnham, O.M., Heggie, G., 2011. Global variability in the platinum-group element contents of komatiites. J. Petrol. 52 (1), 83–112.
Fowler, A.D., Berger, B., Shore, M., Jones, M.I., Ropchan, J., 2002. Supercooled rocks: development and significance of varioles, spherulites, dendrites and spinifex in Archean volcanic rocks, Abitibi Greenstone Belt, Canada. Precamb. Res. 115 (1–4), 311–328.
Ghosh, R., Vermeesch, P., Gain, D., Mondal, R., 2019. Genetic relationship among komatiites and associated basalts in the Badampahar greenstone belt (3.25-3.10 Ga), Singhbhum Craton, Eastern India. Precamb. Res. 327, 196–211.
Green, D.H. (1981). Petrogenesis of Archaean ultramafic magmas and implications for Archaean tectonics. In: Kroner, A. (Ed.), Precambrian Plate Tectonics. Developments in Precambrian Geology, vol. 4. Elsevier, Amsterdam, pp. 469–489.
Grosch, E. G., & Slama, J. (2021). On the volcanic architecture, petrology and geodynamic setting of the 3.48 Ga Barberton komatiite suite, South Africa. South African Journal of Geology 2021, 124(2), 343–352.
Grove, T.L., de Wit, M.J., Dann, J., 1997. Komatiites from the Komati type section, Barberton, South Africa. In: de Wit, M.J., Ashwal, L.D. (Eds.), Greenstone Belts. Oxford Science Publications, Oxford, pp. 422–437.
Gruau, G., Chauvel, C., Jahn, B.M., 1990. Anomalous Sm-Nd ages for the early Archean Onverwacht Group Volcanics. Significance and petrogenetic implications. Contrib. Miner. Petrol. 104, 27–34.
Hanski, E., Walker, R.J., Huhma, H., Polyakov, G.V., Balykin, P.A., Hoa, T.T., Phuong, N. T., 2004. Origin of the Permian-Triassic komatiites, northwestern Vietnam. Contrib. Miner. Petrol. 147 (4), 453–469.
Harvey, J., Gannoun, A., Burton, K.W., Rogers, N.W., Alard, O., Parkinson, I.J., 2006. Ancient melt extraction from the oceanic upper mantle revealed by Re-Os isotopes in abyssal peridotites from the Mid-Atlantic ridge. Earth Planet. Sci. Lett. 244 (3–4), 606–621.
Herzberg, C., 1992. Depth and degree of melting of komatiites. J. Geophys. Res. 97, 4521–4540.
Herzberg, C., Condie, K., Korenaga, J., 2010. Thermal history of the Earth and its petrological expression. Earth Planet. Sci. Lett. 292, 79–88.
Hoffmann, J.E., Wilson, A.H., 2017. The origin of highly radiogenic Hf isotope compositions in 3.33 Ga Commondale komatiite lavas (South Africa). Chem. Geol. 455, 6–21.
Hofmann, A., Anhaeusser, C.R., Dixon, J., Kröner, A., Saha, L., Wilson, A.H., Xie, H., 2019. Archaean granitoid–greenstone geology of the southeastern part of the Kaapvaal craton. In: Kröner, A., Hofmann, A. (Eds.), The Archaean geology of the Kaapvaal craton, southern Africa. Springer, Heidelberg, pp. 33–54.
Horan, M.F., Walker, R.J., Morgan, J.W., Grossman, J.N., Rubin, A.E., 2003. Highly siderophile elements in chondrites. Chem. Geol. 196 (1–4), 5–20.
Ishikawa, A., Senda, R., Suzuki, K., Dale, C.W., Meisel, T., 2014. Re-evaluating digestion methods for highly siderophile element and $^{187}Os$ isotope analysis: Evidence from geological reference materials. Chem. Geol. 384, 27–46.
Ishikawa, A., Suzuki, K., Collerson, K.D., Liu, J., Pearson, D.G., Komiya, T., 2017. Rhenium-osmium isotopes and highly siderophile elements in ultramafic rocks from the Eoarchean Saglek Block, northern Labrador, Canada: implications for Archean mantle evolution. Geochim. Cosmochim. Acta 216, 286–311.
Jahn, B.M., Vidal, P., Tilton, G.R., 1980. Archaean mantle heterogeneity: evidence from chemical and isotopic abundances in Archaean igneous rocks. Philos. Transa. Roy. Soc. Lond. Ser. A, Math. Phys. Sci. 297 (1431), 353–364.
Jahn, B.M., Gruau, G., Glickson, A.Y., 1982. Komatiites of the Onverwacht Group, South Africa: REE chemistry, Sm–Nd age and mantle evolution. Contrib. Miner. Petrol. 80, 25–40.
Janney, P.E., Shirey, S.B., Carlson, R.W., Pearson, D.G., Bell, D.R., Le Roex, A.P., Boyd, F. R., 2010. Age, composition and thermal characteristics of South African off-craton mantle lithosphere: Evidence for a multi-stage history. J. Petrol. 51 (9), 1849–1890.
Jochum, K.P., Arndt, N.T., Hofmann, A.W., 1991. Nb-Th-La in komatiites and basalts: constraints on komatiite petrogenesis and mantle evolution. Earth Planet. Sci. Lett. 107 (2), 272–289.
Kleinhanns, I.C., Kramers, J.D., Kamber, B.S., 2003. Importance of water for Archaean granitoid petrology: A comparative study of TTG and potassic granitoids from Barberton Mountain Land, South Africa. Contrib. Miner. Petrol. 145 (3), 377–389.
Kröner, A., Hoffmann, J.E., Xie, H., Wu, F., Münker, C., Hegner, E., Liu, D., 2013. Generation of early Archaean felsic greenstone volcanic rocks through crustal melting in the Kaapvaal, craton, southern Africa. Earth Planet. Sci. Lett. 381, 188–197.
Kröner, A., Nagel, T.J., Hoffmann, J.E., Liu, X., Wong, J., Hegner, E., Liu, D., 2018. High-temperature metamorphism and crustal melting at ca. 3.2 Ga in the eastern Kaapvaal craton, southern Africa. Precambr. Res. 317, 101–116.
Lahaye, Y., Arndt, N., Byerly, G., Chauvel, C., Fourcade, S., Gruau, G., 1995. The influence of alteration on the trace-element and Nd isotopic compositions of komatiites. Chem. Geol. 126 (1), 43–64.
Linström, W. (1987). The geology of the Dundee area. Explanation: Sheet 2730 (1:250 000), Geological Survey of South Africa, 52.
Liu, C.Z., Snow, J.E., Brügmann, G., Hellebrand, E., Hofmann, A.W., 2009. Non chondritic HSE budget in Earth's upper mantle evidenced by abyssal peridotites from Gakkel ridge (Arctic Ocean). Earth Planet. Sci. Lett. 283 (1–4), 122–132.
Lowe, D.R., Byerly, G.R., 2007. An overview of the geology of the Barberton Greenstone Belt and vicinity: implications for early crustal development. In: Van Kranendonk, M. J., Smithies, R.H., Bennett, V.C. (Eds.), Earth's Oldest Rocks, vol. 15. Elsevier, Amsterdam, pp. 481–526.
Maier, W.D., Roelofse, F., Barnes, S.J., 2003. The concentration of the platinum-group elements in South African komatiites: implications for mantle sources, melting regime and PGE fractionation during crystallization. J. Petrol. 44 (10), 1787–1804.
Maier, W.D., Barnes, S.J., Campbell, I.H., Fiorentini, M.L., Peltonen, P., Smithies, R.H., 2009. Progressive mixing of meteoritic veneer into the early Earth's deep mantle. Nature 460, 620–623.
Matthews, P.E., Charlesworth, E.G., Eglington, A.A., Harmer, R.E., 1989. A minimum 3.29 Ga age for the Nondweni greenstone complex in the Southeastern Kaapvaal Craton. S. Afr. J. Geol. 92, 272–278.
Mungall, J.E., Brenan, J.M., 2014. Partitioning of platinum-group elements and Au between sulfide liquid and basalt and the origins of mantle-crust fractionation of the chalcophile elements. Geochim. Cosmochim. Acta 125, 265–289.
Nesbitt, R.W., Sun, S.S., Purvis, A.C., 1979. Komatiites: geochemistry and genesis. Can. Mineral. 17, 165–186.
Nisbet, E.G., Cheadle, M.J., Arndt, N.J., Bickle, M.J., 1993. Constraining the potential temperature of the Archean mantle: a review of the evidence from komatiites. Lithos 30, 291–307.
Ohtani, E., Kawabe, I., Moriyama, J., Nagata, Y., 1989. Partitioning of elements between majorite garnet and melt and implications for petrogenesis of komatiite. Contrib. Miner. Petrol. 103, 263–269.
Palme, H., O'Neill, & H.S.C. (2014). Cosmochemical estimates of mantle composition. In: Holland, H.D., Turekian, K.K. (Eds.), Treatise on Geochemistry, Volume 3: The Mantle and Core, 2nd ed. Elsevier Ltd, Amsterdam, pp. 1–39.
Parman, S.W., Dann, J.C., Grove, T.L., deWit, M.J., 1997. Emplacement conditions of komatiite magmas from the 3·49 Ga Komati Formation, Barberton Greenstone Belt, South Africa. Earth Planet. Sci. Lett. 150, 303–323.
Pearce, J.A., 2008. Geochemical fingerprinting of oceanic basalts with applications to ophiolite classification and the search for Archean oceanic crust. Lithos 100 (1–4), 14–48.
Pearce, J.A., Ernst, R.E., Peate, D.W., Rogers, C., 2021. LIP printing: Use of immobile element proxies to characterize Large Igneous Provinces in the geologic record. Lithos 392, 106068.
Pearce, J.A., Reagan, M.K., 2019. Identification, classification, and interpretation of boninites from Anthropocene to Eoarchean using Si-Mg-Ti systematics. Geosphere 15 (4), 1008–1037.
Pearson, D. G., & Wittig, N. (2014). The formation and evolution of cratonic mantle lithosphere–evidence from mantle xenoliths. In: In: Holland, H.D., Turekian, K.K. (Eds.), Treatise on Geochemistry, Volume 3: The Mantle and Core, 2nd ed. Elsevier Ltd, Amsterdam, pp. 255–292.
Pearson, D.G., Carlson, R.W., Shirey, S.B., Boyd, F.R., Nixon, P.H., 1995. Stabilisation of Archaean lithospheric mantle: A Re-Os isotope study of peridotite xenoliths from the Kaapvaal craton. Earth Planet. Sci. Lett. 134 (3–4), 341–357.
Puchtel, I.S., Humayun, M., Walker, R.J., 2007. Os-Pb-Nd isotope and highly siderophile and lithophile trace element systematics of komatiitic rocks from the Volotsk suite, SE Baltic Shield. Precambrian Research 158 (1–2), 119–137.
Puchtel, I.S., Walker, R.J., Anhaeusser, C.R., Gruau, G., 2009. Re-Os isotope systematics and HSE abundances of the 3.5 Ga Schapenburg komatiites, South Africa: Hydrous melting or prolonged survival of primordial heterogeneities in the mantle? Chem. Geol. 262 (3–4), 391–405.
Puchtel, I.S., Blichert-Toft, J., Touboul, M., Walker, R.J., Byerly, G.R., Nisbet, E.G., Anhaeusser, C.R., 2013. Insights into early Earth from Barberton komatiites: evidence from lithophile isotope and trace element systematics. Geochim. Cosmochim. Acta 108, 63–90.
Puchtel, I.S., Walker, R.J., Touboul, M., Nisbet, E.G., Byerly, G.R., 2014. Insights into early Earth from the Pt-Re-Os isotope and highly siderophile element abundance systematics of Barberton komatiites. Geochim. Cosmochim. Acta 125, 394–413.
Puchtel, I.S., Blichert-Toft, J., Touboul, M., Horan, M.F., Walker, R.J., 2016. The coupled $^{182}W$–$^{142}Nd$ record of early terrestrial mantle differentiation. Geochem. Geophys. Geosyst. 17 (6), 2168–2193.
Puchtel, I.S., Blichert-Toft, J., Horan, M.F., Touboul, M., Walker, R.J., 2022. The komatiite testimony to ancient mantle heterogeneity. Chem. Geol. 120776.
Pyke, D.R., Naldrett, A.J., Eckstrand, O.R., 1973. Archaean ultramafic flows in Munro Township, Ontario. Geol. Soc. Am. Bull. 84 (3), 955–978.
Rehkämper, M., Halliday, A.N., Alt, J., Fitton, J.G., Zipfel, J., Takazawa, E., 1999. Non-chondritic platinum-group element ratios in oceanic mantle lithosphere: petrogenetic signature of melt percolation? Earth Planet. Sci. Lett. 172 (1–2), 65–81.
Robin-Popieul, C.C.M., Arndt, N.T., Chauvel, C., Byerly, G.R., Sobolev, A.V., Wilson, A., 2012. A new model for Barberton komatiites: deep critical melting with high melt retention. J. Petrol. 53, 2191–2229.

Sandsta, N.R., Robins, B., Furnes, H., de Wit, M., 2011. The origin of large varioles in flow-banded pillow lava from the Hooggenoeg Complex, Barberton Greenstone Belt, South Africa. Contrib. Miner. Petrol. 162, 365–377.
Schneider, K.P., Hoffmann, J.E., Münker, C., Patyniak, M., Sprung, P., Roerdink, D., Garbe-Schönberg, D., Kröner, A., 2019. Petrogenetic evolution of metabasalts and metakomatiites of the lower Onverwacht Group, Barberton Greenstone Belt (South Africa). Chem. Geol. 511, 152–177.
Shervais, J.W., 1982. Ti-V plots and the petrogenesis of modern and ophiolitic lavas. Earth Planet. Sci. Lett. 59 (1), 101–118.
Smart, K.A., Tappe, S., Ishikawa, A., Pfänder, J.A., Stracke, A., 2019. K-rich hydrous mantle lithosphere beneath the Ontong Java Plateau: significance for the genesis of oceanic basalts and Archean continents. Geochim. Cosmochim. Acta 248, 311–342.
Smart, K.A., Tappe, S., Woodland, A.B., Harris, C., Corcoran, L., Simonetti, A., 2021. Metasomatized eclogite xenoliths from the central Kaapvaal craton as probes of a seismic mid-lithospheric discontinuity. Chem. Geol. 578, 120286.
Smithies, R.H., Ivanic, T.J., Lowrey, J.R., Morris, P.A., Barnes, S.J., Wyche, S., Lu, Y.J., 2018. Two distinct origins for Archean greenstone belts. Earth Planet. Sci. Lett. 487, 106–116.
Snow, J.E., Reisberg, L., 1995. Os isotopic systematics of the MORB mantle: results from altered abyssal peridotites. Earth Planet. Sci. Lett. 136 (3–4), 723–733.
Sobolev, A.V., Asafov, E.V., Gurenko, A.A., Arndt, N.T., 2016. Komatiites reveal ahydrous Archaean deep-mantle reservoir. Nature 531, 628–632.
Sobolev, A.V., Asafov, E.V., Gurenko, A.A., Arndt, N.T., Batanova, V.G., Portnyagin, M. V., Garbe-Schönberg, D., Wilson, A.H., Byerly, G.R., 2019. Deep hydrous mantle reservoir provides evidence for crustal recycling before 3.3 billion years ago. Nature 571, 555–559.
Sossi, P.A., Eggins, S.M., Nesbitt, R.W., Nebel, O., Hergt, J.M., Campbell, I.H., Davies, D. R., 2016. Petrogenesis and geochemistry of Archean komatiites. J. Petrol. 57 (1), 147–184.
Spera, F.J., Bohrson, W.A., 2001. Energy-constrained open-system magmatic processes I: General model and energy-constrained assimilation and fractional crystallization (EC-AFC) formulation. J. Petrol. 42 (5), 999–1018.
Sproule, R.A., Lesher, C.M., Ayer, J.A., Thurston, P.C., Herzberg, C., 2002. Spatial and temporal variations in geochemistry of komatiites and komatiitic basalts in the Abitibi greenstone belt. Precambr. Res. 115, 153–186.
Steiger, R.H., Jäger, E., 1977. Subcommission on geochronology: Convention on the use of decay constants in geo- and cosmochronology. Earth Planet. Sci. Lett. 36, 359–362.
Stone, W.E., Deloule, E., Larson, M.S., Lesher, C.M., 1997. Evidence for hydrous high-MgO melts in the Precambrian. Geology 25, 143–146.
Sun, S.S., McDonough, W.F., 1989. Chemical and isotopic systematics of oceanic basalts: implications for mantle composition and processes. Geol. Soc. Lond. Spec. Publ. 42 (1), 313–345.
Sun, S.S., Nesbitt, R.W., 1978. Petrogenesis of Archaean ultrabasic and basic volcanics: Evidence from rare earth elements. Contrib. Miner. Petrol. 65, 301–325.
Tappe, S., Stracke, A., van Acken, D., Strauss, H., Luguet, A., 2020. Origins of kimberlites and carbonatites during continental collision: Insights beyond decoupled Nd-Hf isotopes. Earth Sci. Rev. 208, 103287.
Tappe, S., Shaikh, A.M., Wilson, A.H., Stracke, A., 2022. Evolution of ultrapotassic volcanism on the Kaapvaal craton: deepening the orangeite versus lamproite debate. Geol. Soc. Lond. Spec. Publ. 513 (1), 17–44.
Trela, J., Gazel, E., Sobolev, A.V., Moore, L., Bizimis, M., Jicha, B., Batanova, V.G., 2017. The hottest lavas of the Phanerozoic and the survival of deep Archaean reservoirs. Nat. Geosci. 10 (6), 451–456.
van Acken, D., Hoffmann, J.E., Schorscher, J.H.D., Schulz, T., Heuser, A., Luguet, A., 2016. Formation of high-Al komatiites from the Mesoarchean Quebra Osso Group, Minas Gerais, Brazil: trace elements, HSE systematics and Os isotopic signatures. Chem. Geol. 422, 108–121.
van der Meer, Q.H., Klaver, M., Reisberg, L., Riches, A.J., Davies, G.R., 2017. Preservation of an Archaean whole rock Re-Os isochron for the Venetia lithospheric mantle: Evidence for rapid crustal recycling and lithosphere stabilisation at 3.3 Ga. Geochim. Cosmochim. Acta 216, 242–263.
Van Kranendonk, M.J., 2011. Cool greenstone drips, hot rising domes, and the role of partial convective overturn in Barberton greenstone belt evolution. J. Afr. Earth Sc. 60 (5), 346–352.
Vermeesch, P., 2018. IsoplotR: A free and open toolbox for geochronology. Geosci. Front. 9, 1479–1493.
Viljoen, M., Viljoen, R., 1969. The effects of metamorphism and serpentinization on the volcanic and associated rocks of the Barberton region. Geol. Soc. South Africa, Special Publication 2, 29–54.
Waterton, P., Pearson, D.G., Mertzman, S.A., Mertzman, K.R., Kjarsgaard, B.A., 2020. A fractional crystallization link between komatiites, basalts, and dunites of the Palaeoproterozoic Winnipegosis komatiite belt, Manitoba, Canada. Journal of Petrology 61 (5), egaa052.
Waterton, P., Mungall, J., Pearson, D.G., 2021. The komatiite-mantle platinum-group element paradox. Geochim. Cosmochim. Acta 313, 214–242.
White, J.D., McPhie, J., Soule, S.A., 2015. Submarine lavas and hyaloclastite. In: The encyclopedia of volcanoes. Academic Press, pp. 363–375.
Wilson, A.H., 2003. A new class of silica enriched, highly depleted komatiites in the southern Kaapvaal Craton, South Africa. Precambr. Res. 127, 125–141.
Wilson, A.H., 2019. The Late-Paleoarchean Ultra-Depleted Commondale Komatiites: Earth's Hottest Lavas and Consequences for Eruption. J. Petrol. 60 (8), 1575–1620.
Wilson, A.H., Versfeld, J.A., 1994. The early Archaean Nondweni greenstone belt, Southern Kaapvaal Craton, South Africa, part II. Characteristics of the volcanic rocks and constraints on magma genesis. Precambr. Res. 67, 277–320.
Wilson, A.H., Shirey, S.B., Carlson, R.W., 2003. Archaean ultra-depleted komatiites formed by hydrous melting of cratonic mantle. Nature 423, 858–861.
Wilson, A.H., Groenewald, B., Palmer, C., 2013. Volcanic and volcaniclastic rocks of the Mesoarchaean Pongola Supergroup in South Africa and Swaziland: distribution, physical characteristics, stratigraphy and correlations. S. Afr. J. Geol. 116 (1), 119–168.
Xie, Q., Kerrich, R., Fan, J., 1993. HFSE/REE fractionations recorded in three komatiite basalt sequences, Archean Abitibi greenstone belt: implications for multiple plume sources and depths. Geochim. Cosmochim. Acta 57, 4111–4118.